ANALYSIS OF $\omega \to \pi^+\pi^-\pi^0$ DECAY USING CLAS AT JEFFERSON LAB

Master Thesis

by

Andrés Melo[1]

Tutors: Dr. Gabriel González-Sprinberg[1], Dr. Carlos Salgado[2,3]

[1]Facultad de Ciencias, Universidad de la República, Montevideo, Uruguay

[2]Norfolk State University, Norfolk, Virginia, USA

[3]Thomas Jefferson National Accelerator Facility, Newport News, Virginia, USA

2016

Abstract

In this work we study in detail the $\omega \to \pi^+\pi^-\pi^0$ decay. It was produced and detected at Jefferson Laboratory (JLab) with the CLAS detector as part of the g12 run by the photoproduction reaction $\gamma p \to p\omega$. Our photon energy range is above 3.6 GeV and below 5.3 GeV, which makes this experimental data the first about ω photoproduction at these energies.

Three body decay reactions are very important in order to understand hadron physics. Various meson resonances has been discovered in the past analyzing the three-pion spectrum, which opens the possibility of finding new resonances that do not fit current models. The decay we want to study is a precise scenario in which hadronic QCD inspired models can be tested. We fit a recent one of such models to our data.

In this work the primary objective is to obtain a clean signal for the ω. This was done mostly by cutting our data according to known kinematic quantities and then fitting it by a functional form that is expected from a signal with a background. From the resulting ω signal we obtained the values of 783.45 MeV for its mass and 9.92 MeV for its width.

Then we fitted the model developed by the Joint Physics Analysis Center (JPAC) at JLab to our data to see how well it describes the mentioned decay and to obtain one of their parameters. Preliminary fits show that the value of this parameter does not fall within the expected range from the model.

Preface

This work received financial support from Comisión Sectorial de Investigación Científica - Universidad de la República (CSIC-UdelaR) through a Initiation to Research scholarship and from the Norfolk State University and the Thomas Jefferson National Accelerator Facility. To learn the computational tools and basic knowledge necessary to begin this work I did an internship at Jefferson Lab between March and July 2012 under the supervision of Dr. Carlos Salgado. The raw data used in this work was facilitated by the CLAS g12 collaboration, led by Dr. Salgado and Dr. Dennis Weygand.

At the accelerator facility Mike Kunkel spent a great deal of his time showing me the basics of data analysis, mostly using the ROOT software [1], and other computational tools like farm usage while the skimming of the data he performed was running. Also Johan Goetz helped me with computational issues, and Diane Schott showed me how to perform a Monte Carlo simulation with scripts used by the collaboration. Back in Uruguay, I continued my work supervised by Dr. Gabriel González-Sprinberg and maintaining reunions via Skype with Dr. Salgado. I would like to thank all the people involved in the making of this work for their time and advise.

Some preliminary results (all that is presented before the application of the kinematic fitter, which was performed by Kunkel) were presented as a poster at the X Latin American Symposium on Nuclear Physics and Applications, which took place in December 2013 in Montevideo, Uruguay, and on the XIV Reunion of the Uruguayan Physics Society (SUF) in November 2014, although by this stage most of the results presented were already superseded by the analysis done after a kinematic fit was applied at the beginning of 2014, but they were not yet presented to the CLAS collaboration as must be done before being presented anywhere else.

Compared to the preliminary results already presented in those instances, the results presented in this work are not only based now on kinematically fitted data but also the background noise was filtered with a more powerful method which involves a Q-factor calculation, whose use for this work was proposed at the beginning of 2015, and by a new Monte Carlo simulation, performed by Dr. Salgado.

Contents

1 Introduction

In this chapter we will give a very brief overview of the current state of particle physics, some fundamentals of hadron spectroscopy and a description of the model to which we want to fit our data.

1.1 The Standard Model

The current formulation of the Standard Model (SM) [2] was finalized in the mid-1970s, after the experimental confirmation of the existence of quarks, elementary particles (as far as we know) that were independently proposed by Murray Gell-Mann [3] and George Zweig [4] on their constituent quark model (CQM), which characterizes hadrons according to their valence quarks. It describes hadrons based on symmetries such as energy and angular momentum conservation, while broken symmetries can lead to new symmetries and properties. At the beginning only the up, down and strange quarks were included, while the charm, top and bottom quarks were added later. The CQM is an approximate model superseded by the Standard Model, which allows other states that we call "exotic" (like glueballs, multi-quark or hybrid states) that the CQM does not.

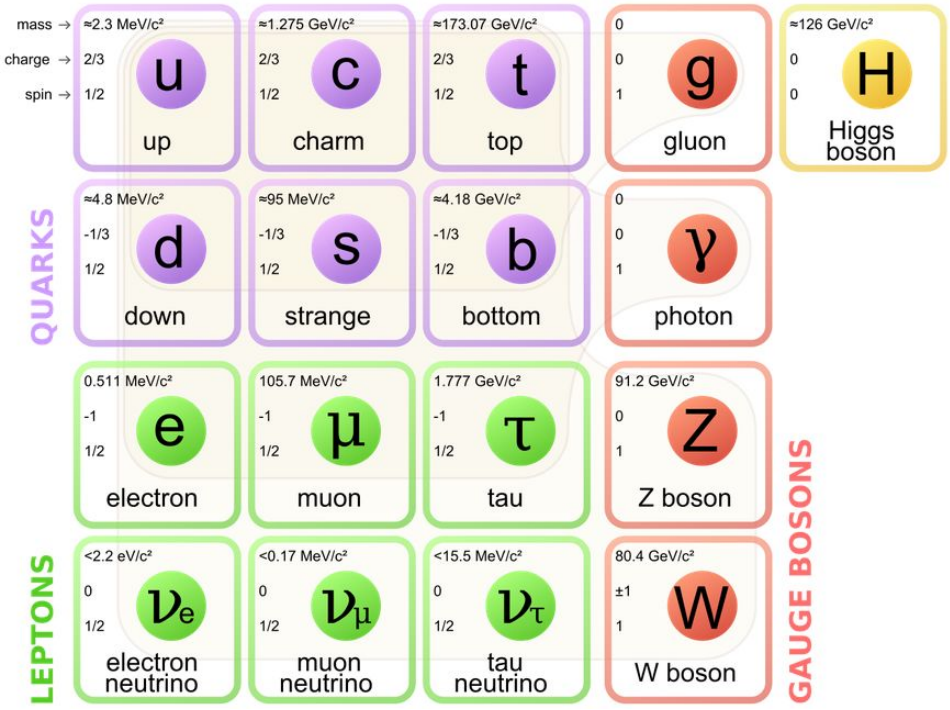

Figure 1: Schematic depiction of the Standard Model.

As shown in figure 1, the Standard Model classifies all the known subatomic particles into three generations of matter (quarks and leptons), gauge bosons (carriers of the electromagnetic, weak, and strong nuclear interactions) and the Higgs boson (whose preliminary experimental confirmation came in 2013), including in this manner 3 of the 4 fundamental interactions (the exception being gravity).

The strong nuclear interaction is responsible for the strong force. It is a short-range force: between 1 and 3 femtometers it is responsible for binding the nucleons together, while at shorter distances it binds the quarks together in hadrons, either mesons (bosons) or baryons (fermions). The gauge bosons (force carriers) of this force are the gluons, which are neutral, massless vector particles of spin-parity $J^P = 1^-$, like the photon in the case of electromagnetic interactions.

1.2 Quantum Chromodynamics

Quantum Chromodynamics (QCD) [5] is the part of the Standard Model that describes the strong interactions. In this theory, the strong force acts between color charges. Quarks have color charge (which can be red, green or blue), while antiquarks have anticolor charge, and gluons have color-anticolor charge, therefore they can interact between themselves with triple or quadruple gluon vertices, like the ones shown in figure 2, something that does not happen in the case of photons.

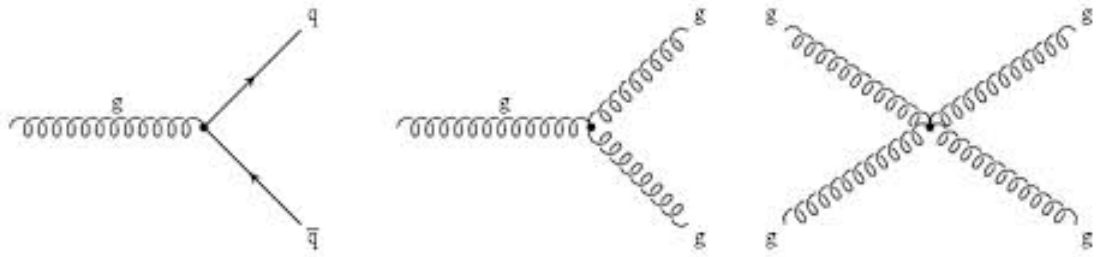

Figure 2: Possible gluon vertex.

QCD has two interesting properties: confinement, at low energies, and asymptotic freedom at high energies. The boundary between these phenomena has been determined (with data from 2010) by A Large Hadron Collider Experiment (ALICE) at the Large Hadron Collider (LHC) to be around 160 MeV [6].

Confinement allegedly does not allow the existence of free quarks, any attempt of separating two of them results in hadronization, name given to the creation of another quark pair from the energy in the gluon field, since the force between

the two first quarks does not diminish when their separation increases. Although this remains analytically unproven since the equations of QCD remain unsolved at these energy ranges, it has been reproduced in models like Lattice QCD.

Asymptotic freedom manifests itself at very high-energy ranges, where quarks and gluons interact very weakly, resulting in a quark-gluon plasma (QGP). This was predicted from QCD perturbative calculations, allowed at these energy ranges, by Frank Wilczek and David Gross [7] and independently by David Politzer [8], earning them the 2004 Nobel Prize in Physics.

1.3 Groups and Symmetries

The similarities between the proton and the neutron (they have nearly the same mass and interact almost in the same way if the electromagnetic forces are neglected) prompted Heisenberg to propose that they were two different states of a single particle called the nucleon [9]. Isospin (I) is then introduced (in the abstract isospin space) similarly to spin by saying that the nucleon carries $I = \frac{1}{2}$ and that the eigenvalues of its third component, I_3, determines if the state corresponds to a proton ($I_3 = +\frac{1}{2}$) or a neutron ($I_3 = -\frac{1}{2}$). Heisenberg then proposed that strong interactions are invariant in isospin space, which implies that isospin is conserved in this interaction [10]. This means that strong interactions are invariant under the symmetry group $SU(2)$ ($SU(n)$ are special unitary groups of degree n, defined as a Lie group of $n \times n$ unitary matrices with determinant 1).

The isospin and its properties could be later extended to the hadronic multiplets: for Λ, $I = 0$, for the three pions, $I = 1$ and for the four $\Delta's$, $I = \frac{3}{2}$. It was Gell-Mann who combined this structure with strangeness to create his Eightfold Way and, ultimately, the CQM. The similarity between the proton and the neutron was then understood from the similarity between the up and down quarks, and the isospin formalism, translated to them, is now known to be an approximate (but anyway useful) symmetry.

Parity (P) is the operation that mirrors the spatial coordinates about the origin, thus flipping their sign. That the mirror image of any physical process was also possible, or parity invariance, was thought to be self-evident, until 1956 when Lee and Yang realized that, although there was plenty of experimental evidence for parity invariance for electromagnetic and strong interactions, there was none for

the weak ones [11]. Shortly thereafter Wu carried out an experiment that showed that weak interactions were not parity invariant [12].

C-parity (C), also called charge conjugation, refers to the operation that changes each particle into its antiparticle and, like parity, electromagnetic and strong interactions are invariant under this operation, while the weak interactions are not, since a left-handed neutrino would give a left-handed antineutrino, which does not exist (as far as we know). Since only neutral bosons are eigenstates of C its applications are limited.

G-parity (G) is defined as CR_2, where $R_2 = e^{i\pi I_2}$ is a rotation of 180° around the second axis in isospin space (although any axis in the plane defined by the first and second axis can be used). All mesons with no strangeness, charm, bottomness or topness are eigenstates of G. This transformation is only approximately invariant in the strong interactions because the isospin is involved.

Parity, C-parity and G-parity are finite symmetry groups, each with only two elements with eigenvalues ± 1 since when applied twice the resulting operation is the identity.

1.4 Hadron Spectroscopy

The development of the ideas about the structure of the atom and, consequentially, quantum mechanics, came in great part from the study of the atomic spectrum. This was done by analyzing the light emitted by a previously excited atom, which in this way gave information about itself, and in particular about the discrete nature of the energies of the excited states (which we call spectrum of the atom), explained in 1913 by Niels Bohr, although his model is now known to be a first-order approximation of the hydrogen atom result derived form quantum mechanics.

The study of hadrons is envisioned in the same way as described with atoms, although there are many differences between them. The increased technical difficulties are obvious: while in the case of the atom the energies required were readily available in the XIX century and the emitted radiation sometimes was in the visible range, when dealing with hadrons a large particle accelerator and a complicated detector system are needed.

Also we know that according to the Heisenberg Principle

$$\Delta E \Delta t \approx \frac{\hbar}{2} \tag{1.1}$$

Then the energy uncertainty of the excited state can be estimated from its mean lifetime, taking it as the uncertainty in time [13], since a finite lifetime would imply an indeterminate energy constrained by the relation

$$\Delta E \approx \frac{\hbar}{2\tau} \tag{1.2}$$

This means that while in the atomic case the spectrum had the appearance of separated lines, the hadronic case could be (and it is) more problematic in that respect since the signal broadening is enough to make some of them to overlap, thus the correct interpretation of the spectra requires a more careful and advanced study (like performing a partial wave analysis).

It is worth mentioning that if we only consider the energy uncertainty as described in the last paragraph, the profile of our signal would be a Lorentzian (also called Breit-Wigner) distribution [14]. We also have to consider the resolution of the detectors, which gives a Gaussian profile [15]. The convolution of these two broadening mechanisms is what we call a Voigtian distribution, and as such is commonly used to fit and analyze signal profiles.

Since QCD cannot be solved analytically we cannot predict directly from it the form of the hadronic spectrum, but there are approximate models (like CQM and Lattice QCD, among others) from where we can obtain many excited states, which end up being more than the observed ones. This phenomenon is known as the missing baryon problem.

1.5 JPAC Decay Model

The model we want to fit with our data was developed for the vector mesons ω and ϕ [16] (we will leave many of the details to that reference). Their mass, momentum and helicity, in our case of the ω, will be noted as M, p_V and λ. We can write the matrix element for the three pion decay of the ω as [17]

$$\langle \pi^a(p_1)\pi^b(p_2)\pi^c(p_3)|T|V(p_V,\lambda)\rangle = (2\pi)^4 \delta(p_V - p_1 - p_2 - p_3) H_\lambda^{abc} \tag{1.3}$$

with an helicity amplitude

$$H_\lambda^{abc} = i\epsilon_{\mu\nu\alpha\beta}\epsilon^\mu(p_V,\lambda)p_1^\nu p_2^\alpha p_3^\beta \frac{P_{abc}^1}{\sqrt{2}} F(s,t,u) \tag{1.4}$$

where p_1, p_2 and p_3 are the momentum of the outgoing pions with a, b and c their Cartesian isospin indices, T is defined by $S = 1 + iT$ where S is the scattering matrix, P_{abc}^1 is the isospin factor which corresponds to the coupling of the three pions to the ω and s, t and u are the Mandelstam variables of the decay, which will be defined in what follows and can be easily shown to satisfy the relation $s + t + u = M^2 + m_\pi^2$. Lorentz and parity invariance imply that H_λ^{abc} can indeed be expressed in terms of a single scalar function $F(s,t,u)$, which is free from kinematical singularities (as Mandelstam analyticity requires) and because of crossing symmetry it describes not only the $\omega \to 3\pi$ decay but also the $\omega\pi \to 2\pi$ ones.

Considering first the kinematics of the s-channel scattering $\omega(p_V,\lambda)\pi_{\bar{3}}^c \to \pi_1^a\pi_2^b$, we have $s = (p_V + p_{\bar{3}})^2 = (p_V - p_3)^2$, $t = (p_V - p_1)^2$ and $u = (p_V - p_2)^2$. In the center of mass frame, if we call $q(s)$ the relative momentum magnitude between the outgoing pions and $p(s)$ the momentum magnitude of the incoming pion we have

$$p(s) = \frac{\lambda^{\frac{1}{2}}(M^2, m_\pi^2, s)}{2\sqrt{s}}, \qquad q(s) = \frac{\lambda^{\frac{1}{2}}(m_\pi^2, m_\pi^2, s)}{2\sqrt{s}} \tag{1.5}$$

where $\lambda(x,y,z) = x^2 + y^2 + z^2 - 2(xy + yz + xz)$ is the Kallen triangle function. It can be shown that the cosine of the s-channel scattering angle is related with the Mandelstam variables by

$$z_s = \cos\theta_s = \frac{t-u}{4p(s)q(s)} = \frac{t-u}{k(s)} \tag{1.6}$$

We can write the s-channel partial wave decomposition [18]

$$H_\lambda^{abc} = \frac{P_{abc}^1}{\sqrt{2}} \sum_{J=1,3\ldots}^{\infty} (2J+1) d_{\lambda 0}^J(\theta_s) f_\lambda^J(s) \tag{1.7}$$

where $d_{\lambda 0}^J(\theta_s)$ are the Wigner d-functions and the x-z plane was chosen as the reaction plane. The sum goes over odd values of J because of the Bose symmetry of pions, and because of parity conservation $f_0^J(s) = 0$ and $f_{+1}^J(s) = -f_{-1}^J(s) \equiv f_J(s)$. Since H_λ^{abc} and $F(s,t,u)$ are related, we can determine the kinematical singularities of $f_J(s)$.

Writing the Wigner d-functions in terms of the derivatives of the Legendre polynomials, and defining the reduced partial waves $F_J(s)$ as

$$d^J_{10}(\theta) = -\frac{sen\theta}{\sqrt{J(J+1)}}P'_J(\cos\theta), \quad F_J(s) = \frac{\sqrt{2}(2J+1)f_J(s)}{\sqrt{s}\sqrt{J(J+1)}(p(s)q(s))^J} \tag{1.8}$$

we have

$$H^{abc}_{+} = -P^1_{abc}\frac{\sqrt{\phi}}{4}\sum_{J=1,3...}^{\infty}(p(s)q(s))^{J-1}P'_J(z_s)F_J(s) \tag{1.9}$$

where $\phi = (2\sin\theta\sqrt{s}p(s)q(s))^2 = stu - m_\pi^2(M^2 - m_\pi^2)^2$ is the Lorentz-invariant Kibble function, and then we obtain

$$F(s,t,u) = \sum_{J=1,3...}^{\infty}(p(s)q(s))^{J-1}P'_J(z_s)F_J(z_s) \tag{1.10}$$

We see that $(p(s)q(s))^{J-1}P'_J(z_s)$ is a polynomial free from kinematical singularities, which implies that F_J can have only dynamical singularities. The sum converges in the s-channel physical region, and to obtain the amplitudes on the other channels it must be analytically continued. We will truncate this infinite series to a maximum value J_{max} since we expect the first terms to be the dominant ones. This approximation, whose diagrams are represented in figure 3, is what we call the Isobar Model [19].

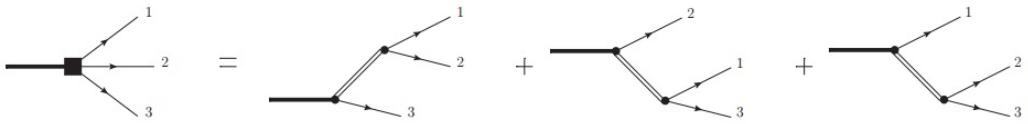

Figure 3: Isobar decomposition diagrams.

Singularities of $F(s,t,u)$ in s, t and u can only emerge from the infinite terms in the sum. In order to retain dynamical singularities, $F(s,t,u)$ is approximated by a linear combination of truncated partial wave series. Then, because of Bose symmetry, we have

$$F(s,t,u) = \sum_{J=1,3...}^{J_{max}}(p(s)q(s))^{J-1}P'_J(z_s)F_J(z_s) + (s\to t) + (s\to u) \tag{1.11}$$

which satisfies crossing symmetry and single-variable dispersion relation, and where

$$z_t = \cos\theta_t = \frac{s-u}{4p(t)q(t)}, \qquad z_u = \cos\theta_u = \frac{t-s}{4p(u)q(u)} \tag{1.12}$$

We will take $J_{max} = 1$ (only P-waves) since these are expected to be the dominant terms. Imposing elastic unitarity leads to the Khuri-Treiman (KT) equations [20], and we obtain

$$Disc\, F(s) = \rho(s)t^*(s)(F(s) + \hat{F}(s)), \quad \hat{F}(s) = 3\int_{-1}^{+1} \frac{1-z_s^2}{2} F(t(s,z_s))dz_s \tag{1.13}$$

where $F(s) = F_{J=1}(s)$, $t(s) = t_{J=1}(s)$ and $\rho(s) = \sqrt{1-4m_\pi^2/s}$. For real s we have

$$F(s) = \frac{1}{\pi}\int_{4m_\pi^2}^{\infty} \frac{Disc\, F(s')}{s'-s-i\epsilon} ds' \tag{1.14}$$

This equation was derived for $s \geq (M+m_\pi)^2$, so it must be continued analytically in s to the decay region $4m_\pi^2 \leq s \leq (M-m_\pi)^2$. With this we are considering the interactions due to all possible pion-pion rescattering, whose diagrams are represented in figure 4

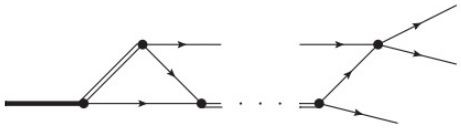

Figure 4: Crossed channel rescattering diagrams.

In working out a solution for $F(s)$ the integral will be split in two parts, the first one determined by elastic scattering while the second part will take into account inelastic effects, then we have

$$F(s) = \Omega(s)\left(\frac{1}{\pi}\int_{4m_\pi^2}^{s_i} \frac{\rho(s')t^*(s')}{\Omega^*(s')}\frac{\hat{F}(s')}{s'-s} ds' + \Sigma(s)\right) \tag{1.15}$$

with

$$\Sigma(s) = \sum_{k=0}^{\infty} a_k \omega^k(s), \quad \omega(s) = \frac{\sqrt{s_i - s_E} - \sqrt{s_i - s}}{\sqrt{s_i - s_E} + \sqrt{s_i - s}} \tag{1.16}$$

where $s_E = 0$ and $s_i = 1\,GeV$ is the point where the inelastic contributions become relevant. The a_k coefficients are unknown and are determined by fitting to the experimental data. In fact, only the a_0 term (expected to be positive) will be considered, this because the fit has proved to converge very fast, and also because with only one parameter it is sufficient to reproduce any Dalitz plot shape [21].

The previous integral is solved by numerical iteration, and then we can obtain the Dalitz plot distribution and the partial and total 3π decay widths [22]

$$\frac{d^2\Gamma}{dsdt} = \frac{P(s,t)|F(s,t,u)|^2}{3(2\pi)^3 32M^3} \tag{1.17}$$

where $P(s,t) = \frac{\phi(s,t)}{4}$, called kinematical or P-wave factor, which from now on we will call P.

We can construct a Dalitz plot in terms of the Lorentz invariant dimensionless parameters [23]

$$x = \frac{\sqrt{3}(t-u)}{2M(M-3m_\pi)}, \qquad y = \frac{3(s_c - s)}{2M(M-3m_\pi)} \tag{1.18}$$

where $s_c = \frac{M^2+3m_\pi^2}{3}$.

Finally, figure 5 shows the Dalitz plot distribution generated by the JPAC for the *omega* decay, divided by P and normalized to 1 at $x = y = 0$.

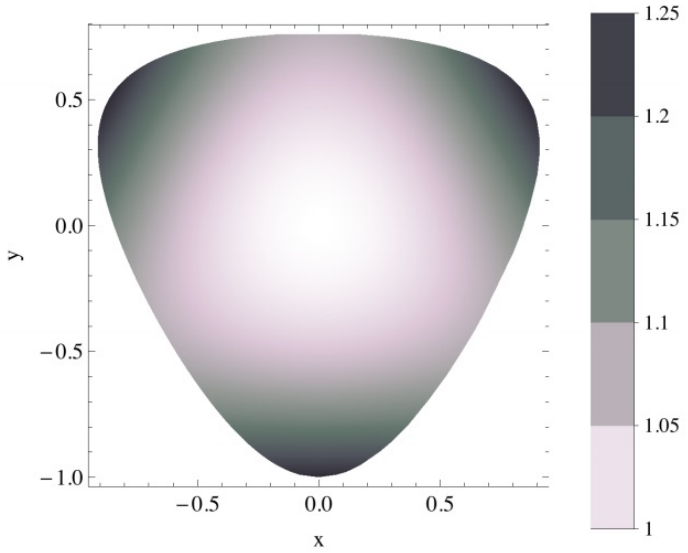

Figure 5: Numerical Dalitz plot obtained by the JPAC.

2 Experimental Setup And Apparatus

In this chapter we will describe some of the basic characteristics and operation of the particle accelerator and the detector hosted at Hall B, which were used to obtain the data analyzed in this thesis.

2.1 Thomas Jefferson National Accelerator Facility

The data analyzed in this thesis was taken at the Thomas Jefferson National Accelerator Facility (TJNAF), also called Jefferson Lab (JLab), which is located at Newport News, Virgina, USA, which can conduct research at the quark level. It hosts a particle accelerator (CEBAF), which will be described in the next section, and three experimental Halls (A, B and C), each one hosting its own detector system.

Figure 6: Aerial view of Jefferson Lab.

2.2 Continuous Electron Beam Accelerator Facility

The Continuous Electron Beam Accelerator Facility CEBAF is a recirculating linear electron accelerator, with the capability of delivering a quasi-continuous electron beam. Figure 7 shows a diagram describing some components of the CEBAF.

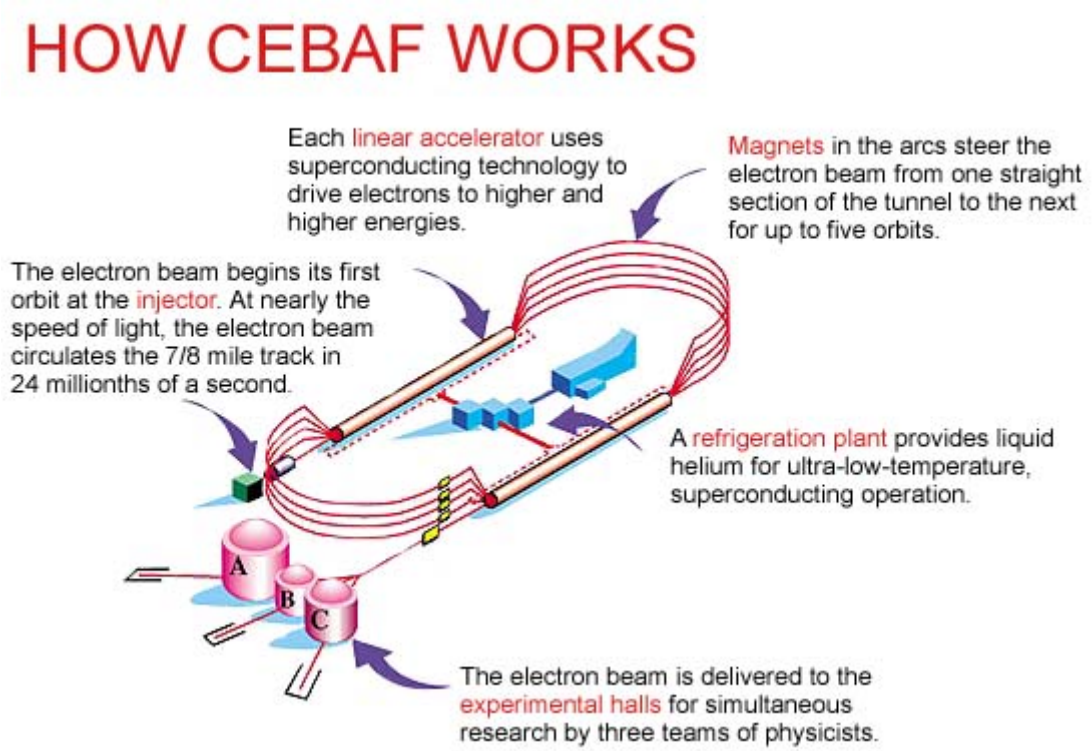

Figure 7: CEBAF, located at Jefferson Lab.

The electrons are supplied by the injector after being obtained by illuminating a gallium arsenide (GaAs) photocathode with a system of lasers [24]. Then, after clearing an optical chopper, they are accelerated to between 40 and 80 MeV by means of 2.25 superconducting radio-frequency (RF) niobium cavities, which are metallic chambers that contain an electromagnetic field whose waves become resonant and build up inside the cavity and on phase with the injector, alternating their polarity at a frequency determined by the arrival time of the electrons with the purpose of accelerating them [25]. All this system is submerged in liquid helium and kept at $2°K$ with the propose of attain superconducting properties. A diagram of the RF cavities is shown in figure 8.

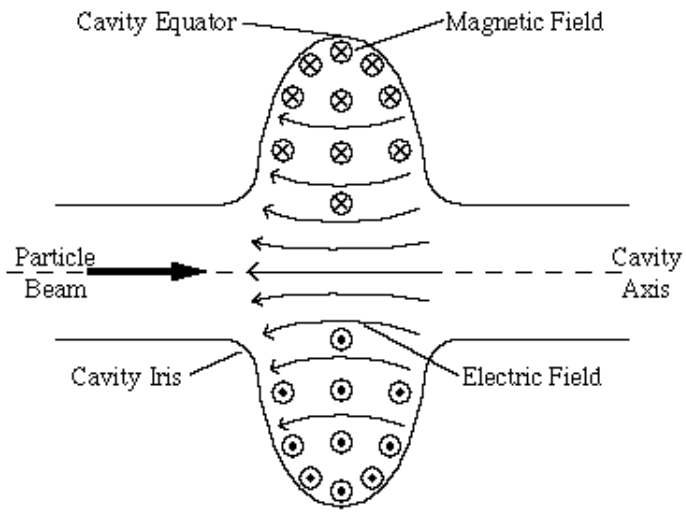

Figure 8: RF cavity diagram.

After being initially accelerated, the electrons enter one of the two parallel linear accelerators (linacs), which are made of 168 RF cavities like the ones described before. Each the linacs are connected on both of each ends by different recirculation arcs, each dealing with electrons of different energies separated when entering the arcs and recombined upon exiting them. These recirculation arcs redirects the electrons by means of steering dipole magnets, making a track length for each pass of about 1400 meters. The energy of the electrons is increased by certain amount each time they pass through the linacs, the value of the increment depend on the linacs settings but is close to 600 MeV. Since in any of the passes the electrons can be extracted at the end of the linacs, with typical settings there can be up to five passes, therefore the electron beam energies available to the end stations range from 1.2 GeV to 6.0 GeV in 1.2 GeV intervals. The electrons circulate in pulses separated by 0.67 ns, and they are splitted into different beams upon exiting the linacs, one for each Hall and with the possibility of having on each one of them different energy, therefore the electrons will appear as pulses separated by 2.004 ns (this is called the RF time bucket) [26].

The range of energies in which CEBAF operates is called "intermediate" ("low" being a few dozens of MeV, where nucleons are treated as fundamental, and "high" being hundreds of GeV, where we can have a free quarks soup), therefore in this regime non-perturbative QCD should be used when analyzing the data obtained, and the fact that it is still being developed implies that this energy range is of particular interest.

2.3 Experimental Hall B

The Experimental Hall B is one of the three end stations (each with its own characteristics) dedicated to physics research. Both electron-beam and photon-beam experiments are conducted in it. The Hall-B Bremsstrahlung tagging system (tagger) and the CEBAF Large Acceptance Spectrometer (CLAS) are the two major detector systems that are housed by this end station. A diagram of the Experimental Hall B is shown in figure 9, where the tagger is shown on the right.

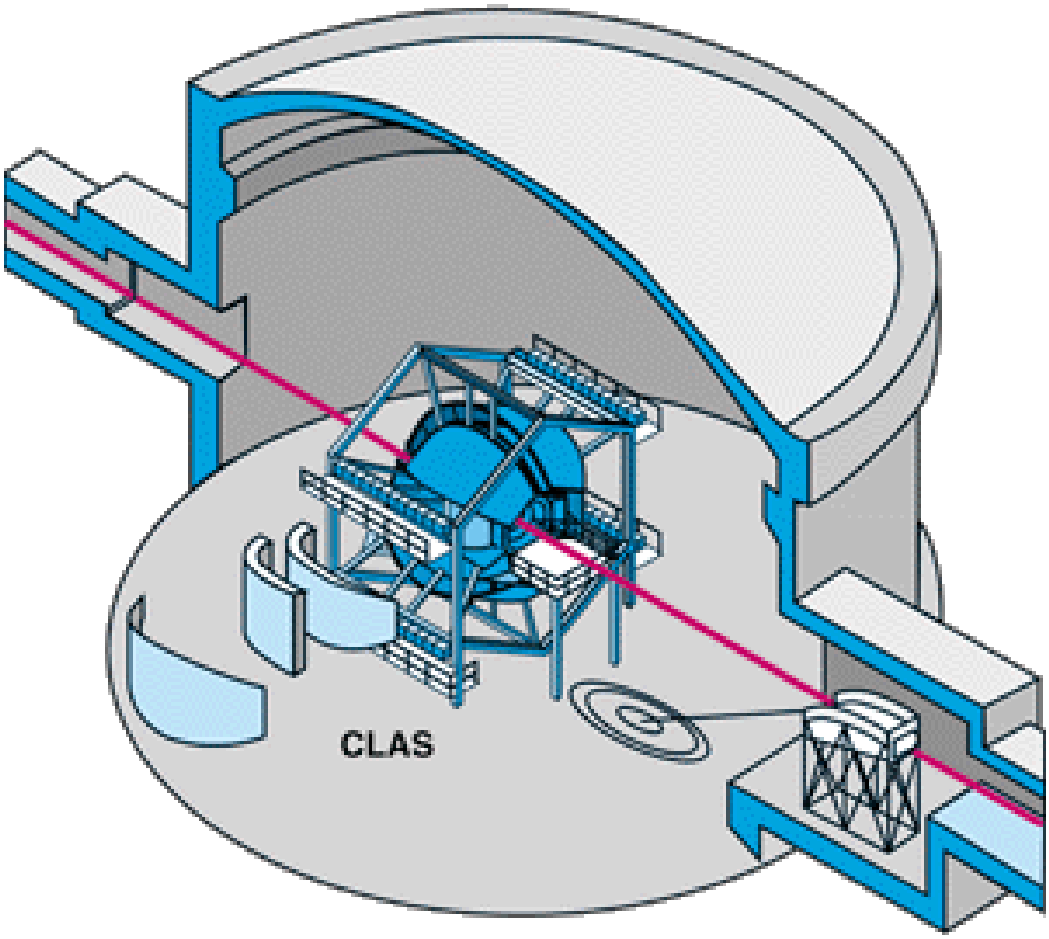

Figure 9: Experimental Hall B.

2.4 Tagging System

In Hall B, the photon beam comes from the bremsstrahlung radiation of electrons scattered by a thin radiator foil made of gold (which reduces background photons produced from scattering between electrons), whose width can be varied between 10^{-6} and 10^{-3} radiation lengths (the radiation length of gold is 3344 μm), which

makes it small enough to avoid multiple scattering. Along the beam line there are three harp systems, composed of two thin moving wires that can measure the x and y coordinates of the beam with great accuracy. At this stage, the tagger magnet provides an uniform magnetic field of 1.13 T to sweep the electrons (and other possible charged particles produced by nuclear interactions) off the beam.

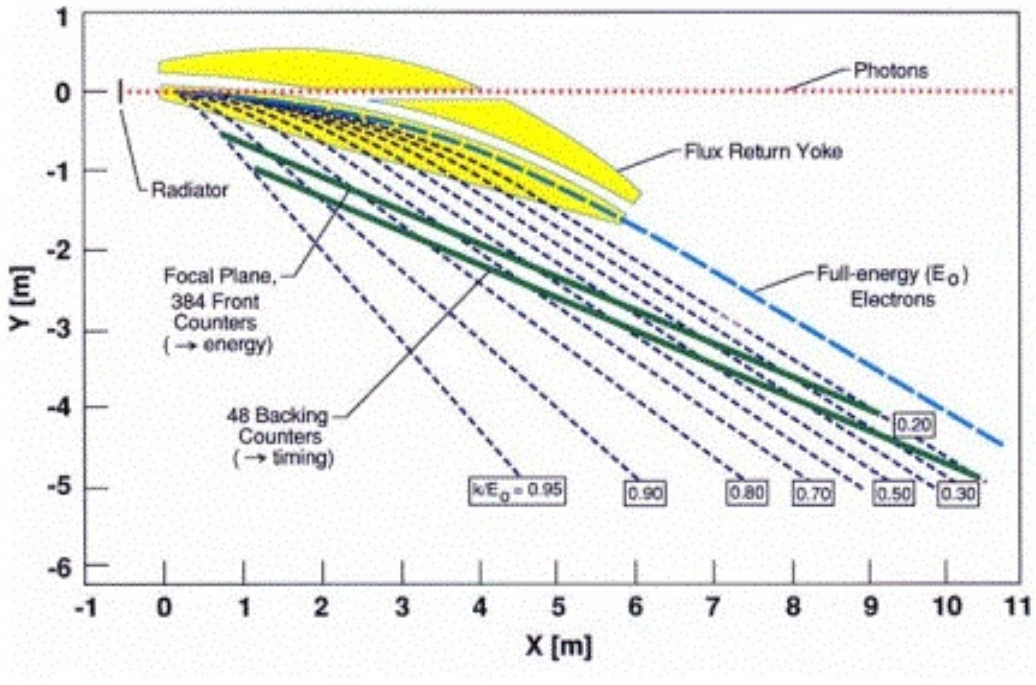

Figure 10: Tagger diagram.

Figure 10 shows a diagram of the tagger system. The deflected electrons pass through two layers of scintillators: the E-plane, composed of 384 narrow overlapping scintillators (E-counters) that can measure the energy of the electrons with a resolution of 0.1% their value (the photon energies can be obtained from the difference between the incoming electron beam energies and the energies measured by the E-plane), and the T-plane, composed of 61 overlapping scintillators (T-counters) that can time tag the electrons with a resolution of 300 ps (enough to identify to which pulse the electrons came from and useful to determine the event vertex time). All the signals were read using photomultiplier tubes (PMTs). The tagging system can tag photon energies that are between 20% and 95% of that of the electrons, which can be up to 6.1 GeV (full energy electrons go to the beam dump).

Also, before reaching the target, two collimators are placed to trim the beam,

and between them there are sweeping magnets that get rid of charged particles that could have been produced by interactions between the photons and the first collimator.

2.5 CEBAF Large Acceptance Spectrometer

The principal characteristics of CLAS are its ability to run using a photon beam (as it was previously described) and its large solid angle coverage, which means that it is well adapted for experiments that require the detection of a large number of particles in the final state [27]. It has six multi layered instrumented sectors azimuthally symmetric about the beam line, and was designed with the following considerations: large angular detection range ($0° \leq \phi \leq 360°$, $8° \leq \theta \leq 142°$ for charged particles, $8° \leq \theta \leq 45°$ for neutral ones) large momentum detection range ($0.1 \leq p \leq 4.0\ GeV/c$ for charged particles, energy detection range for photons E $\geq 50\ MeV$), good angular resolution ($\delta\theta \approx 1.0\ mrad$), good momentum resolution ($\delta p/p \approx 0.5\%$ at small θ, 1.0% at large θ), and high luminosity (electron beam: $L \approx 10^{34} cm^{-2} s^{-1}$, photon beam: I $\approx 10^{7} s^{-1}$. A couple of diagrams of CLAS are shown in figures 11 and 13.

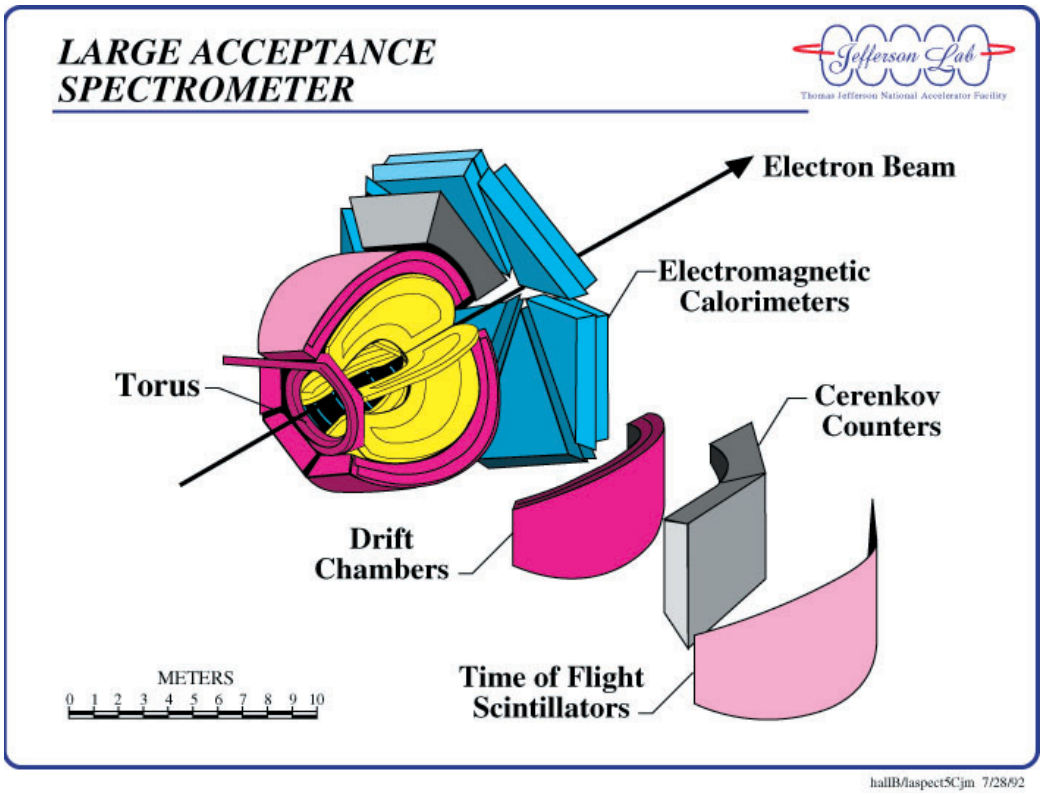

Figure 11: Overview of CLAS. It has approximately 8 meters in diameter.

On the following sections we are going to describe the components of CLAS from the inside to the outside.

2.5.1 Target

The target (also called cryotarget) used is a cylinder with a diameter of about 4 cm and 40 cm in length, filled with liquid hydrogen. It is commonly placed at the center of the detector, but in this experiment it was displaced 90 cm upstream in relation to that position, decreasing the angle covered by the downstream hole (area without detectors) of CLAS from 8° to 6°, and at the same time, providing more coverage of small-angle tracks, although this reduces the maximum angle acceptance. This was done in this way because we are interested in t-channel meson production at low momentum transfer (in absolute value), or diffractive events, a requirement of the model to which we want to fit our data. Also, at this stage the photon beam has a spread of about 1 cm full width half maximum.

2.5.2 Start Counter

Immediately surrounding the target we have the start counter (ST), a set of 24 thin scintillators which gives us an initial timing with a resolution of 350 ps. When used with the signal of the tagger previously described the accidental trigger rate can be greatly reduced, and in conjunction with the time of flight counter one can pinpoint the pulse that gave rise to the event. The ST is in fact a set of three independent detectors (8 scintillators per detector), each one covering two of the six sectors in which CLAS is divided. Figure 12 shows how the ST surrounds the target, forming an hexagonal bent region called the nose, and a tubular region called the leg, where photomultiplier tubes are attached at its end. In this diagram the beam would come from the left.

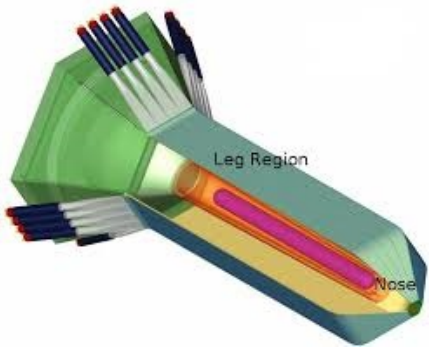

Figure 12: CLAS target and start counter (ST) diagram.

2.5.3 Toroidal Shield

Along the beam line, before reaching the target and surrounding it and the ST, we encounter the toroidal shield, also called minitorus. In our experiment it will not be of relevance since its meant to work for electron beam runs and we are dealing with a photon beam. The toroidal shield is a powerful magnet which prevents low energy electrons that can be created by electro-magnetic showers in the target from reaching and saturating the drift chambers. In figure 13 a diagram of the toroidal shield is shown, along many of the components that will be described in the next sections.

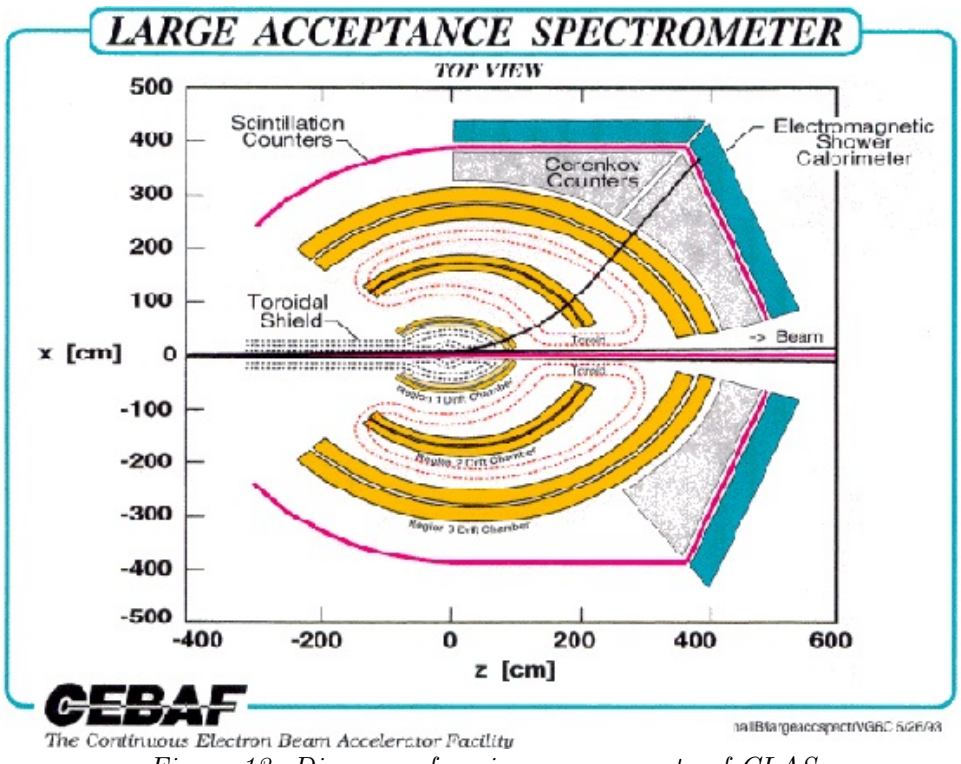

Figure 13: Diagram of various components of CLAS.

2.5.4 Main Torus Magnet

The main torus magnets are a set of six superconducting kidney-shaped magnets kept at $4.4°K$ using liquid Helium, which generate a toroidal magnetic field for CLAS. They are placed at 60° intervals, azimuthally along the beam line, and can generate a maximum field of about 3.5 T (supporting a current of about 3800 A), with a polarity such that positive particles are bent outward the beam line and negative ones toward it (although this can be reversed if required), not altering the azimuthal angle of them. The main torus serves the purpose of facilitating the identification of charged particles. In this experiment the current was set at half its maximum value (or half-field setting), which increases the small angle acceptance of the negative particles since they will bend less.

2.5.5 Drift Chambers

The drift chambers (DC) are the next layer of detectors, divided again in six separate sectors in correspondence to the CLAS ones. The drift chambers cover a polar angular range of 134° and an azimuthal angular range of 50°, which are in turn divided in three regions (Region 1, 2 and 3 as we keep getting farther away from the target) as shown in figure 13. Region 1 determines the initial track direction of charged particles, Region 2, placed between the main torus coils, is located where the curvature of the track is maximal, which means that a good energy resolution can be achieved and that by measuring the charged particles curvature radius their charge and momenta can be obtained, and finally Region 3 can be used to determine the final track direction of charged particles on their way towards the outlying detectors. Region 2 and 3 consist of two superlayers with six sense-wire layers, while region 1 has four, all surrounded by a gas composed of 88% argon and 12% carbon dioxide, which becomes ionized (by freeing electrons) when a charged particle transverse it. These electrons drift towards the wires, which creates a signal that will be used for trajectory reconstruction.

2.5.6 Cerenkov Counters

The Cerenkov counters (CC), which are used to discriminate between light and heavy charged particles, would be next, but we are not going to describe them in

detail since we did not use them in this experiment.

2.5.7 Time Of Flight Counters

After the Cerenkov counters we have (around 5 meters away from the target) the time of flight (TOF) Counters, which measures the total time of flight of the particles coming from the target. There are 57 of them per sector (342 in total), with photomultiplier tubes attached at the ends of each one. This counter, the ST and the tagger are used in particle identification, since they allow us to identify the time bucket that gave rise to a given event. The TOF Counters have a thickness of 5.08 cm and their length and width varies depending if they are in a forward position (32 cm and 15 cm minimum) or at very large angles (450 cm and 22 cm maximum), with a time resolution between 80 ps to 160 ps (with the longer counters having the worst resolution).

2.5.8 Electromagnetic Calorimeter

Finally, we have the Electromagnetic Calorimeter, which is divided in the forward (EC) and large angle parts (LAC, although this one was not used in this experiment), each one again divided following the six sector pattern of CLAS and covering a polar angle between 8° and 45°. There are 39 layers per sector, 10 mm thick and with 2.3 mm thick lead sheets in between, each with 36 sheets of scintillators rotated 120° every 13 of them. This calorimeter is used to measure the position, timing and energy of particles, including neutral ones (like neutrons and photons), and also to discriminate between electrons and π^-.

2.5.9 Triggering

Not every signal is treated as an event originated at the target since there are various sources that can trigger an unwanted signal, like electronic noise or cosmic radiation. It is the trigger (a logical operation that takes into account coincidences between the different detector systems) that determines which signals will be collected and written to magnetic tape by the Data Acquisition System (DAQ). Also the trigger system is meant to minimize the time lost to recording data while still receiving events, so it works on two-levels. On the first level, the signals from the

TOF scintillators are processed in 90 ns and then used as a start signal for the photomultiplier tubes Time to Digital and Analog to Digital Converters (TDC and ADC) readings and as a stop signal for the Drift Chamber signals, which allows all the signals to be digitalized. On the second level, the tracks are sorted by probability and selected if the ST and TOF counter sectors coincide. Finally, we ask for at least two charged tracks in different sectors in coincidence with a photon.

2.5.10 Running Conditions

To finalize this chapter we summarize some of the information already mentioned about the running conditions of the accelerator and mention other ones in table 1

e^- Energy Beam	5.715 GeV
Beam Polarization	Circular
e^- Current	60-65 nA
Tagger Range	5%-95% of e^- energy
Tagger Trigger Range	3.6-5.441 GeV
Torus Magnet	$\frac{1}{2}B_{max}$ (1930 A)
Target Length	40 cm
Target Center (z location)	90 cm
Target Material	$l\mathrm{H}_2$
Target Polarization	None
Start Counter Offset	0 cm
Radiator Thickness	10^{-4} radiation lengths
Collimator Radius	6.4 mm

Table 1: g12 experiment running conditions.

3 Analysis

In this chapter we give a very brief overview of how the signals of the detectors are converted to digital data and then processed to be ready for the computer analysis we wanted to do. Also, the derivation of some physical quantities and preliminary analysis of the signal are outlined. The analysis proper starts after the kinematic fit, which will supersede many of the early cuts done before it, although they are useful to give an introduction about data selection methods.

3.1 Data Preparation

In this section we outline how the signals from the detector was processed in order to be converted in data files.

3.1.1 Raw Data

The signals from the CLAS detector and the tagger pass through analog and time to digital converters, thus generating raw ADC and TDC readings. It is the DAQ system that converts this information and stores it in raw banks in BOS format. The a1c event reconstruction program uses the raw banks, the detector geometry parameters and the calibration constants to perform beam and event timing reconstruction, event vertex fitting, charged particle tracking and momentum measurement, neutral particle momentum measurement and particle identification, information that is stored in what is called cooked banks.

3.1.2 Data Skim

To skim our data means to convert our banks in BOS format to root files, which can be then read by the ROOT software. The skim imposes that at least one proton, one π^+ and one π^- be present, and that the photon beam energy must be higher that 3.6 GeV, thus limiting ourselves to the higher part of the energy spectrum. It also calculates the timings and time of flight of the particles, as we will describe below, and finally it corrects for lost energy as charged particles go from the event vertex through the target and the ST, considering their material characteristics and the particle path length.

3.2 Data Overview

In this section we will explain how various physical quantities were determined form the measurements described in sections 2.4 and 2.5, or how to obtain them from those variables (that will be present after the skimming), and we will plot them to see and understand their behavior. This was done using CERN's ROOT, which reads the root files and whose development was started by René Brun and Fons Rademakers in 1994. This software is optimized for high computing efficiency, something that has become a necessity for high energy physicists in order to process the enormous amounts of data obtained at present particle accelerators. In this section we will also describe part of the preliminary analysis, as stated before, where some of the cuts were studied. The process of selecting appropriate cuts to get rid of reactions we are not interested is a tedious one, one has to try many possibilities in different orders and combinations, and the high amount of data slows down this process significantly. It would be almost impossible and too dense to put all of this in detail in this work, therefore mostly at the beginning each cut will be presented individually to highlight its effect on the data, and after on the sequence of all the cuts presented in each case will be applied in sequence in one plot to visualize the cutting of the data and what is left at the end. Most of the plots show how many events are plotted after applying the corresponding cut and all of those listed before it to avoid cumbersome labels, unless specified.

3.2.1 Energy Spectrum

Figure 14 shows the photon beam energy spectrum, which is determined from the energy difference between the beam and bent electrons [28], the former is known from the running conditions while the latter is measured as described in section 2.4. We started our analysis by imposing a cut on the photon beam energy of

$$3.6\,GeV < E_\gamma \tag{3.1}$$

which is represented on the plot. The cut requiring energies below 5.3 GeV was done later in the analysis.

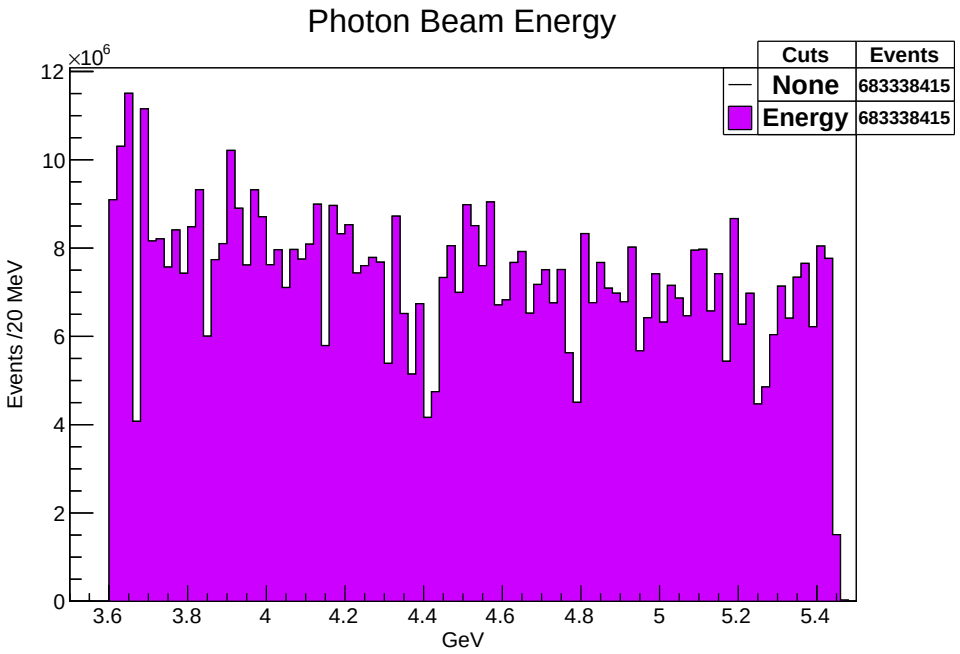

Figure 14: Photon beam energy spectrum. All events comply with the cut imposed on equation 3.1, as expected.

The depleted regions that can be seen in this plot correspond to inefficiencies in the tagger T-counter paddles, measurement needed to pinpoint the bunch of electrons in the beam corresponding to the produced photon. All energies already comply with the cut imposed because this was set on the skim. This can be seen from the fact that the number of events before (which are the events that passed the skim) and after the application of this energy cut is the same (683338415). Although the application of this cut after the skim can appear redundant, after performing the kinematic fit it will be not since some values could be changed by it.

3.2.2 Event Vertex

A vertex can be determined for each particle whose trajectory has been reconstructed as explained in section 2.5.5. In our case this can be done to the proton, the π^+ and the π^-. The vertex of a particle is determined by taking into consideration the particle distance of closest approach (DOCA), which is the minimum distance between the trajectory of the particle and the photon beam line. This defines a DOCA vector, whose middle point is what we call the vertex of the particle. Then we define the event vertex as the middle point between the vertex of

the π^+ and the π^- particles.

In figures 15 and 16 we can recognize the shape and dimensions of the target cell as we plot the vertex coordinates for each event. Since the reactions we want to focus must have taken place inside the target, we can restrict the event vertex position to the region occupied by it by performing cuts taking into account the physical dimensions of the target (described in section 2.5.1), that is, by imposing

$$x_v^2 + y_v^2 < 4\,cm^2 \tag{3.2}$$

$$-110\,cm < z_v < -70\,cm \tag{3.3}$$

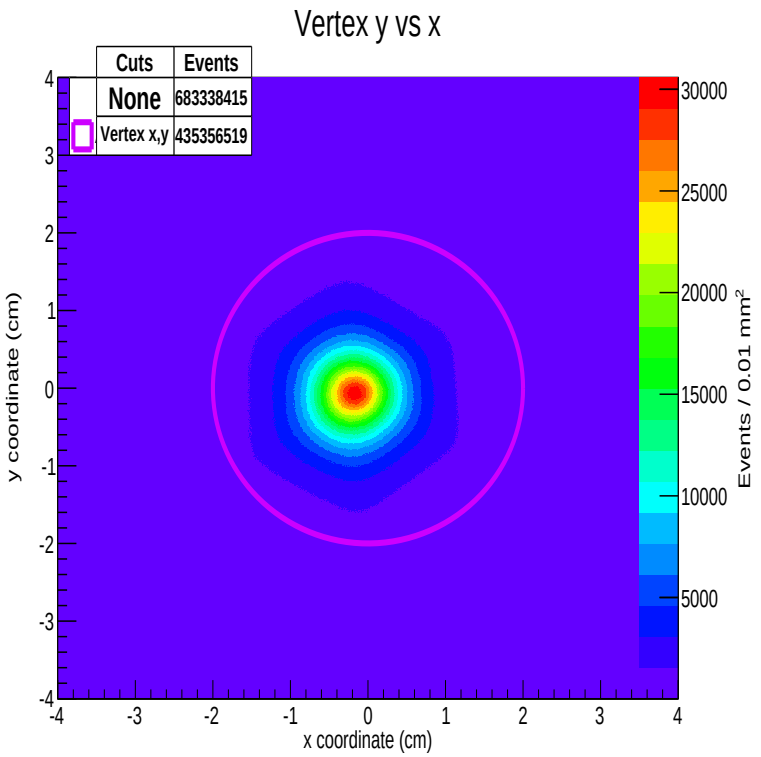

Figure 15: Event vertex distribution for the xy plane. The x and y vertex cut, from equation 3.2, is represented.

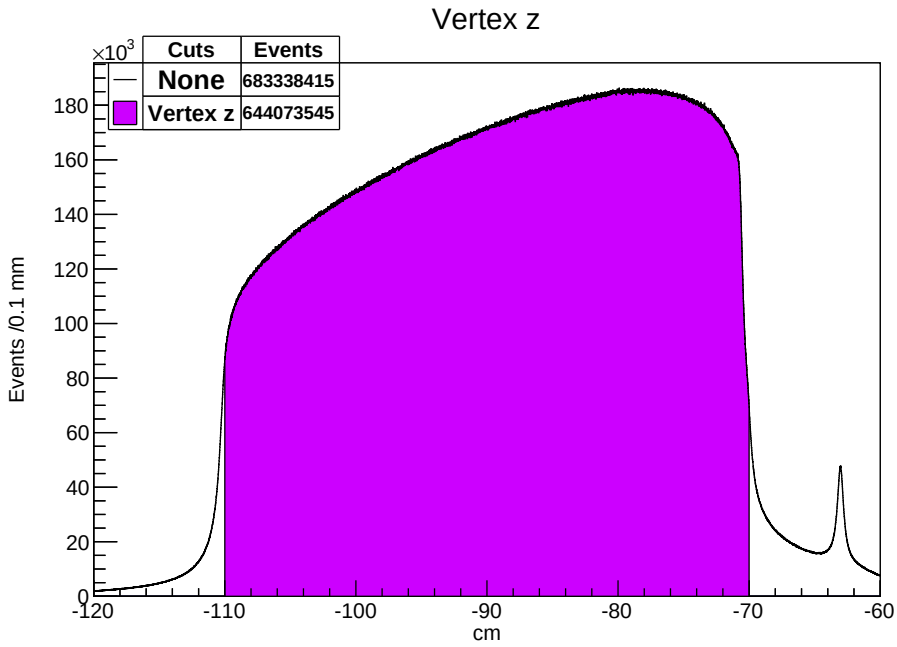

Figure 16: Event vertex distribution for coordinate z. The z vertex cut, from equation 3.3, is represented.

In figure 16 the center of CLAS would be at 0 cm, therefore the beam comes from the left since the target was positioned upstream. The peak at around -63 cm comes from a piece of metal attached to the target which divides it in order to create a vacuum.

3.2.3 Vertex Timing

The vertex timing of the charged particles are calculated in the skim as

$$Timing = t_{tag} - t_{ST} \tag{3.4}$$

where the first term is the vertex time measured by the tagger as described in section 2.4 and the last term is the vertex time measured by the ST as described in section 2.5.2. In both cases the propagation times of the photon and the charged particles are taken into account [29], that is, after the RF bucket is identified with the T-counters measurement, the time the photon reach the center of the target is easily calculated and then corrected by the z coordinate of the vertex, and the time obtained by the ST is also corrected by the time from track to the PMT.

The timings of the charged particles are represented in figures 17 to 19, where the RF buckets and their expected 2.004 ns separation can be recognized in figures 18

and 19, therefore to ensure that the tagged photon is responsible of the event that produced those charged particles we discard the events that does not comply, for each charged particle, the timing cut

$$|Timing| < 1\,ns \tag{3.5}$$

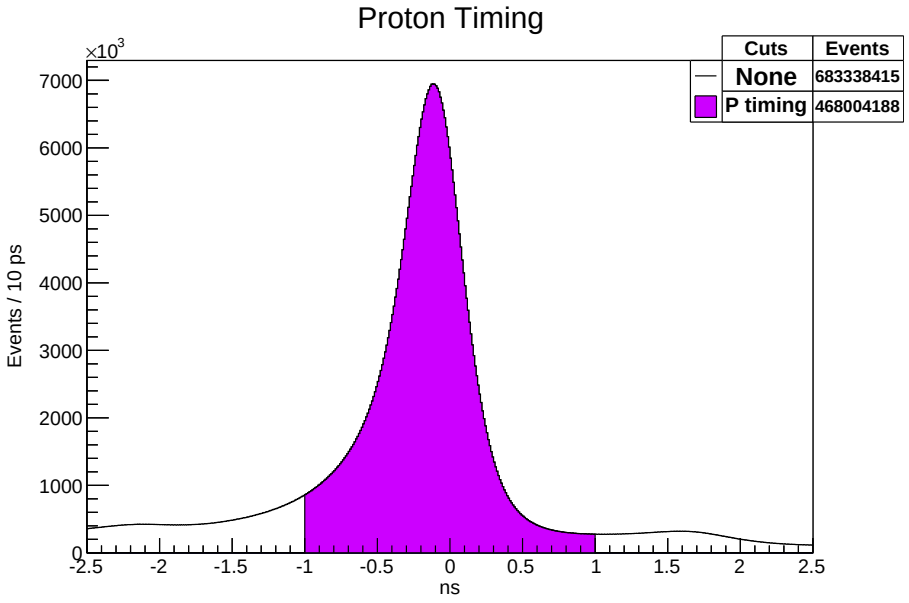

Figure 17: Proton timing plot. The proton timing cut, from equation 3.5, for the proton case, is represented.

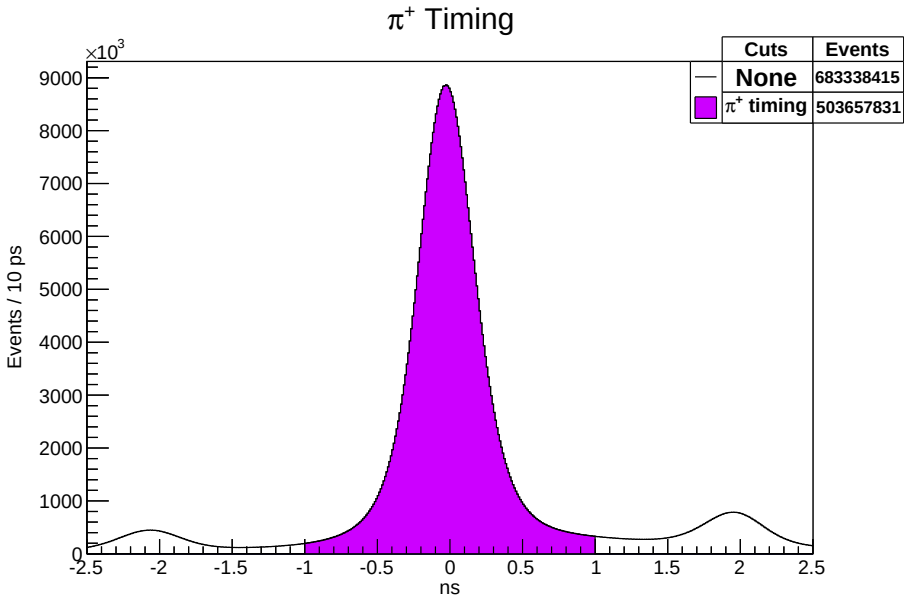

Figure 18: π^+ timing plot. The π^+ timing cut, from equation 3.5, for the π^+ case is represented.

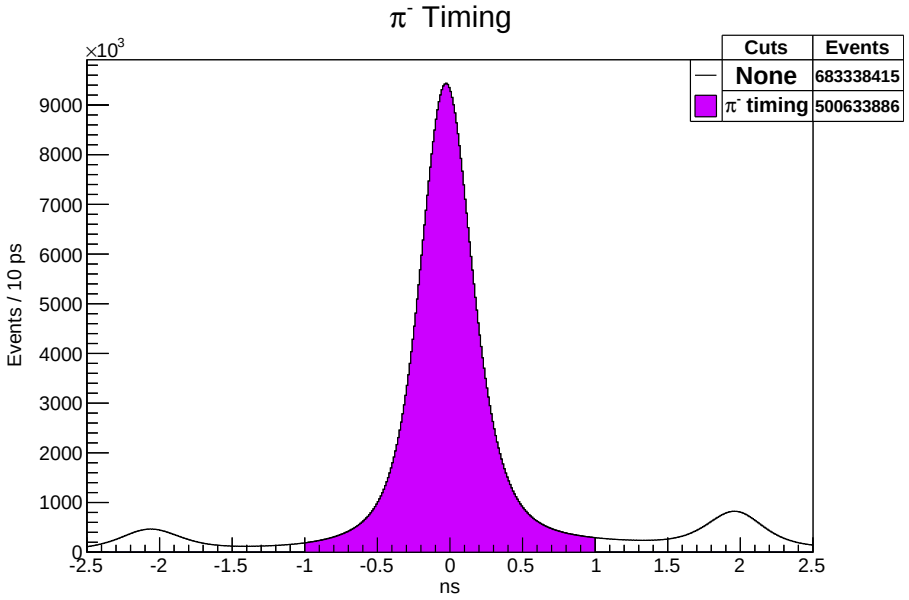

Figure 19: π^- timing plot. The π^- timing cut, from equation 3.5, for the π^- case is represented.

3.2.4 Differential Time Of Flight

The differential time of flight of the charged particles is calculated in the skim as

$$\Delta ToF = ToF_{meas} - ToF_{calc} = (t_{SC} - t_{ST}) - \frac{l}{c}\sqrt{1 + \left(\frac{m}{p}\right)^2} \tag{3.6}$$

where the term between parenthesis is the measured time a particle takes to travel from the target to the TOF counter, reached at time t_{SC} (measured as described in section 2.5.7), while the last term is that same calculated time, where l is the length of the track, c the speed of light, p the momentum of the particle and m its mass. The last relation is immediately derived from $ToF_{calc} = \frac{l}{v}$ and $p = \gamma(v)mv$, and then not forgetting to write m and p in eV.

When we say that m is the mass of the particle we are assuming that it has been correctly identified. If this were the case, we would expect a null differential time of flight. We can put this into test by imposing the cuts

$$(\Delta ToF_{\pi^+})^2 + (\Delta ToF_{\pi^-})^2 < 4\,ns^2, \quad (\Delta ToF_{proton})^2 + (\Delta ToF_{\pi^-})^2 < 4\,ns^2 \tag{3.7}$$

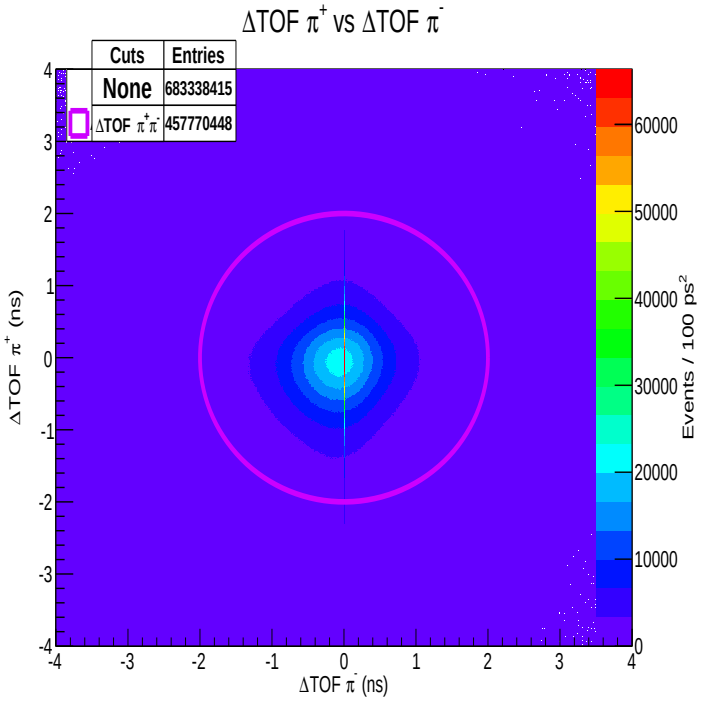

Figure 20: π^+ vs π^- differential time of flights. The ΔToF cut from the left side equation 3.7 is represented.

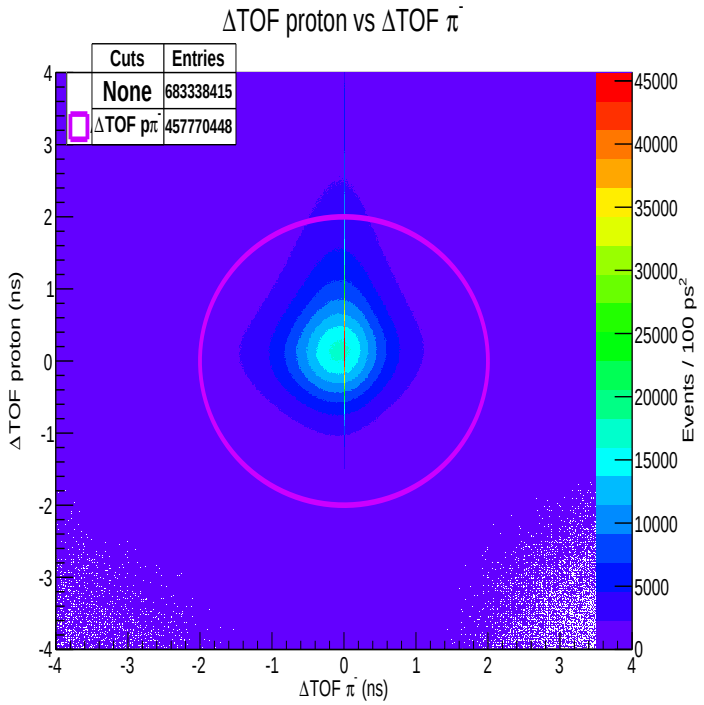

Figure 21: proton vs π^- differential time of flights. The ΔToF cut from the right side equation 3.7 is represented.

We can see that in the great majority of the events the particles were correctly

identified. In fact, the highly concentrated event vertical distribution correspond to identified π^-, which is expected since it is easier to differentiate from the proton and the π^-.

From now on in this chapter all the previous cuts (energy, vertex, timings and differential time of flight, set of cuts that will be denominated on the plots when they are the only ones applied as "E, V & T") will be applied, even when not explicitly stated (this with the intention of avoiding cumbersome notation when other cuts are also applied).

3.2.5 $p\pi^+\pi^-$ Missing Mass

Writing the products of the ω decay, as shown in figure 22, the reaction we are interested is $\gamma p \to p\pi^+\pi^-(\pi^0)$, where the missing particle (that needs to be reconstructed) is indicated by the parenthesis. The principal branching ratios of the ω decay modes are $\pi^+\pi^-\pi^0$ (89.2 $\pm$ 0.7%), $\pi^0\gamma$ (8.28 $\pm$ 0.28%) and $\pi^+\pi^-$ (1.53 $^{+0.11}_{-0.13}$%) [30].

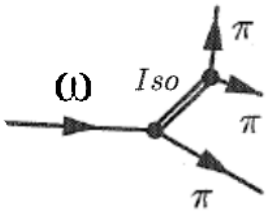

Figure 22: Omega decay.

After a particle is identified we know its mass, and its momentum can be calculated using $p = qrB$, where q is the electric charge of the particle, B the magnitude of the magnetic field caused by the Main Torus Magnet and r the curvature of its trajectory. Then we can calculate its energy using the relation $E = \sqrt{p^2c^2 + m^2c^4}$. We can also know the polar and azimuthal angles of the momentum from the reconstructed track.

We can then reconstruct the photon, target proton, scattered proton, $\pi+$ and $\pi-$ four-momentums. Since the four-momentum (or alternatively, energy and momentum) is conserved (its magnitude is the mass of the corresponding particles), at the end of the process the four-momentum that is missing from a given sys-

tem can be a useful quantity. For the reaction we are interested, the missing four-momentum of the $p\pi^+\pi^-$ should correspond to the four-momentum of the π^0 particle, which means that the missing mass of that system (the magnitude of the missing four-momentum) should correspond to the π^0 mass. Knowing this, we could filter most of the undesired reactions (those that do not produce $p\pi^+\pi^-\pi^0$) by rejecting events where

$$|mm^2_{p\pi^+\pi^-} - m^2_{\pi^0}| > 0.06\, GeV^2 \tag{3.8}$$

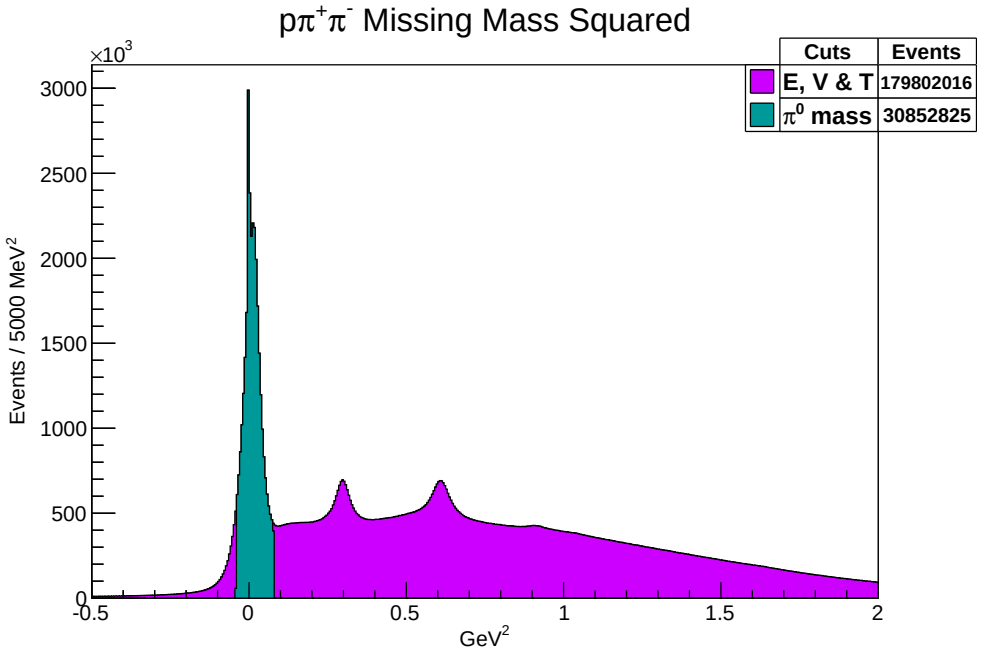

Figure 23: Missing mass squared (mm^2) of the $p\pi^+\pi^-$ system. The missing mass cut, from equation 3.8, is represented. From left to right we can recognize the π^0, the η and the ω, since they should have a squared mass of 0.018, 0.3 and 0.61 GeV^2 respectively.

The particular value of this cut can be fine-tuned by observing its effect on the data, but the use of the particular value $0.06\, GeV^2$ was recommended considering previous similar analysis.

3.2.6 Missing Momentum

As can be seen in figure 23, since the π^0 mass is very small it would be very difficult to distinguish between the $p\pi^+\pi^-$ and $p\pi^+\pi^-\pi^0$ reaction channels using only the $p\pi^+\pi^-$ missing mass. In fact, the cut we applied does not distinguish between the

two cases, since those events with no missing mass are allowed through it, and narrowing it would cause a great loss of the desired signal. Another possibility would be to consider also the missing momentum of the $p\pi^+\pi^-$ system.

From the cartesian components of the missing four-momentum and the fact that we are defining the z direction as that of the photon beam, it is straightforward to calculate and plot the transversal (to the beam line) versus longitudinal (along the beam line) missing momentums of the $p\pi^+\pi^-$ system (or $mp^t_{p\pi^+\pi^-}$ vs $mp^l_{p\pi^+\pi^-}$), as shown in figure 24, where we can recognize two groupings: events accumulated at large longitudinal missing momentum, which come from misidentified photon beams, and events accumulated around the origin, which come from the exclusive two-pion production reaction.

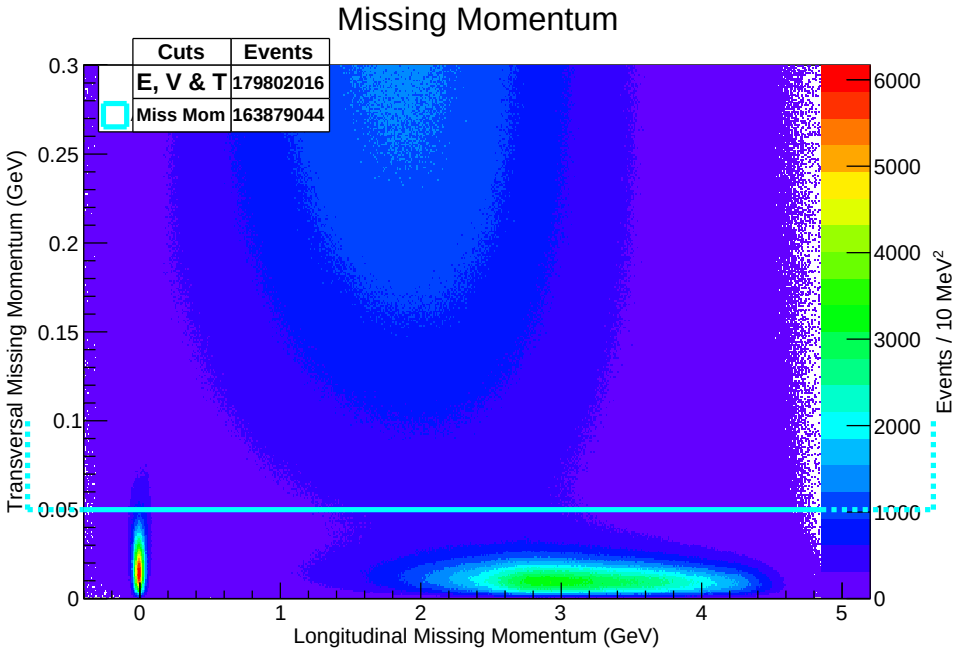

Figure 24: Missing momentum of the $p\pi^+\pi^-$ system. The missing momentum cut, from equation 3.9, is represented.

From figure 24 we can see that we can discard these two groups by imposing the missing momentum cut

$$mp^t_{p\pi^+\pi^-} > 0.05\,GeV \tag{3.9}$$

3.2.7 t' Distribution

As we said before, we are interested in the t-channel reaction $\gamma p \to p\omega$, which is shown in figure 25. In this situation the Mandelstam variable t becomes

$$t = (P^{\mu}_{target\,proton} - P^{\mu}_{scattered\,proton})^2 \tag{3.10}$$

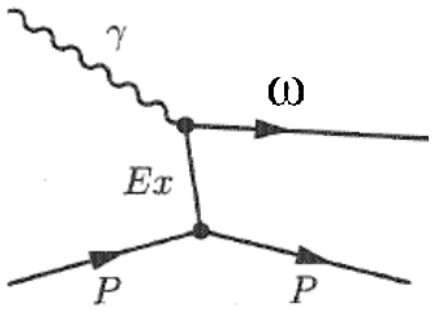

Figure 25: Reaction we are interested.

We define the four-momentum transfer t' as

$$t' = t - t_{min} \tag{3.11}$$

where t_{min} is the value of t corresponding to a null scattering angle. The details of how we can compute it from our data are explained in Appendix A.

Low $|t'|$ events correspond to low energy scattered protons, which are usually poorly measured in CLAS, therefore we will reject these kind of events by imposing

$$t' < -0.6\,GeV^2 \tag{3.12}$$

Diffractive events are those where there is an exchange of a meson between the target proton and the photon instead of a "knock-on" collision, where transfered momentum is greater. High $|t'|$ events would correspond to non-diffractive (non t-channel) events, which means that we are going to reject also events where

$$-3.5\,GeV^2 < t' \tag{3.13}$$

The reason behind the particular choice of these values will be explained when this cut is applied after the kinematic fit is performed on the data.

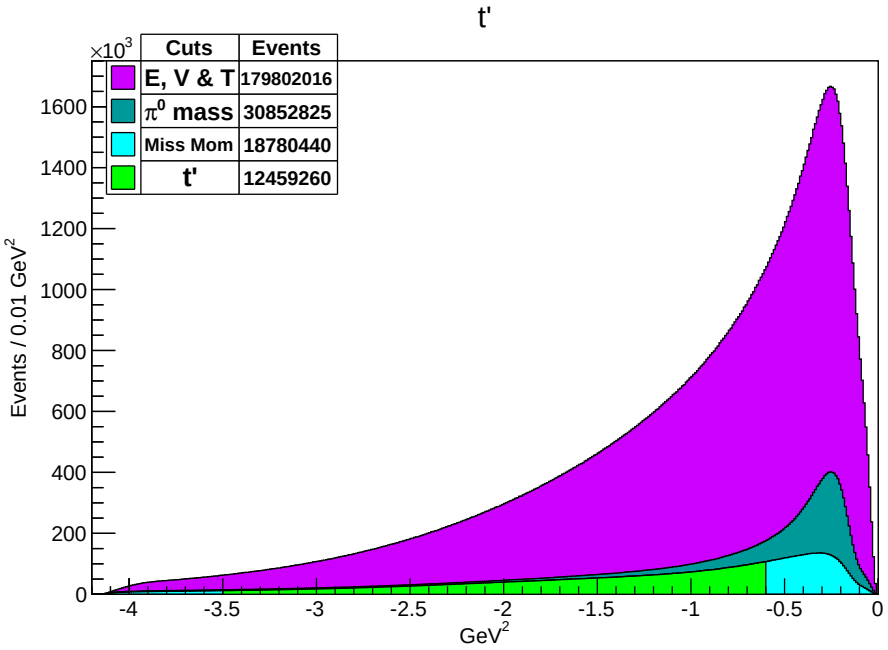

Figure 26: Four-momentum transfer distribution. The t' cut, from equations 3.12 and 3.13, and the previously described cuts are represented.

3.2.8 Baryon Channels

This and the next subsections will serve as an overview of what is contained and can be viewed from the original signal, although the main reason this was done was because the original idea of this work was to study the possible existence of exotic particles in the signal since we will not use this in our study of the ω decay. In our analysis proper, the baryon channels will be discarded by restricting ourselves to the ω mass range.

Baryon channels can appear when an incident photon excites the target proton to a Δ or an N^*, which then decays to a proton and a pion, as shown in figure 27.

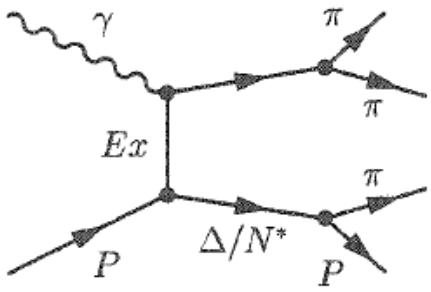

Figure 27: Baryon background reaction.

In the $p\pi^+$ mass spectrum, shown in figure 28, we can identify the $\Delta^{++}(1232)$. We can discard these events by performing a $p\pi^+$ mass cut and rejecting events where

$$m_{p\pi^+} < 1350 MeV \tag{3.14}$$

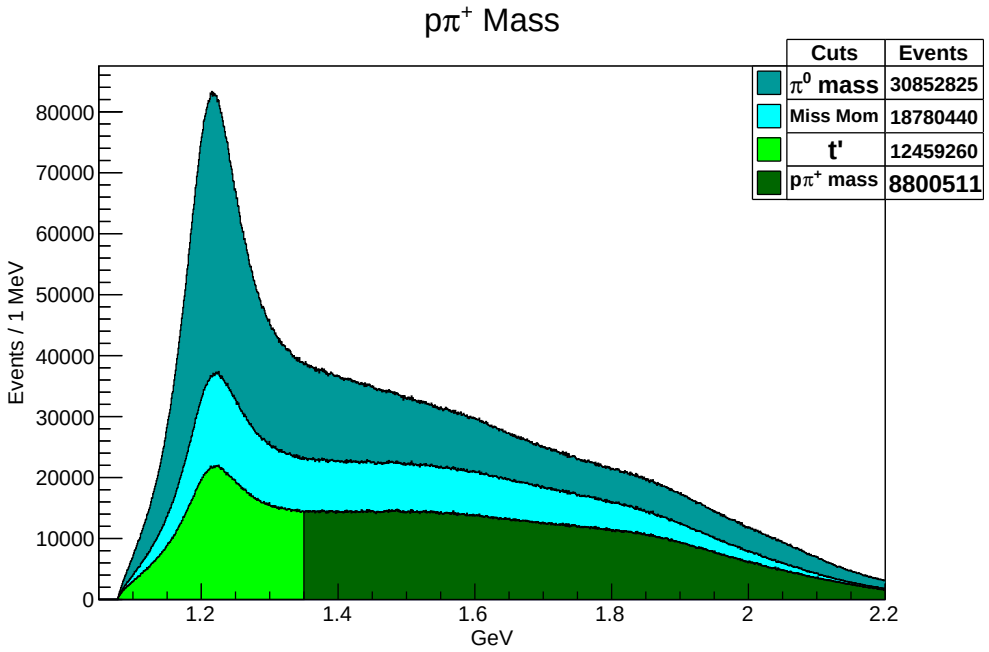

Figure 28: Mass spectrum of the $p\pi^+$ system. The $p\pi^+$ mass cut, from equation 3.14, and the previously described cuts are represented.

Also in the $p\pi^-$ mass spectrum, shown in figure 29, we can identify the $\Delta^0(1232)$, and more clearly the $N^*(1530)$ and the $N^*(1650)$.

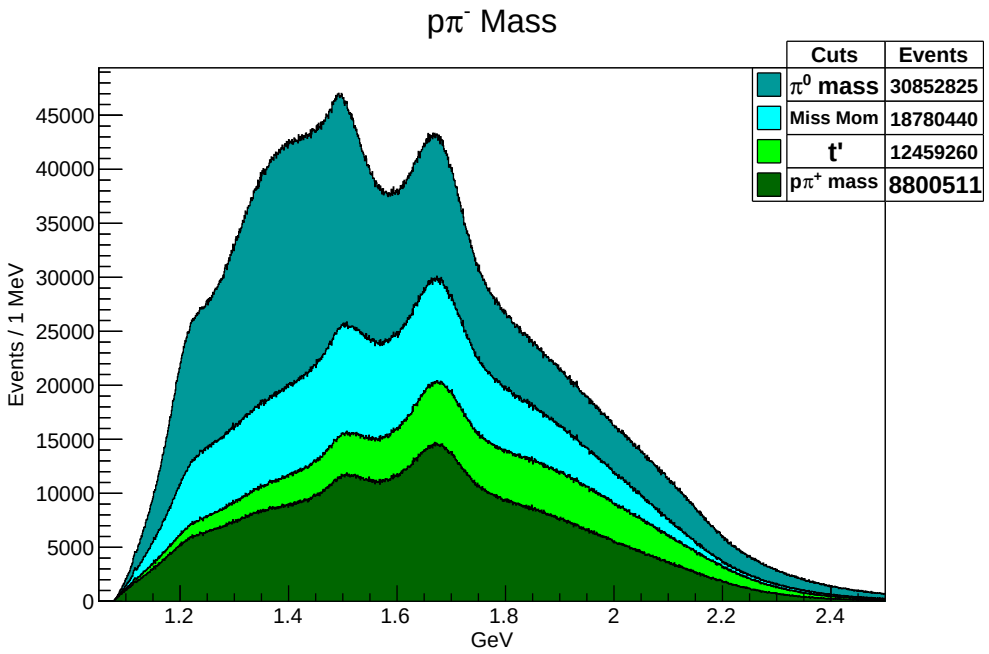

Figure 29: Mass spectrum of the $p\pi^-$ system. All the previously described cuts are represented.

Finally, in the $\pi^+\pi^-$ missing mass spectrum, shown in figure 30, we can identify the $\Delta^+(1232)$, the $N^*(1530)$ and the $N^*(1650)$.

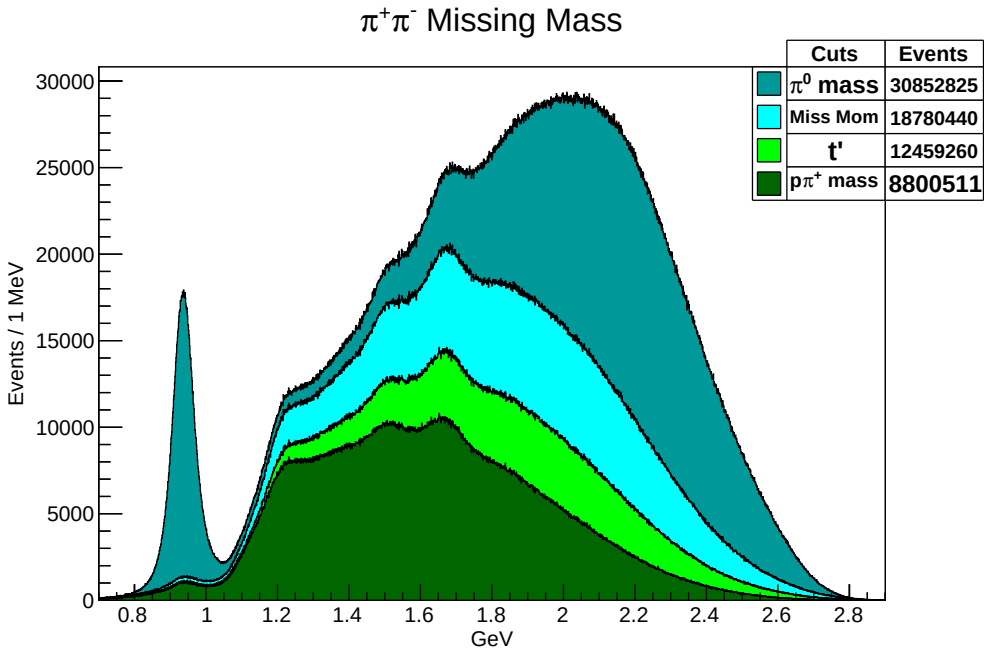

Figure 30: Missing mass spectrum of the $\pi^+\pi^-$ system. All the previously described cuts are represented.

In the last two cases there were no new cuts considered to remove these background channels since those signals were more or less suppressed by the application of all the previously mentioned cuts, and additional cuts with the sole purpose of remove those resonances would also discard much of the useful data.

3.2.9 Di-pion Mass Spectrum Plots

We can also see that in the mass spectrum of the di-pion channels we can recognize the neutral, positive and negative $\rho(770)$ in figures 31, 32 and 33 respectively, while the $f2(1270)$ appears in figure 31.

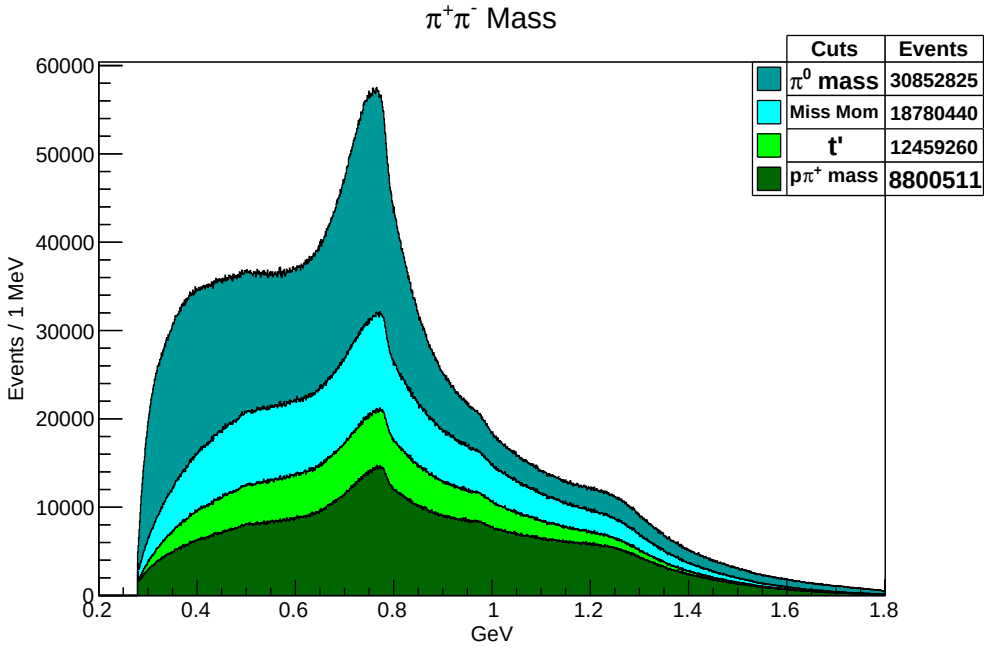

Figure 31: Mass spectrum of the $\pi^+\pi^-$ system. All the previously described cuts are represented.

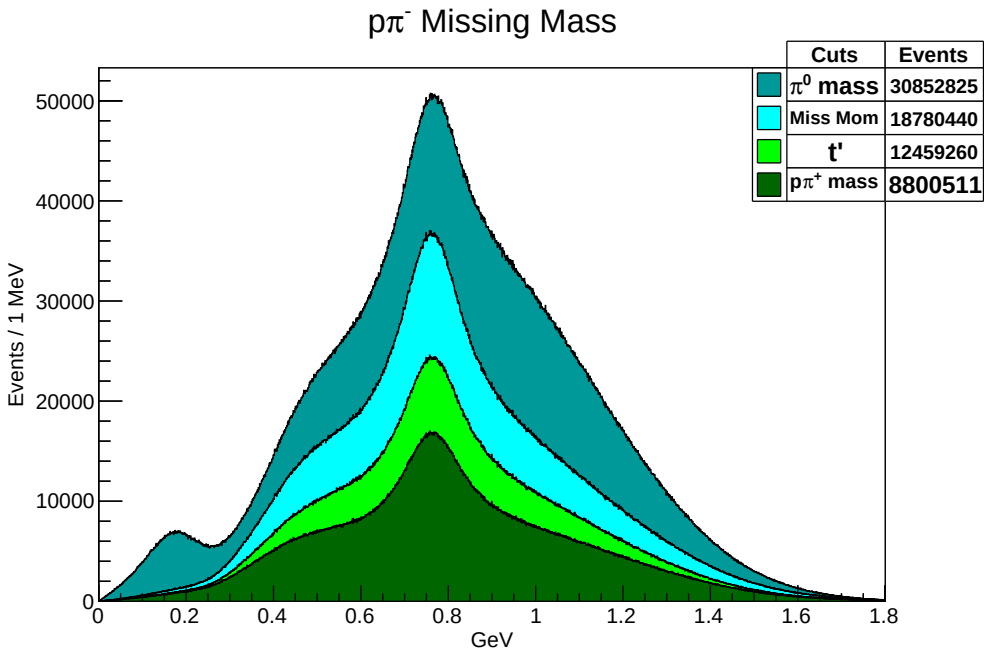

Figure 32: Missing mass spectrum of the $p\pi^-$ system. All the previously described cuts are represented.

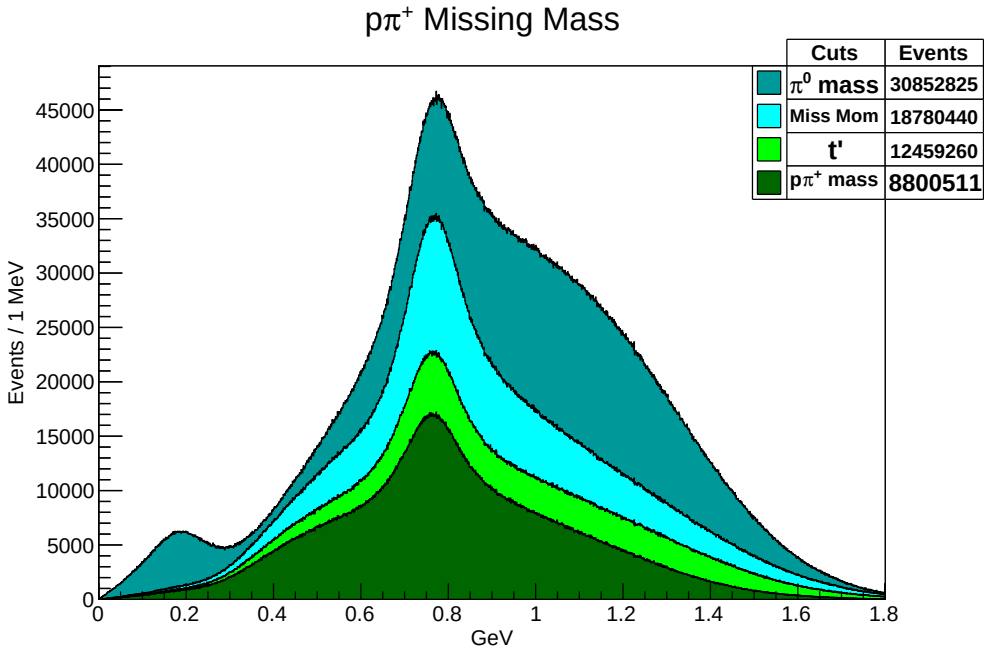

Figure 33: Missing mass spectrum of the $p\pi^+$ system. All the previously described cuts are represented.

From figures 34, 35 and 36 we can see the correlations between the $p\pi$ and the $\pi\pi$ systems. Here only the missing mass and missing momentum cuts of the $p\pi^+\pi^-$ system are applied since this is the stage where these signals are slightly cleaner,

can be seen from figures 28 to 33

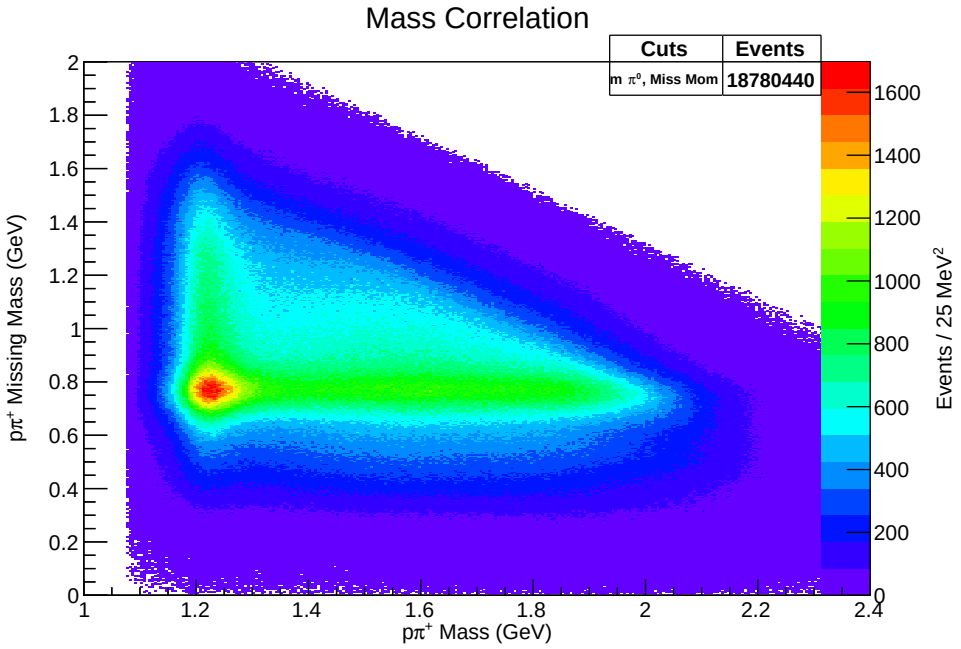

Figure 34: Correlations between $\pi^-\pi^0$ and $p\pi^+$ systems.

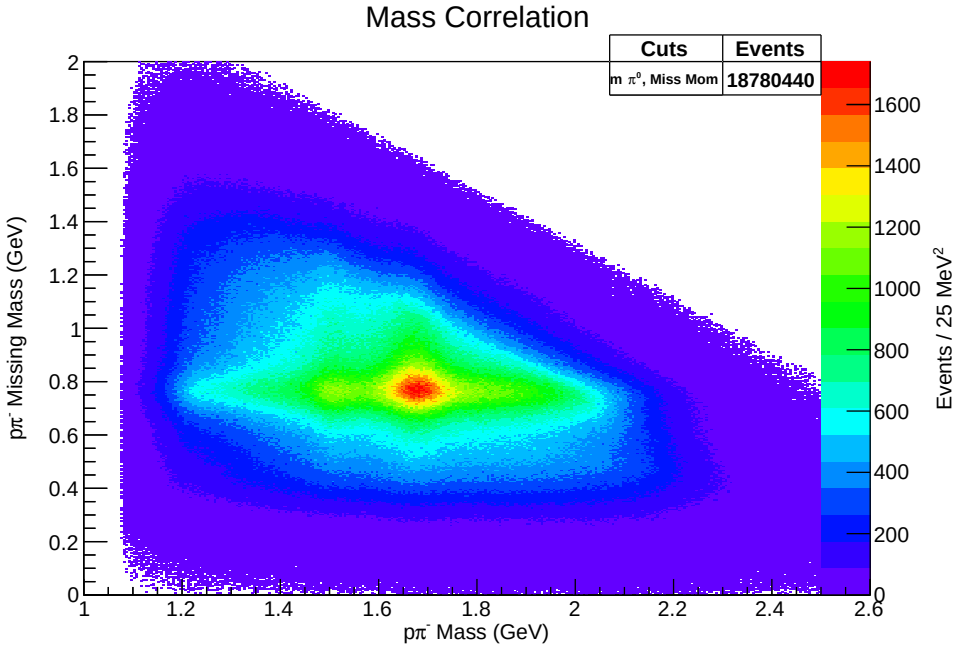

Figure 35: Correlations between $\pi^+\pi^0$ and $p\pi^-$ systems.

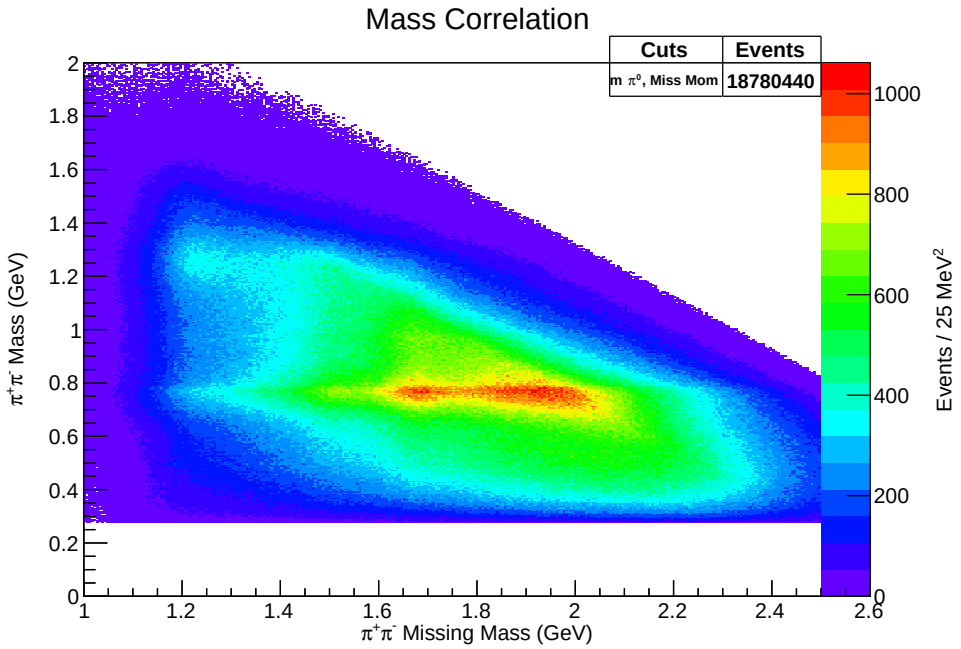

Figure 36: Correlations between $\pi^+\pi^-$ and $p\pi^0$ systems.

It can be seen in figures 34 and 35 that the $\Delta^{++}(1232)$ is correlated with the $\rho^-(770)$ and the $N^*(1650)$ with the $\rho^+(770)$ respectively, while in figure 36 the $\Delta^+(1232)$ can be seen correlated with the $f2(1270)$.

3.2.10 ω Mass Spectrum

We can recognize in figure 37 the $\omega(782)$ (whose decay we want to analyze) and a combination of the $a1(1260)$ and the $a2(1320)$. The hump above 1600 MeV could be because of the $p2(1670)$, $\omega(1650)$ or the $\omega3(1670)$.

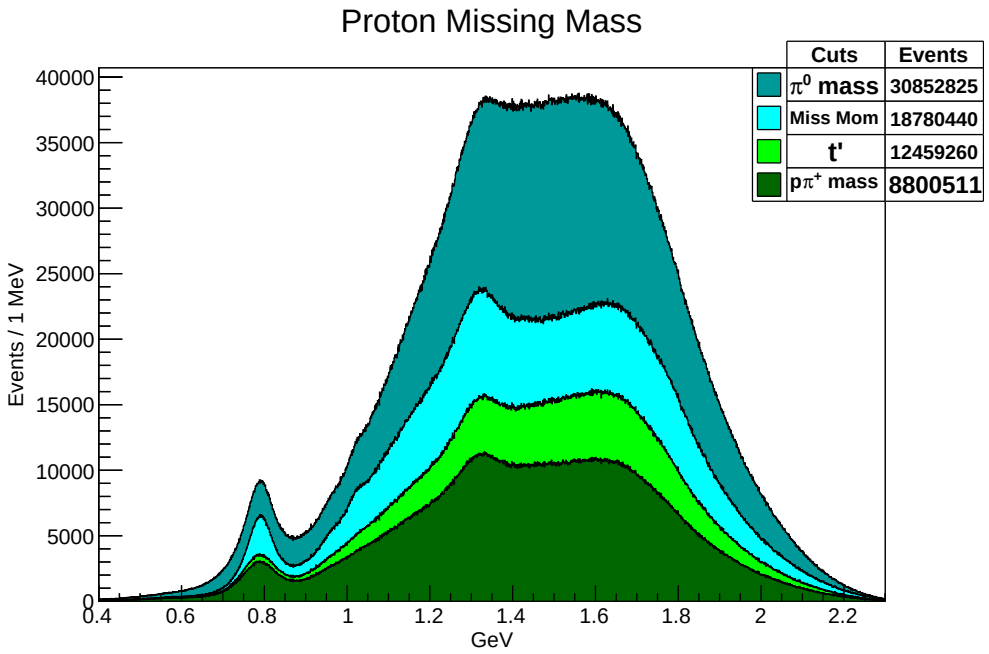

Figure 37: Proton missing mass.

As stated before, the purpose of this part of the work was to visualize the contents of the signal. In what follows we will focus on the ω mass range, thus avoiding background from the barionic channels.

3.3 Kinematic Fit

We will start by applying a kinematic fit, written and developed by Dustin Keller [31], directly on the skimmed data. The purpose of this procedure is to impose conservation of energy, momentum, and vertex positioning, all quantities that could have been misread because of drift chamber tracking errors (mostly due to resolution uncertainties), energy loss and multiple scattering effects. Also it will give us a probability about our hypothesis that the reaction is effectively $\gamma p \to p\pi^+\pi^-(\pi^0)$.

The kinematic fit needs as an input a matrix of correlation, which is created during track reconstruction taking into account the possible causes of error described in the previous paragraph. The method of least squares is used (which minimizes the sum of the squares of the errors), and all the constraints is handled with the method of Lagrange multipliers.

We start our formulation by denoting the m unknown parameters as $\vec{x}$ and the n

measurable parameters as $\vec{y}$, while the actual measured quantities are $\vec{\eta}$ and their errors $\vec{\epsilon}$. If we have r constraints, then

$$\vec{\epsilon} = \vec{\eta} - \vec{y}, \qquad f_k(\vec{x}, \vec{y}) = 0, \quad k = 1, 2, ..., r \tag{3.15}$$

In our case we have

$$f = \begin{bmatrix} E_\gamma + M_{tp} - E_{sp} - E_{\pi^+} - E_{\pi^-} - E_x \\ \vec{p}_\gamma - \vec{p}_{sp} - \vec{p}_{\pi^+} - \vec{p}_{\pi^-} - \vec{p}_x \end{bmatrix} = \vec{0} \tag{3.16}$$

where tp and sp refers to the target and scattered proton, and x to the missing particle, π^0, whose mass we fix to perform this fit, leaving us with three unknowns and the four constraints written from energy and momentum conservation.

We define the pull of the i^{th} measured quantity by

$$z_i = \frac{\epsilon_i}{\sigma_{\epsilon_i}} = \frac{\eta_i - y_i}{\sqrt{\sigma^2_{\eta_i} - \sigma^2_{y_i}}} \tag{3.17}$$

The z_i's should be distributed normally with mean 0 (if this is not the case, systematic errors would be the cause) and standard deviation 1 (if the errors have been overestimated, the standard deviation would be smaller, and if they have been underestimated, higher).

The "goodness of the fit" can be assessed by means of the confidence level of the fit

$$CL = \int_{\chi^2}^{\infty} f(z, n) dz \tag{3.18}$$

with

$$\chi^2 = \sum_i \left(\frac{\eta_i - \eta_i'}{\sigma_{\eta_i}} \right)^2 \tag{3.19}$$

where η_i' is the expected value for the measurement, which depends on the data points that are being tested, and $f(z, n)$ is the χ^2 probability density function, n being its degrees of freedom. Maximizing the probability density function is equivalent to minimizing χ^2. The confidence level is a measure of the probability that a given event has a theoretical χ^2 greater than the given from the fit. Events

described by the fit hypothesis will have a flat distribution between 0 and 1, and those poorly described by it will peak at 0. We will perform the corresponding cuts below.

3.4 Data Selection

We will describe the cuts that were effectively performed on kinematic fitted data, since many cuts previously described turn out to be unnecessary after the kinematic fit, and there will be some new ones.

3.4.1 Energy And Time Cuts

We will start by performing the same energy, timing and differential time of flight cuts described in sections 3.2.1, 3.2.3 and 3.2.4.

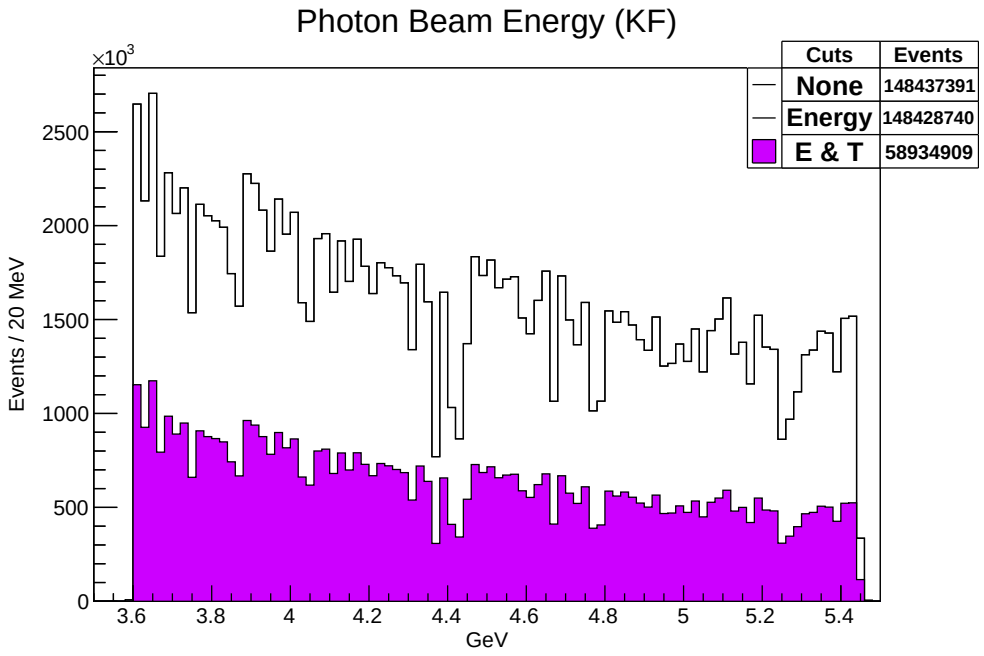

Figure 38: Energy spectrum. The energy and time related cuts, denominated here as "E & T", are represented.

As we can see in figure 38, there were 8651 events that did not comply with the energy cut even after this condition was imposed in the skim, this is because the kinematic fit changed the energy values of some events. The kinematic fitted timing and differential time of flight plots are very similar to the ones previously

shown, therefore we will not present them again here, although it must be said that the asymmetries seen before in the case of the proton timing disappear after all the cuts (specially the ω mass cut, described in the next section) are applied.

3.4.2 ω Mass Cut

As said before, we will focus on the ω mass region by imposing on the proton missing mass an omega mass cut of

$$750\,MeV < mm_{proton} < 830\,MeV \tag{3.20}$$

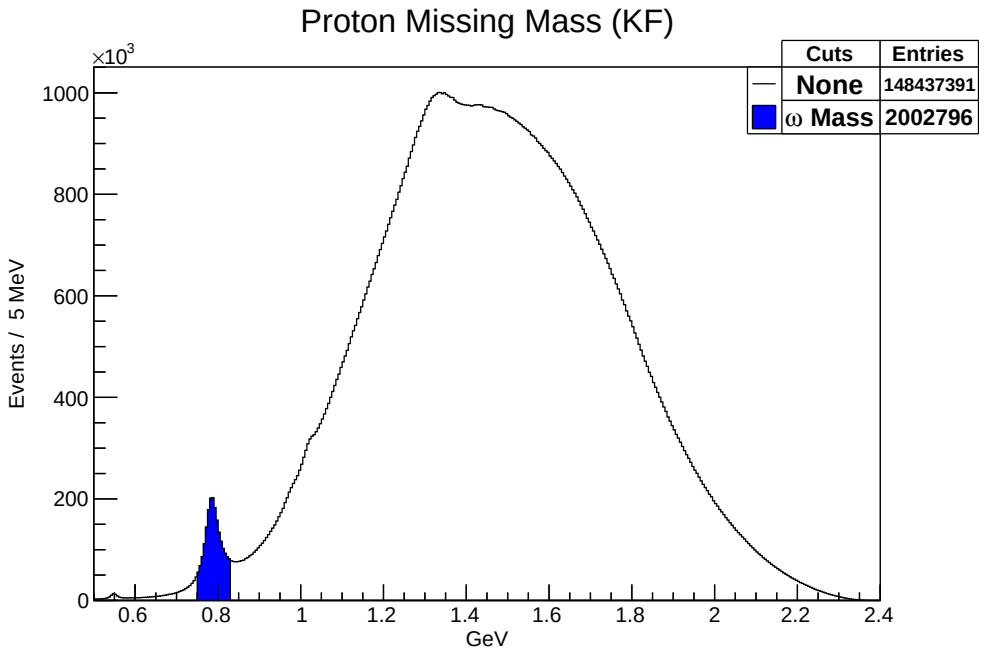

Figure 39: Proton missing mass. The ω signal is clearly visible, and the omega mass cut of equation 3.20 is represented.

The particular values of this cut were chosen to select all of the ω signal and part of the background, although this is not entirely apparent at this stage because we are showing the effects of each cut individually on the data when, as stated before, each of them had to be fine tuned back and forth depending on the effect all the others had on the selected data.

3.4.3 Pull Cuts

Then we impose that the Pulls of the kinematic fit verify

$$|Pull\, i| < 1 \text{ for } i \text{ from 0 to 9}, \qquad Pull\, Prob > 0.15 \tag{3.21}$$

where $i = 0$ correspond to the photon energy, $i = 1, 2, 3$ to the proton momentum, $i = 4, 5, 6$ to the π^+ momentum and $i = 7, 8, 9$ to the π^- momentum, in each case the first index refers to its magnitude and the other two to angular quantities to define its direction, and $Pull\, Prob$ is the confidence level.

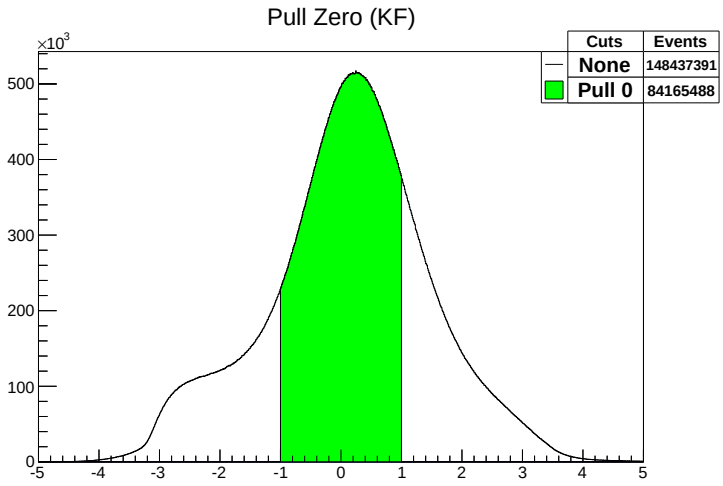

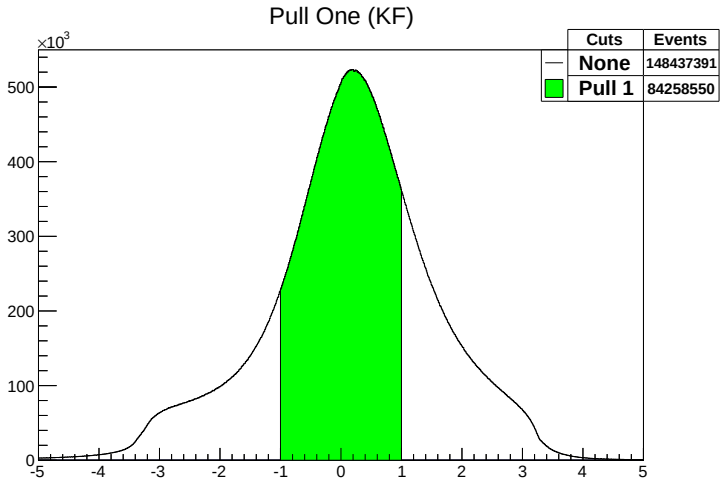

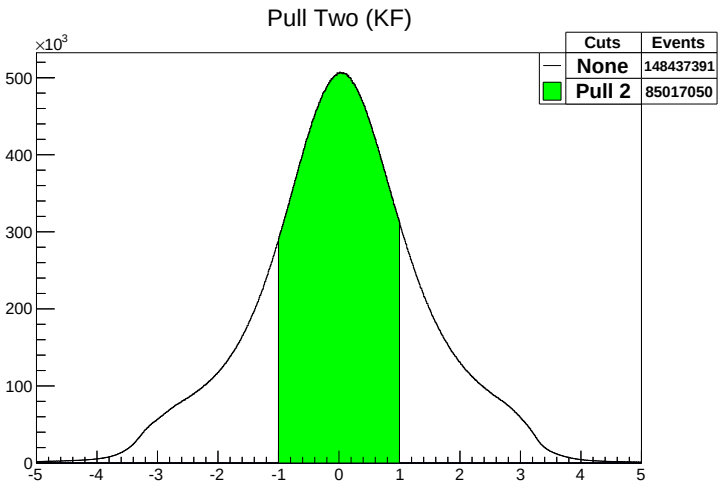
Pull Two (KF)
×10^3
Cuts
Events
None
148437391
Pull 2
85017050
500
400
300
200
100
0
-5
-4
-3
-2
-1
0
1
2
3
4
5

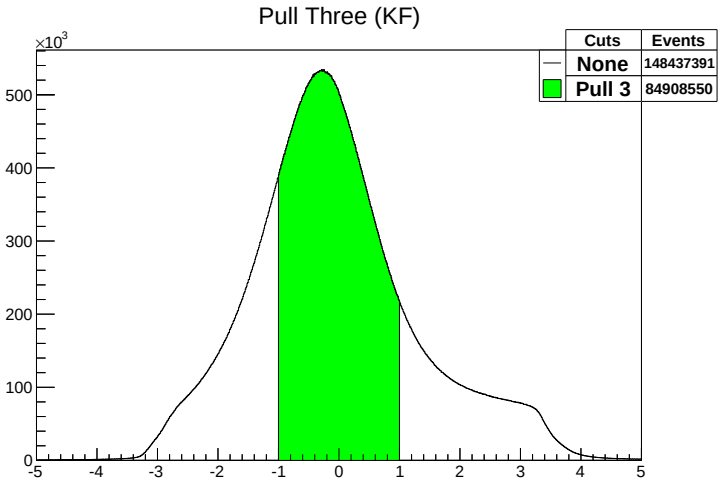
Pull Three (KF)
×10^3
Cuts
Events
None
148437391
Pull 3
84908550
500
400
300
200
100
0
-5
-4
-3
-2
-1
0
1
2
3
4
5

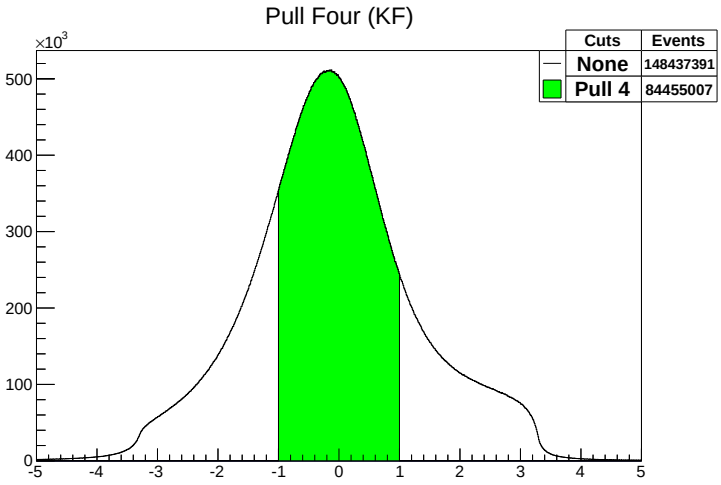
Pull Four (KF)
×10^3
Cuts
Events
None
148437391
Pull 4
84455007
500
400
300
200
100
0
-5
-4
-3
-2
-1
0
1
2
3
4
5

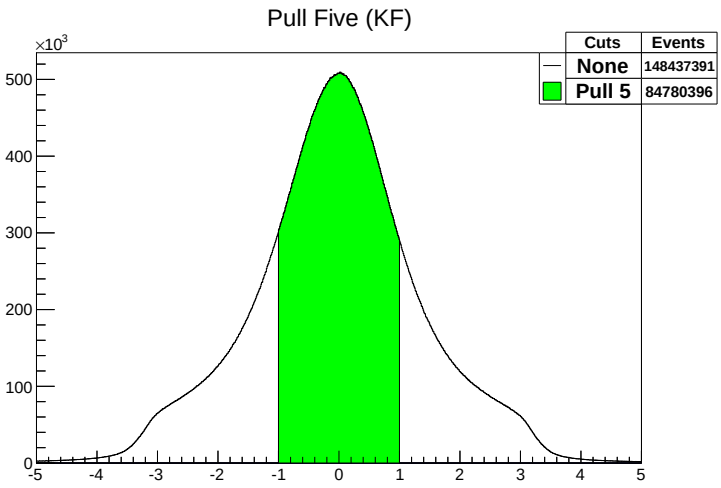
Pull Five (KF)
×10^3
Cuts
Events
None
148437391
Pull 5
84780396
500
400
300
200
100
0
-5
-4
-3
-2
-1
0
1
2
3
4
5

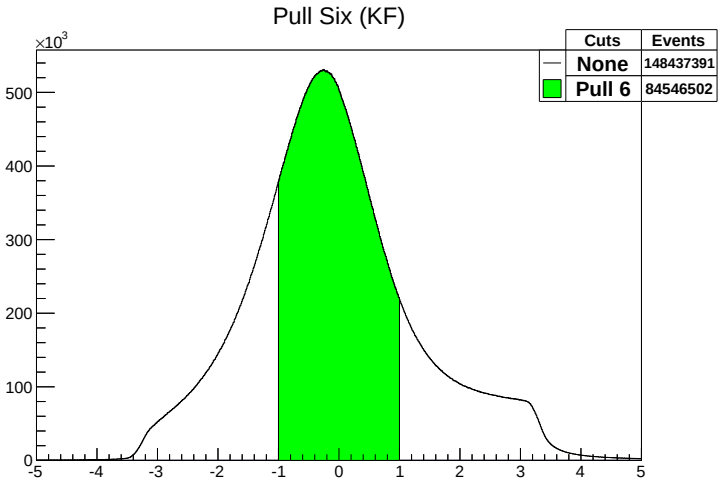
Pull Six (KF)
×10^3
Cuts
Events
None
148437391
Pull 6
84546502
500
400
300
200
100
0
-5
-4
-3
-2
-1
0
1
2
3
4
5

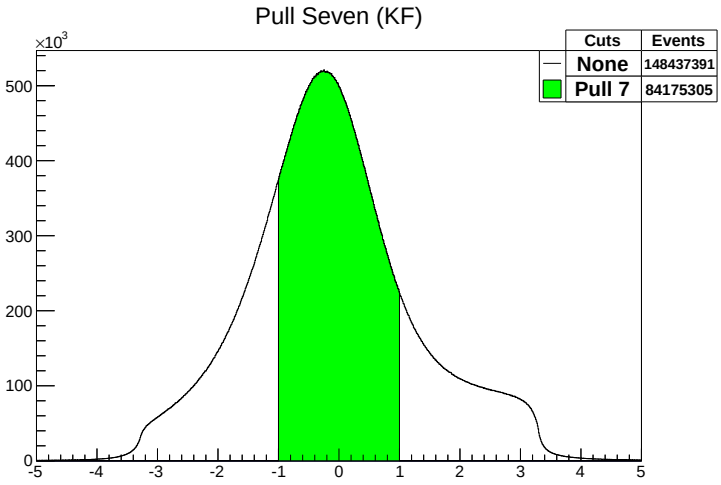
Pull Seven (KF)
×10^3
Cuts
Events
None
148437391
Pull 7
84175305
500
400
300
200
100
0
-5
-4
-3
-2
-1
0
1
2
3
4
5

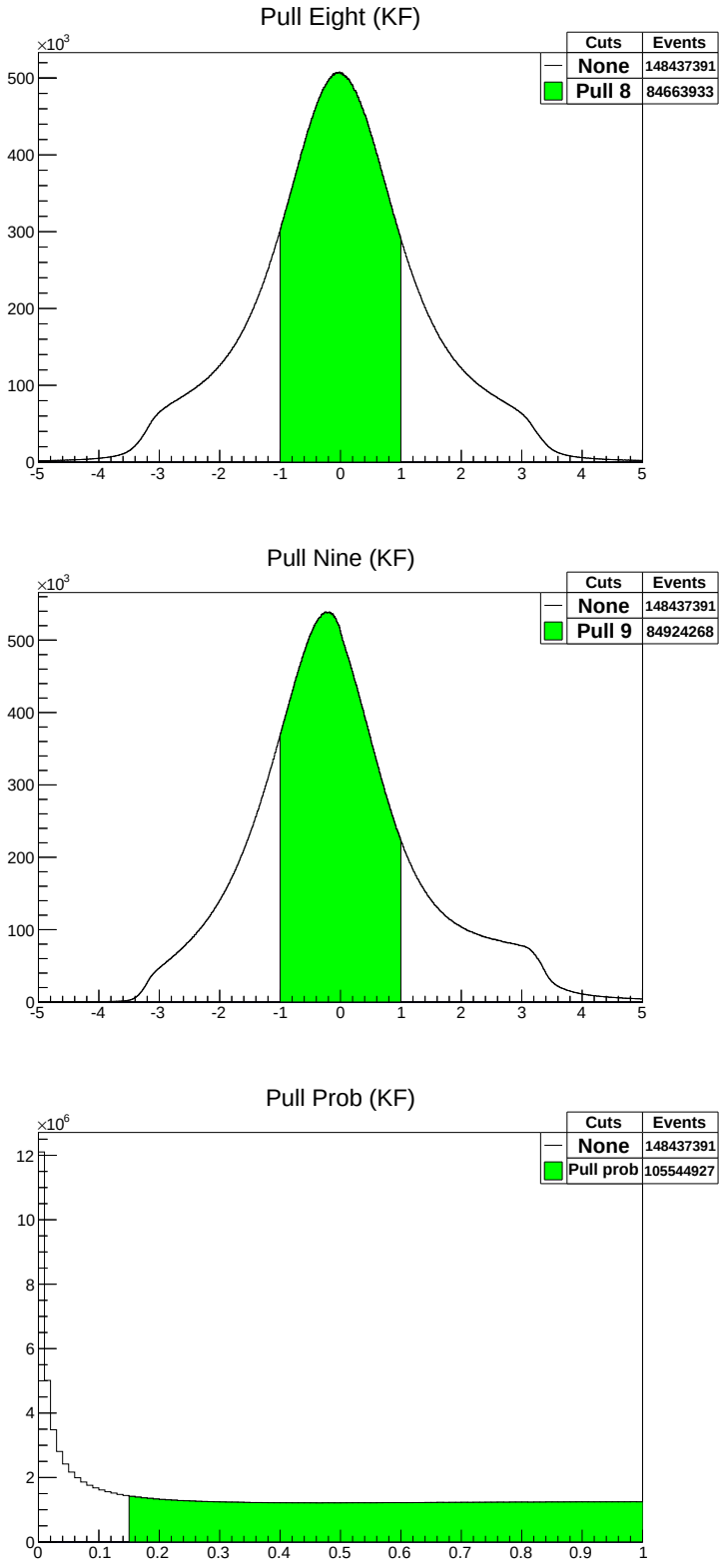

Figure 40: Pull distributions. The pull cuts from equation 3.21 are represented.

These cuts should be done right after the kinematic fit, but the ω mass cut rejects a much larger amount of data, which means that if we wanted to plot all the cuts

together (as we will do at the end) in that case, the effects of the rest of the cuts will appear largely suppressed, difficulting their visualization on the plot.

3.4.4 t' Distribution Cut

As discussed before, we will apply a cut on the t' distribution such that

$$-3.5\,GeV^2 < t' < -0.6\,GeV^2 \tag{3.22}$$

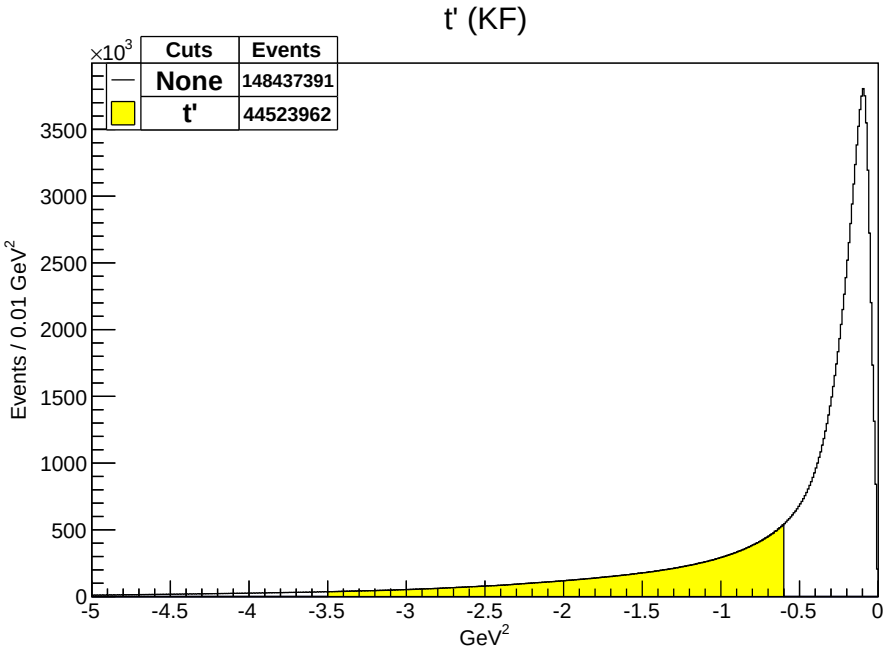

Figure 41: t' Distribution. The t' cut is represented.

The reason that these particular values of the cut were chosen is that, apart from what has been already said about low and high $|t'|$ values, we want to select the region that behaves like an exponential, as expected from previous analysis, and also from Regge theory [32]. The application of the other cuts will move the maximum of the distribution much closer to the selected data, as we will show later, which will justify why this cut was performed in this way.

3.4.5 Fiducial and TOF Knockout Cuts

The geometric fiducial cuts consist in discarding events laying inside regions that can not be reliably reproduced in the simulation, like the ones near the torus coils, where the magnetic field varies rapidly. This happens between each sector. We

define these regions by constraining the difference in azimuthal angle between the center of a given sector and a particle track. The fiducial boundaries on the angle ϕ were evaluated separately in each sector, and are defined as the ϕ values where occupancy gets lower than 50% respect with each sector flat region, which are defined as -10° $< \phi <$ 10° [33].

We also need to see if there are time of flight paddles that we must get rid of. The difference between the measured and expected TOF was plotted for every paddle and for each of the particles in the final state and then fitted to a Gaussian. The standard deviation of the fit is defined as the resolution of that paddle, which is plotted to obtain the bad resolution ones. The knocked out paddles are then identified by their discrepancies in occupancy between data and simulations.

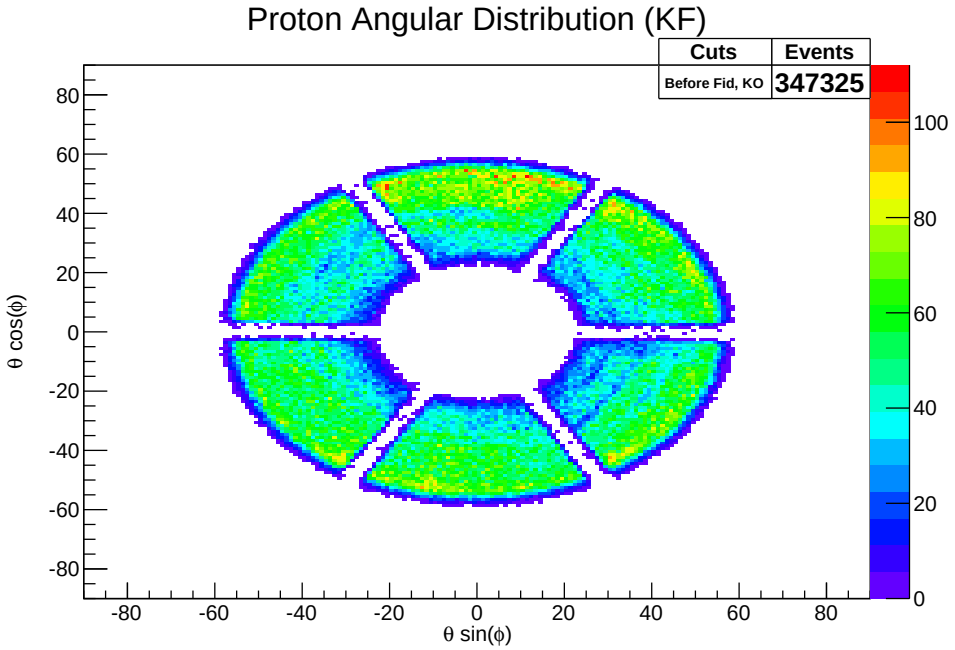

Figure 42: Angular distribution of the proton after the cuts described in the previous sections.

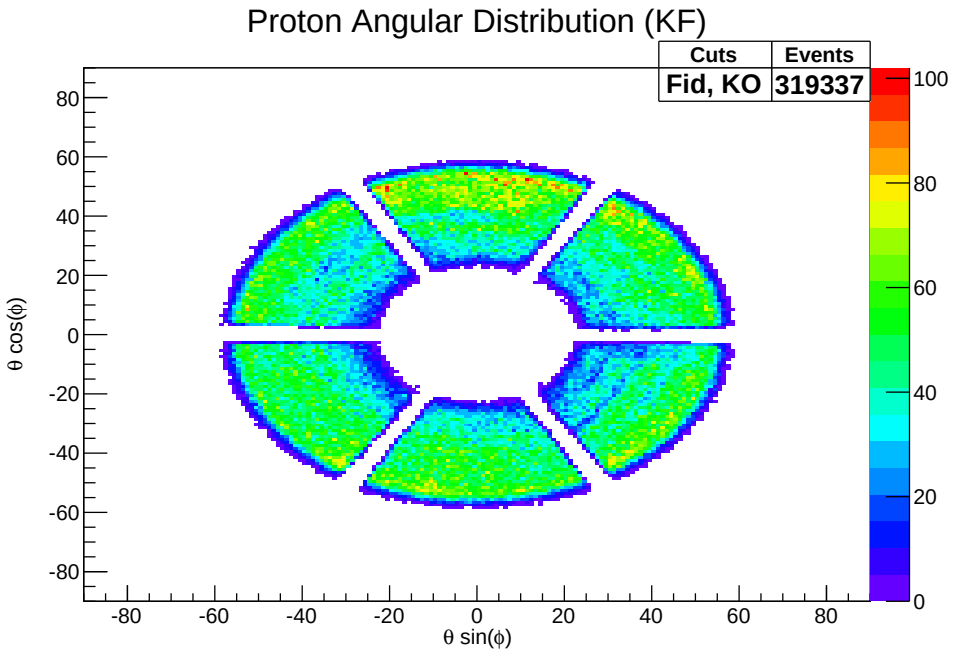

Figure 43: Angular distribution of the proton after the fiducial and TOF knockout cut are added to the cuts.

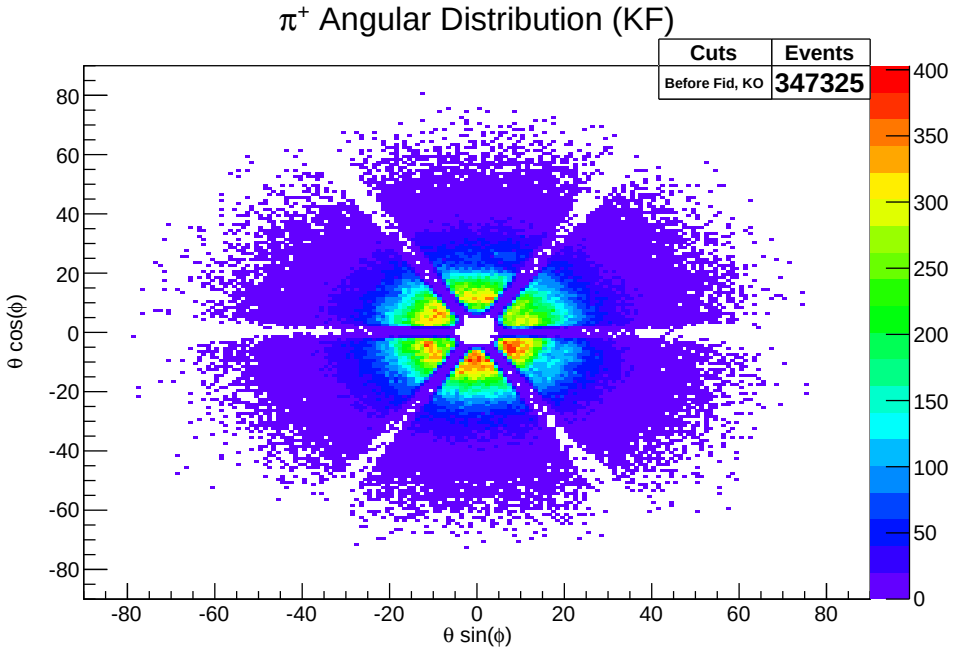

Figure 44: Angular distribution of the π^+ after the cuts described in the previous sections.

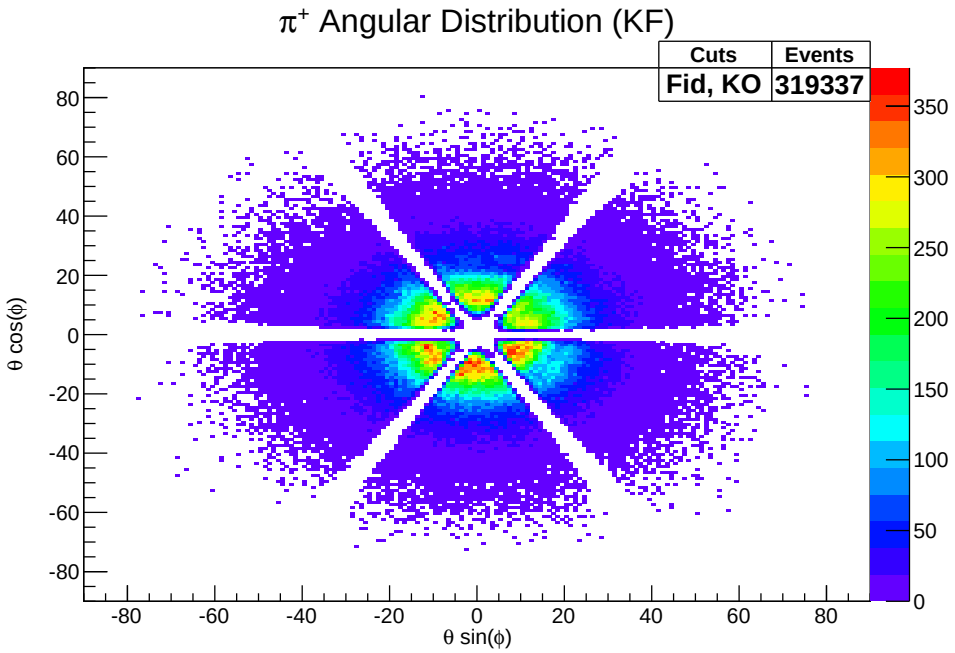

Figure 45: Angular distribution of the π^+ after the fiducial and TOF knockout cut are added to the cuts.

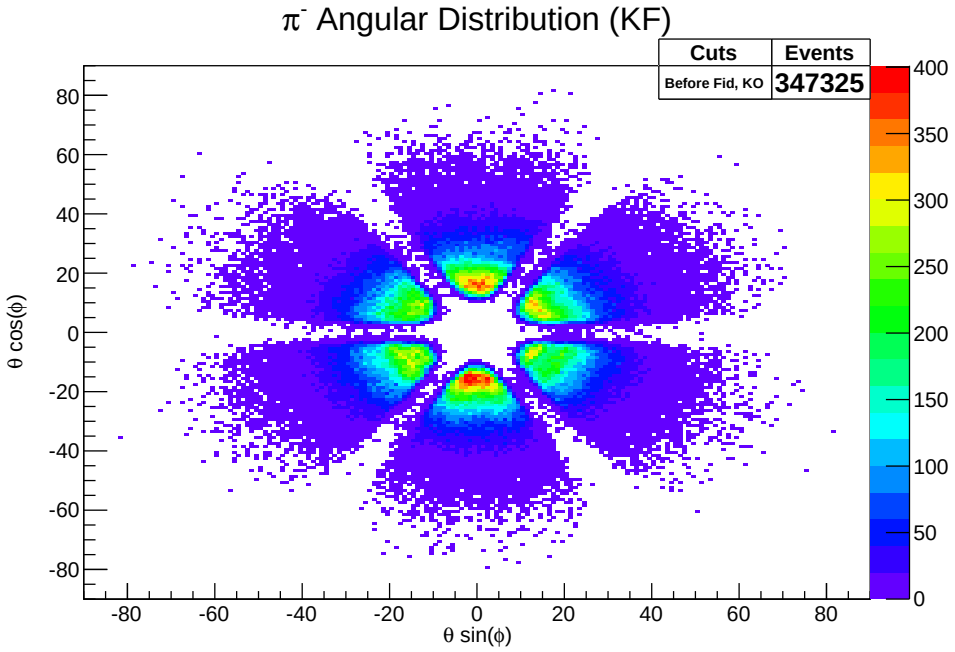

Figure 46: Angular distribution of the π^- after the cuts described in the previous sections.

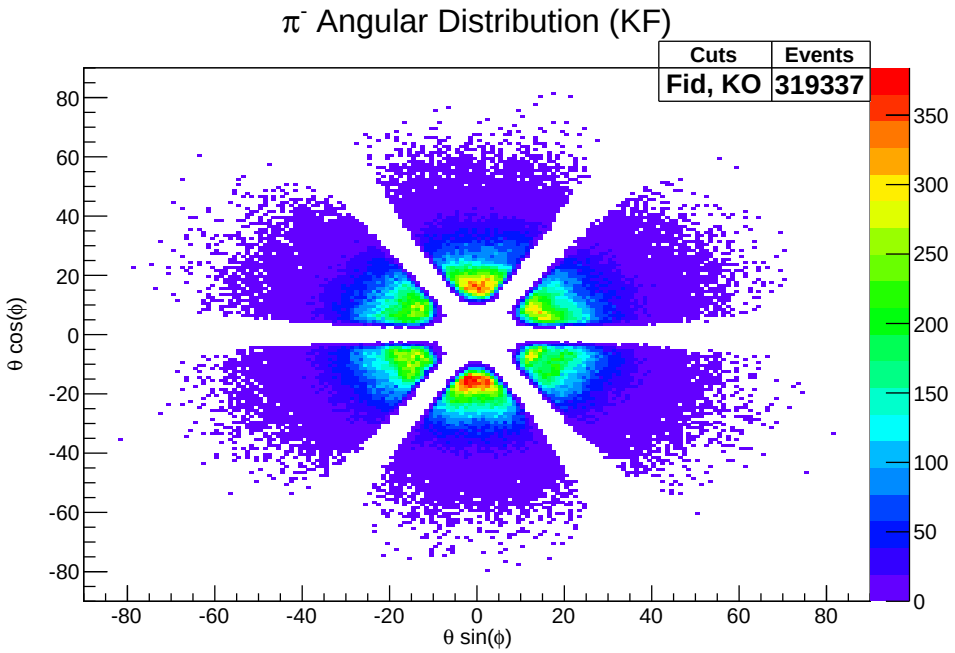

Figure 47: Angular distribution of the π^- after the fiducial and TOF knockout cut are added to the cuts.

From figures 42 to 47 we can see how the zones between the 6 sectors of CLAS and the forward hole are cleared from data, since those are low acceptance region. Also, we see that the pions scatter forward while the protons scattering is wider, as expected from a diffractive event.

3.5 Signal-Background Separation

3.5.1 Side-Band Subtraction Method

The most common approach when it comes to separate background events from the signal ones is to use the side-band subtraction method. This method consist in performing a fit of the data by a sum of two different functions, one corresponding to the signal and the other to the background. Then we can calculate the signal area to the signal plus background (total) area relation, which would gives us the probability that any event comes from the signal.

We will also mention that the fits were performed using the MINUIT numerical minimization computer program, which searches for minima with respect to one or more parameters using several different methods. It is also used in the PyPWA package to minimize $-\ln \mathscr{L}$ and in the kinematic fit to minimize χ^2 [34].

As an example of this we show in figure 48 the mentioned method applied to our kinematic fitted data after the cuts we described must be applied to it are done. Here a third order polynomial was used to fit the background and a Voigtian to fit the signal (considering the reasons given in section 1.4).

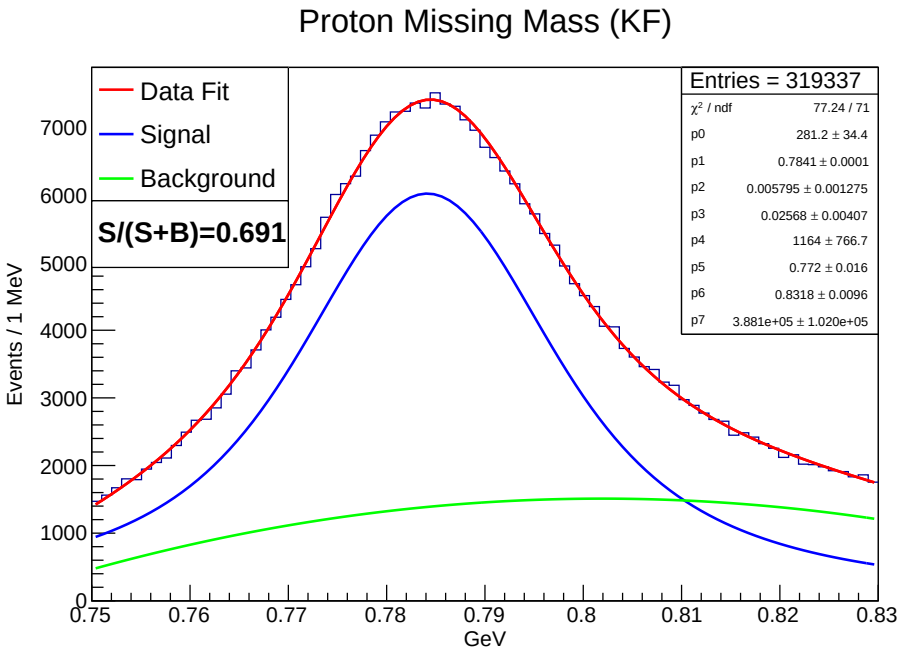

Figure 48: Data fit using a Voigtian with $\mu = p1$, $\sigma = p2$ and $\Gamma = p3$ (see section 3.5.2) multiplied by a factor $p0$, and a polynomial of the form $y = p4 + (x - p5)(x - p6)(x - p7)$.

However, it would be preferable to avoid this method in our analysis because we are dealing with a multi-dimensional problem, and also it would be desirable if we could have a signal probability for each event instead of a global probability.

3.5.2 Quality Factor Calculation Method

We decided to perform the signal-background separation using the same method used in [35], since it is more appropriate according to our multi-dimensional conditions and it is better since it assigns to each particular event a quality factor, Q_i, that gives us the probability a particular event belongs to the signal.

Any three body decay event can be described by five independent kinematic variables. One was chosen to be the invariant mass of the 3π system, $m_{3\pi}$. For the others, we chose to use the set $\cos\theta_{\omega}^{CM}$, $\cos\theta^{GJ}$, ϕ^{GJ} and λ, where the first variable is the cosine of the ω production angle in the center of mass frame, the second

one is the cosine of the decay polar angle in the Gottfried-Jackson frame (see Appendix B), the third one is the decay azimuthal angle in the Gottfried-Jackson frame, and the last one is a quantity proportional to $|\vec{p}_{\pi^+} \times \vec{p}_{\pi^-}|^2$, where $\vec{p}_{\pi^+}$ and $\vec{p}_{\pi^-}$ are measured also in the Gottfried-Jackson frame.

Each event will then be determined by $m_{3\pi\, i}$ (which we will leave as our variable as we have an idea of how it is distributed, as explained below) and a quantity $\vec{\xi}_i = (\cos\theta^{CM}_{\omega\, i}, \cos\theta^{GJ}_i, \phi^{GJ}_i, \lambda_i)$. This quantity belongs to a space in which we are going to define the metric δ_{ij}/σ_i^2 (this, of course, represents a 4x4 diagonal matrix), with $\vec{\sigma} = (\sigma_k) = (2, 2, 2\pi, 1)$ where each σ_k is the root mean square (RMS) of the k^{th} variable, this with the purpose of giving equal weight to each one [36].

Then we can define the distance between two events as

$$d_{ij} = \sum_{k=1}^{4} \left(\frac{\xi_{ik} - \xi_{jk}}{\sigma_k} \right)^2 \tag{3.23}$$

We know that our data is made up of background and signal events. The background distribution will be given by a function $B(m_{3\pi}, \vec{\xi})$, which in principle is unknown, while the signal distribution will be given by a kinematic dependence multiplied by a Voigtian function, taking then the form

$$S(m_{3\pi}, \vec{\xi}) = F_s(\vec{\xi}) V(m_{3\pi}, \mu, \sigma, \Gamma) \tag{3.24}$$

The kinematic dependence is unknown, and the Voigtian is the convolution of a Gaussian of width σ and a Lorentzian of width Γ, both with mean μ.

The next step consists in finding, according to our defined distance, the closest events to each and every event. For each event (i) we chose to find the closest 100 events (j), including the event itself. This number is arbitrary but we are trying to keep the neighborhood we are going to consider as small as possible, and at the same time intending to have enough data for our calculations. Since each selected event will have its own kinematic variables $\vec{\xi}_i$ and $m_{3\pi\, i}$, we can approximate to $\vec{\xi}_i$ the values $\vec{\xi}_j$ of each of the 100 events inside the neighborhood considered around them, and also in this conditions we can approximate the background to a linear function, therefore we have

$$S(m_{3\pi\, j}, \vec{\xi}_j) \approx F_s(\vec{\xi}_i) V(m_{3\pi\, j}, \mu_i, \sigma_i, \Gamma_i) = A_i \cdot V(m_{3\pi\, j}, \mu_i, \sigma_i, \Gamma_i) \tag{3.25}$$

$$B(m_{3\pi\,j}, \vec{\xi_j}) \approx B(m_{3\pi\,j}, \vec{\xi_i}) \approx a_i m_{3\pi\,j} + b_i \tag{3.26}$$

We will determine the parameters A_i, a_i and b_i for each event by fitting to the events inside the neighborhood already defined. From the fit we will obtain the functions $S(m_{3\pi\,j})$ and $B(m_{3\pi\,j})$, and then we can calculate the expected number of signal and background events as $S_i = S(m_{3\pi\,i})$ and $B_i = B(m_{3\pi\,i})$, from which we can calculate the event signal probability (called quality factor or Q-factor)

$$Q_i = \frac{S_i}{S_i + B_i} \tag{3.27}$$

As an example, figures 49, 50 and 51 show the fits described before performed on three different events (namely, the 8th, 36th and 152nd ones), with their respective Q-factor values. The data fit was done using a Voigtian with $\mu = p1$, $\sigma = p2$ and $\Gamma = p3$ multiplied by a factor $p0$, and a polynomial of the form $y = p4 + p5(x - 0.75)$.

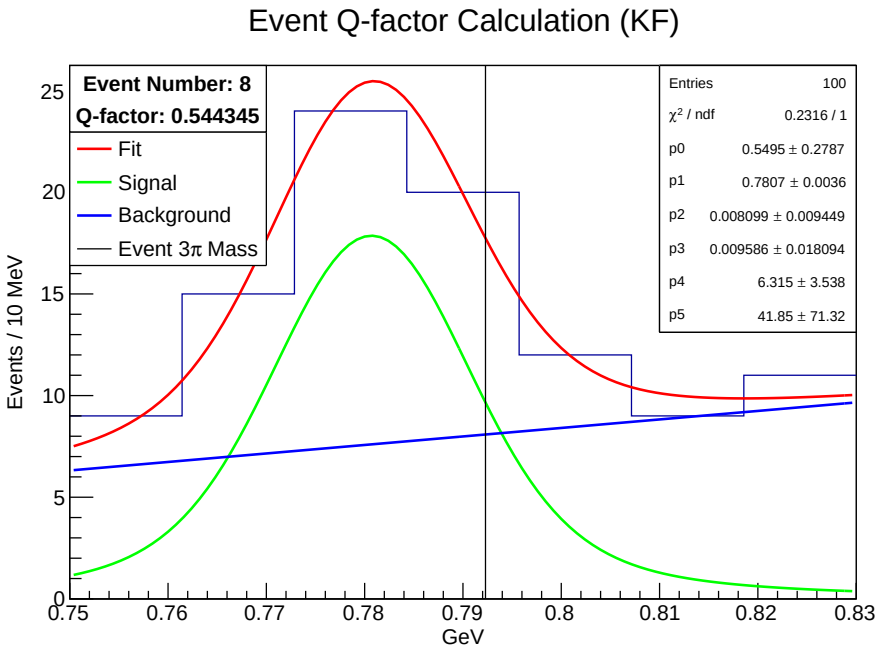

Figure 49: Fit and Q-factor determination for event 8.

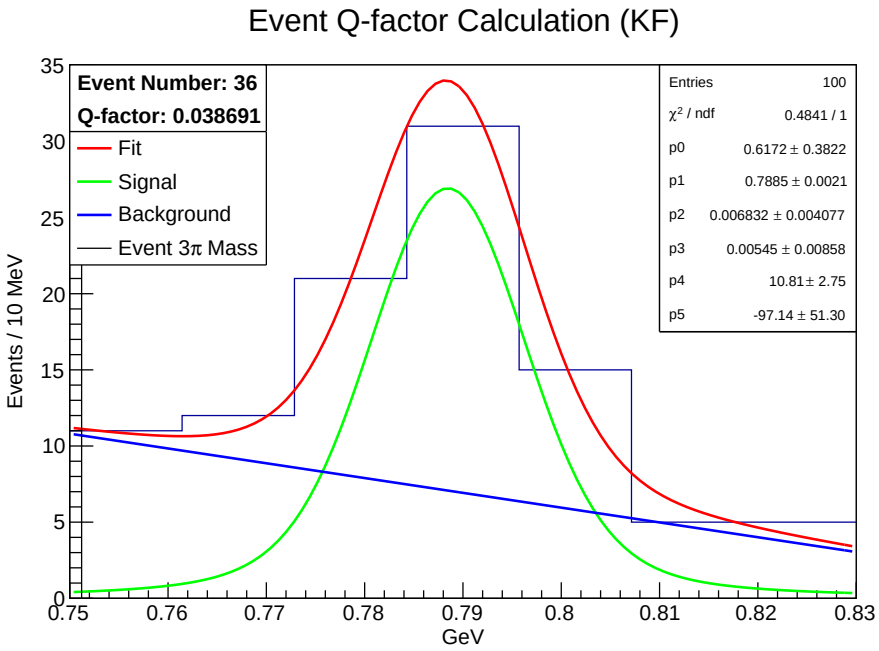

Figure 50: Fit and Q-factor determination for event 36.

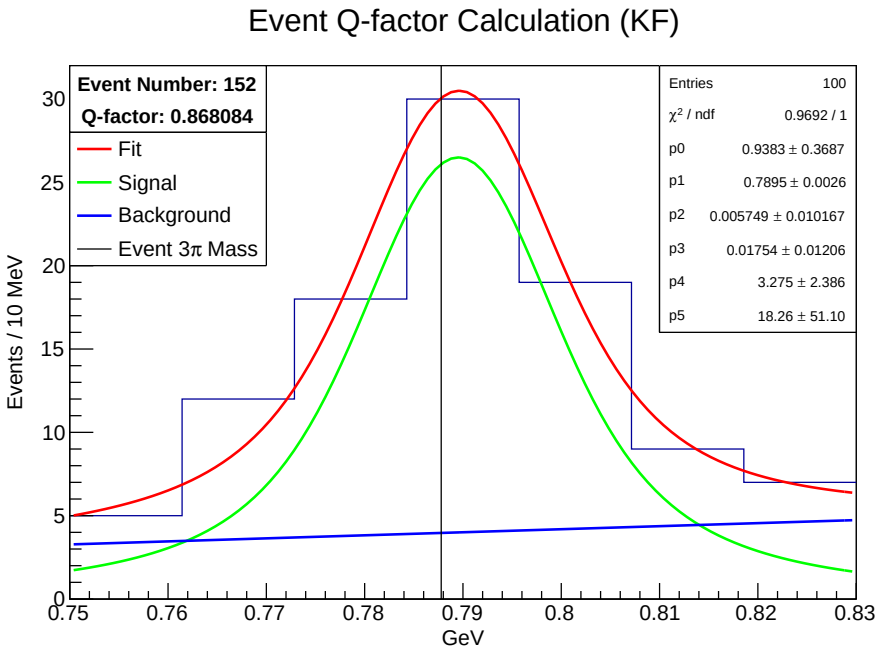

Figure 51: Fit and Q-factor determination for event 152.

In figure 52 we plot the Q-factors obtained for all events (although some were discarded if the fit was unsuccessful), where a concentration at relatively high signal probabilities can be seen, something we would expect. We will accept events as signal ones if their probability of being so is higher than 70%, in other words, we will impose the Q-factor cut

$$Q > 0.7 \tag{3.28}$$

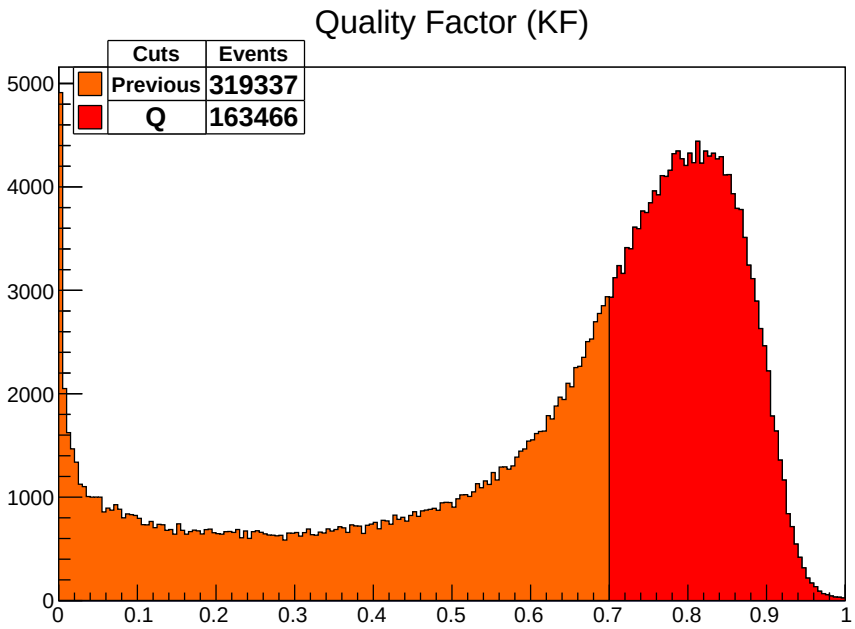

Figure 52: Quality factor of all events. The Q-factor cut, from equation 3.28, is represented.

Taking this into account the 152nd event would make it through the cut, which means that it is probably a signal event, while the 8th and 36th ones would not comply with the condition and therefore will be discarded from our analysis, since probably they are part of the background.

Finally, we also are going to weight the data by the Q-factor to give more importance to the events that more probably belongs to the signal, although the results of doing this or not proved to be almost indistinguishable.

3.6 Selected Data

Now we will plot some of the important quantities already seen since we have already described all the cuts that will be performed on our kinematic fitted data, which allows us to apply them sequentially on the same plot.

3.6.1 Energy Spectrum

We start by plotting the photon beam energy.

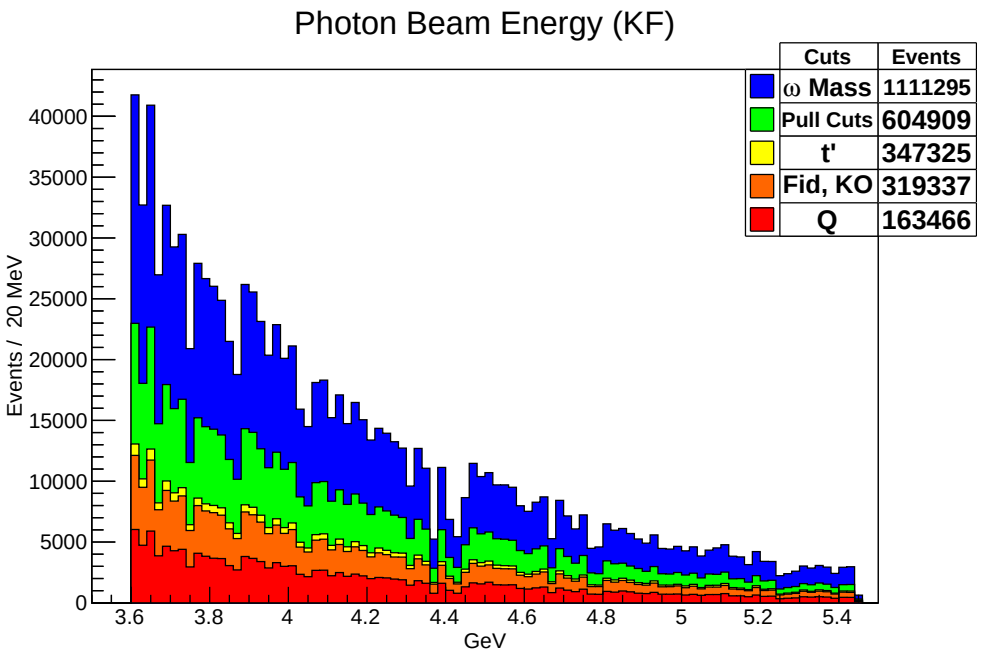

Figure 53: Energy spectrum through the various cuts described.

In figure 53 we can see the cumulative effects all the cuts that we described in the previous section have on our kinematically fitted data. Also, as we mentioned before, the plot where the Q-factor cut is applied is also weighted by Q. In this figure we can see the bremsstrahlung profile that will be put as input in the Monte Carlo simulation.

3.6.2 t' Distribution

Then we show the t' distribution. The region in which we plot now is wider than before, down to -8 GeV^2 instead of -5 GeV^2 since the amount of data left out before was insignificant in relation to the total data plotted, and now it is not.

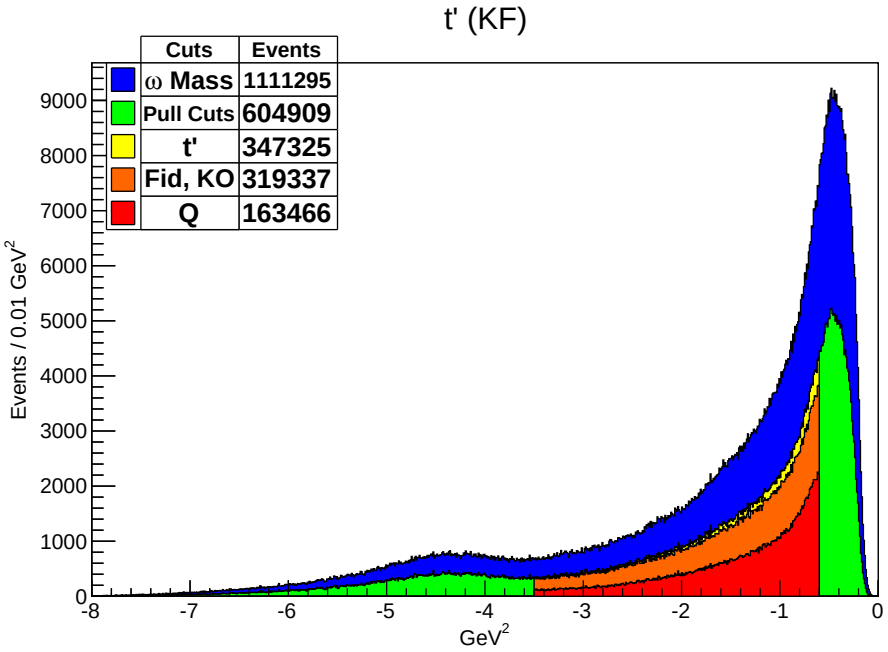

Figure 54: t' distribution through the various cuts described.

We can see from figure 54 that the reason behind the values chosen in the t' cut was to select the data in the exponential region. This region could have gone up to -0.5 GeV, the reason is not so is that this was not evident during the process of deciding the cuts because some plots were made with lower resolution in an effort to diminish execution time, added to the fact that the shape of this plot slightly changed were the cuts other than the t' one were being adjusted.

3.6.3 Proton Missing Mass

Now we plot the missing mass of the proton, or, after all the cuts, the ω mass.

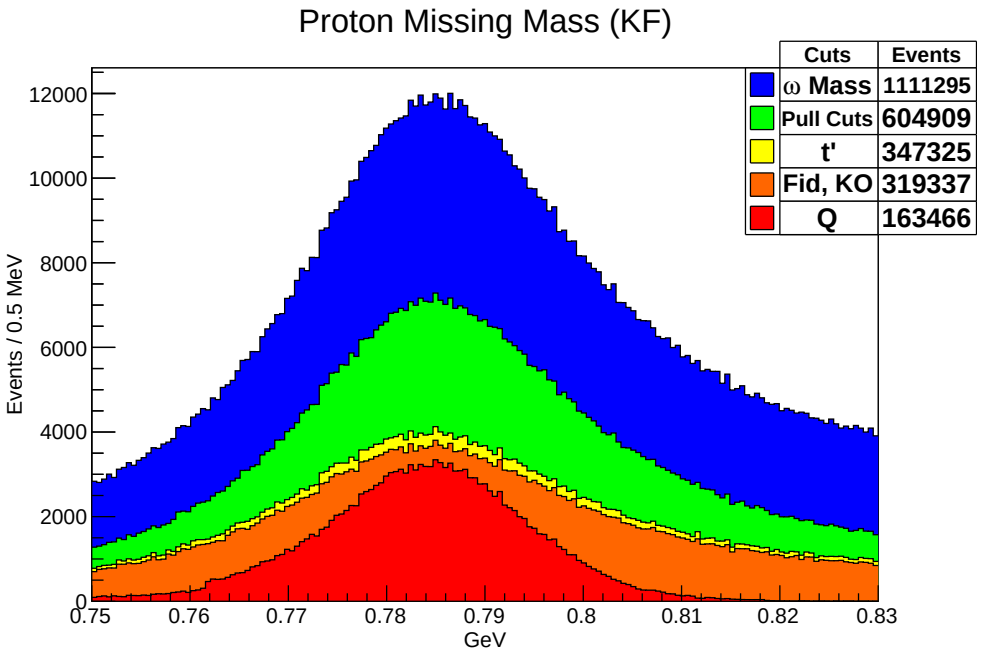

Figure 55: Proton missing mass through the various cuts described.

From figure 55 is also clear now that the mass interval chosen in the ω mass cut contained the signal we want to study, and some of the background.

3.6.4 Other Mass Spectrums

We also present the plots of some mass and missing mass systems previously shown to show that the barion channels (and their complementary di-pion channels) are not present anymore.

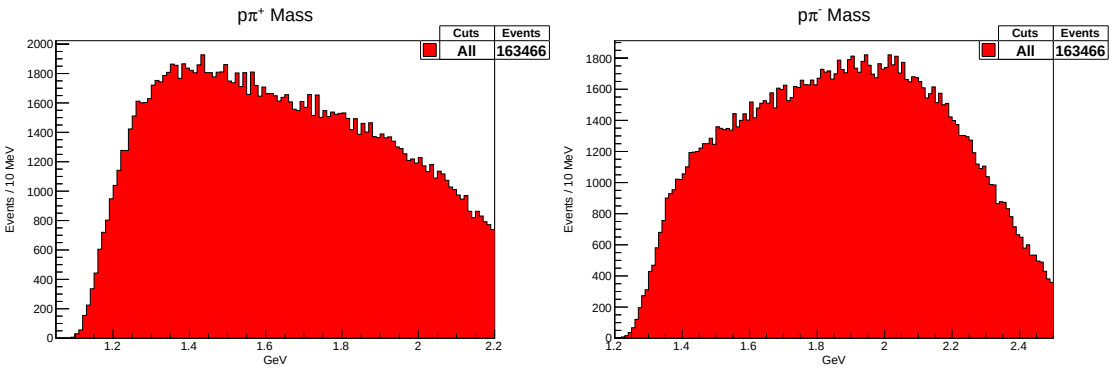

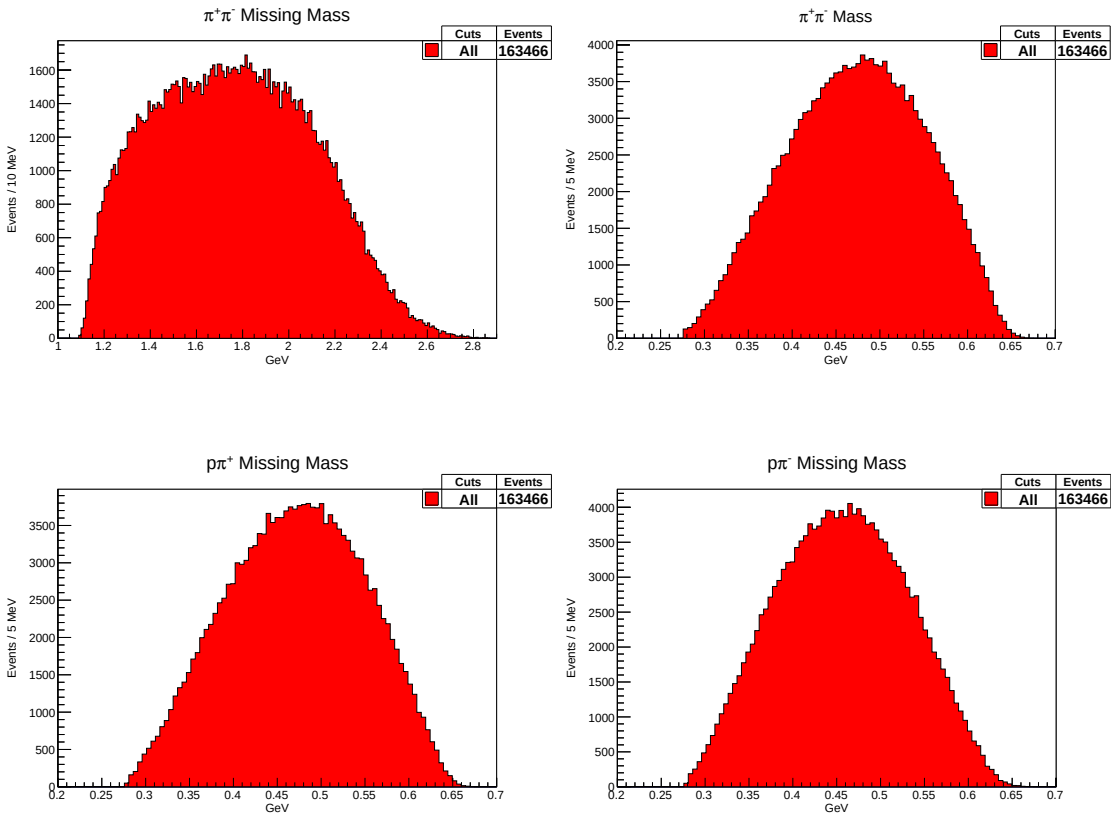

Figure 56: Baryon channels (first 3 plots) and di-pion channels (last 3 plots).

4 Monte Carlo Simulation

In this chapter we describe how our data was corrected by the acceptance of the detector using a Monte Carlo simulated phase space of the required particles of our analysis in conjunction with programs that simulate the detector in order to reproduce what a perfect detector (without holes for example) would have measured. These programs can be obtained from the standard repository for CLAS.

4.1 Event Generation

In order to generate Monte Carlo events, in this experiment we used a phase space event generator called ppgen. We generated events between the energy range from 3.6 to 5.3 GeV with the expected bremsstrahlung profile [37], and imposed a t distribution of the form e^{-3t}. As mentioned before, this exponential form is expected from Regge theory, and the particular value of the slope comes from various previous analysis, although the ideal case would have been to fit e^{-bt} to our data and obtain it from it. This generates a gamp file which will converted to a part file and in the process the target distribution is smeared in order to emulate the physical extension of it.

To simulate the detector we first use the geant3 based program gsim, which gives us an output in BOS banks format. This simulation treat the detector like if it were an ideal one, therefore we need to further manipulate our files in order to make them look more like real data. This is done using the program gpp (gsim post-processor), which removes DC dead wires and SC dead paddles, smears the DOCA and SC TDCL and TDCR (left and right time to digital converters) values, uses a DC drift velocity of 50 microns per nanosecond and in order to mimic the detector resolution it matches the tracking resolution of the simulated data to that of the real events in the three drift chamber regions.

The final step is then to run the event reconstruction program a1c, which, analogously to the experimental data processing case, will reconstruct the simulated event from the simulated electronic signals of the detector which were obtained as we just have described in the previous paragraphs, giving us the desired physical quantities for our analysis.

4.2 Simulation Selection

The Monte Carlo Simulation was then skimmed and kinematically fitted in the same manner as with the experimental data. The next step consisted in selecting the simulated events that pass the same cuts (except the Q-factor one since the simulation does not have background) that our experimental data did. The result is known as the Accepted Monte Carlo. We will proceed to show how each cut, that have been already explained, affected some quantities, and in some cases the selected data is also plotted (after being rescaled to have equal area as the Accepted Monte Carlo plot for comparison).

4.2.1 Energy Spectrum

We begin with the simulated photon beam energy, over which it is imposed that

$$3.6\,GeV < E_\gamma < 5.3\,GeV \tag{4.1}$$

Figure 57 shows the resulting energy spectrum.

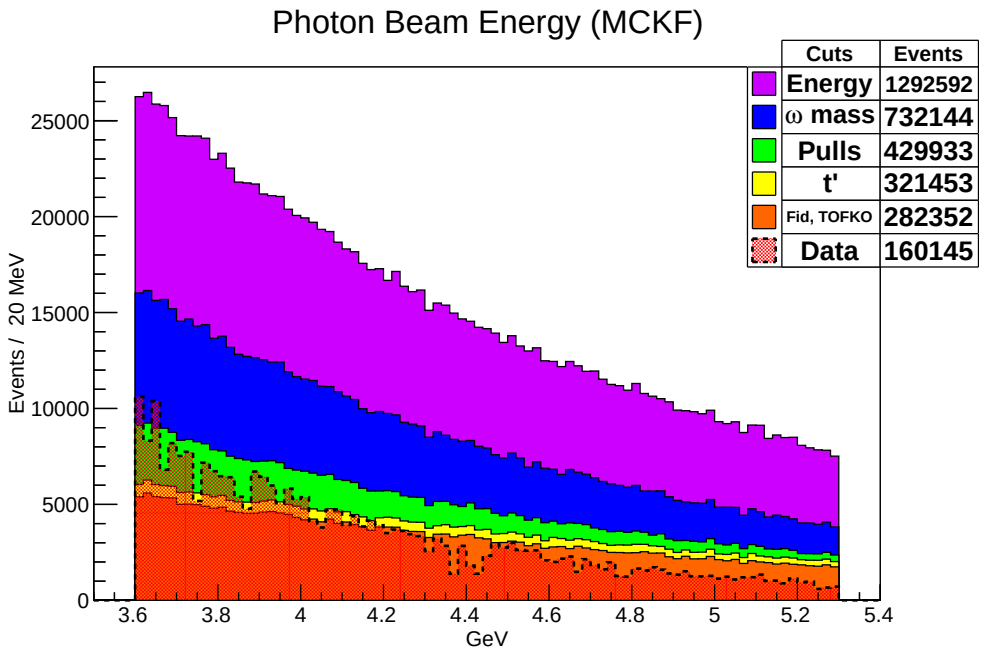

Figure 57: Photon Beam Energy Spectrum for the Monte Carlo simulation, and all the cuts applied to it.

Not only the described cut was represented, but also the rest of the cuts already

explained for the data, which will be exactly the same. We can see that there is a difference between the Accepted Monte Carlo and the selected data slopes. This could be because the value 3 of the t' slope selected for the Monte Carlo was not the most appropriate. We will mention, but not show to avoid repetitive plots, that some of the events from the Monte Carlo were discarded by this cut since the kinematic fit changed their values.

4.2.2 Proton Missing Mass

For the proton missing mass we will focus on the same region as with the data, which contained the ω signal.

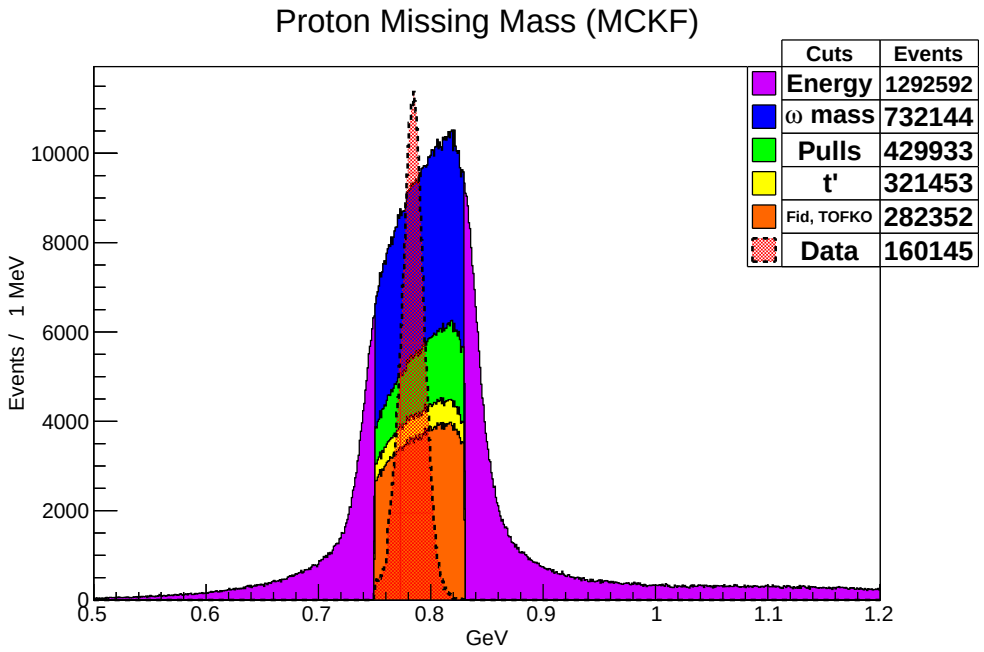

Figure 58: Proton Missing Mass for the Monte Carlo simulation, and all the cuts applied to it.

As expected, there is no resonance in the Monte Carlo simulation in the region where the ω signal appears on the experimental data since it is not simulating any physics, only phase space. What we see in the case of the Monte Carlo simulation would be then just the proton missing mass acceptance of the detector through the various cuts.

4.2.3 t' Distribution

The corresponding cut of the simulated t' distribution will be the same as with the data.

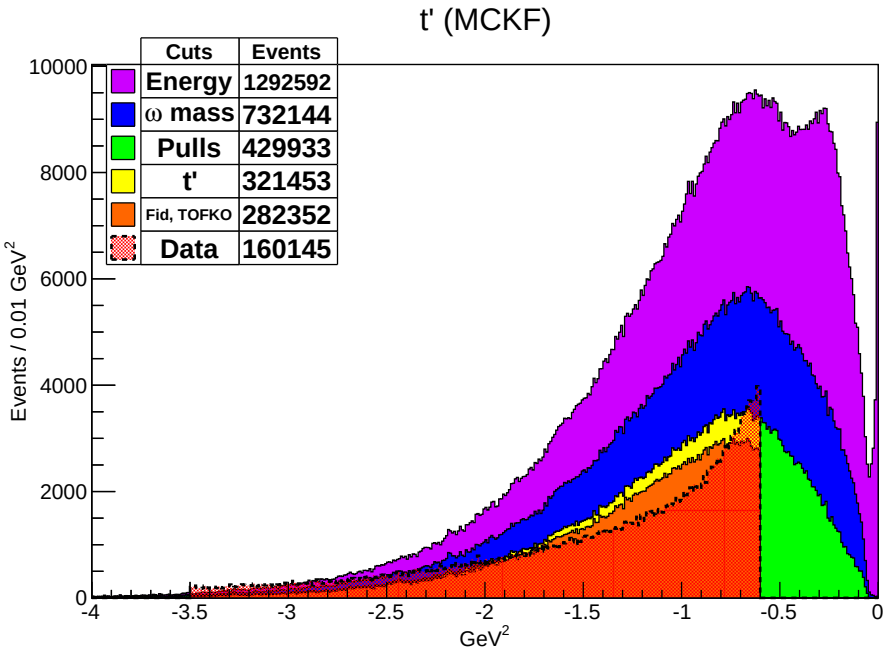

Figure 59: t' Distribution for the Monte Carlo simulation, and all the cuts applied to it.

Again we see a difference in the slopes in both cases, presumably for the reasons already given. The unusual shape of the t' distribution when only the energy cut is applied comes from the fact that events that were not successfully kinematically fitted are still present, at least until we perform the Pull cuts, although in our case the ω mass cut is enough to discard the worst ones. As we mentioned before, this cut should be the first one applied after the kinematic fit, but we did it in this order since otherwise the plots of the following cuts would be greatly suppressed.

4.2.4 Pulls

We want the pulls from the kinematic fit applied to the simulation to verify the same imposed on the data.

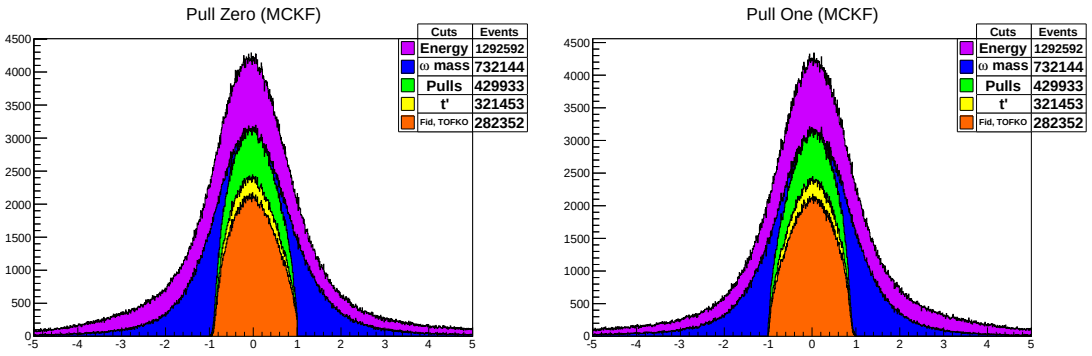
Pull Zero (MCKF)
Cuts Events
Energy 1292592
ω mass 732144
Pulls 429933
t' 321453
Fid, TOFKO 282352

Pull One (MCKF)
Cuts Events
Energy 1292592
ω mass 732144
Pulls 429933
t' 321453
Fid, TOFKO 282352

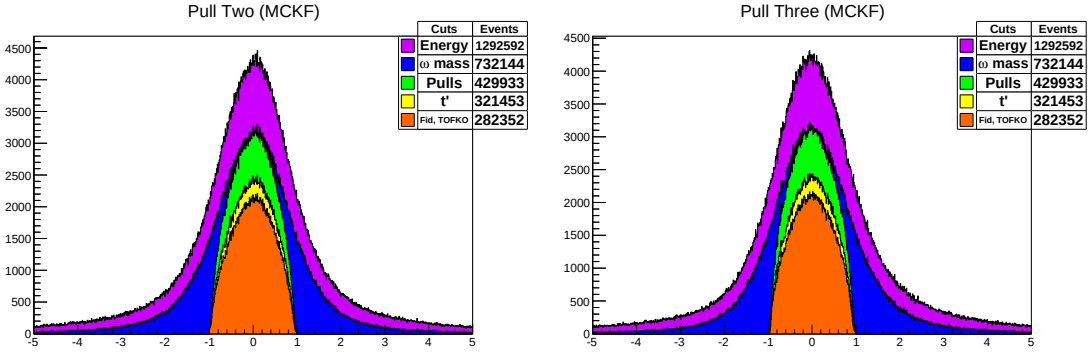
Pull Two (MCKF)
Cuts Events
Energy 1292592
ω mass 732144
Pulls 429933
t' 321453
Fid, TOFKO 282352

Pull Three (MCKF)
Cuts Events
Energy 1292592
ω mass 732144
Pulls 429933
t' 321453
Fid, TOFKO 282352

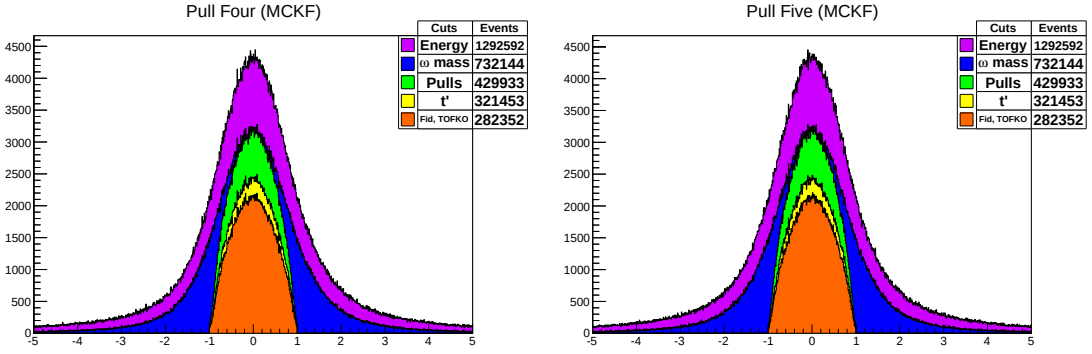
Pull Four (MCKF)
Cuts Events
Energy 1292592
ω mass 732144
Pulls 429933
t' 321453
Fid, TOFKO 282352

Pull Five (MCKF)
Cuts Events
Energy 1292592
ω mass 732144
Pulls 429933
t' 321453
Fid, TOFKO 282352

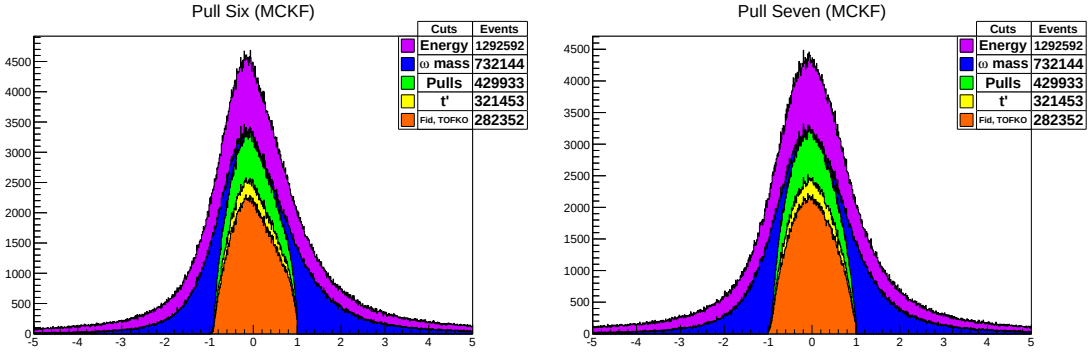
Pull Six (MCKF)
Cuts Events
Energy 1292592
ω mass 732144
Pulls 429933
t' 321453
Fid, TOFKO 282352

Pull Seven (MCKF)
Cuts Events
Energy 1292592
ω mass 732144
Pulls 429933
t' 321453
Fid, TOFKO 282352

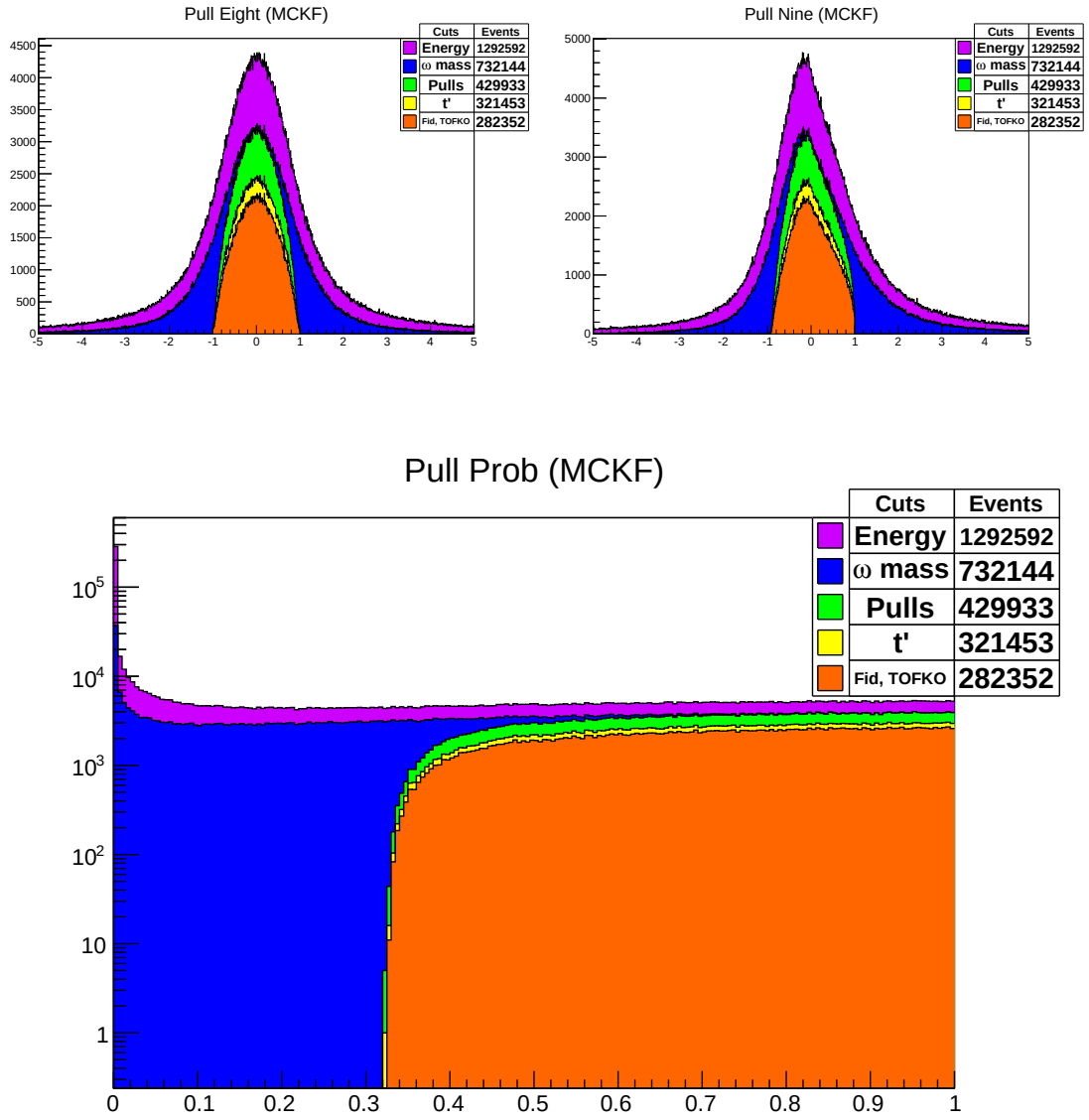

Figure 60: Pull distributions for the Monte Carlo simulation, and all the cuts applied to it. A logarithmic scale had to be used in the Pull Prob.

4.2.5 Fiducial and TOF Knockout Cuts

Finally, the fiducial and TOF knockout cuts performed on the simulation were also the same as the ones performed on the data

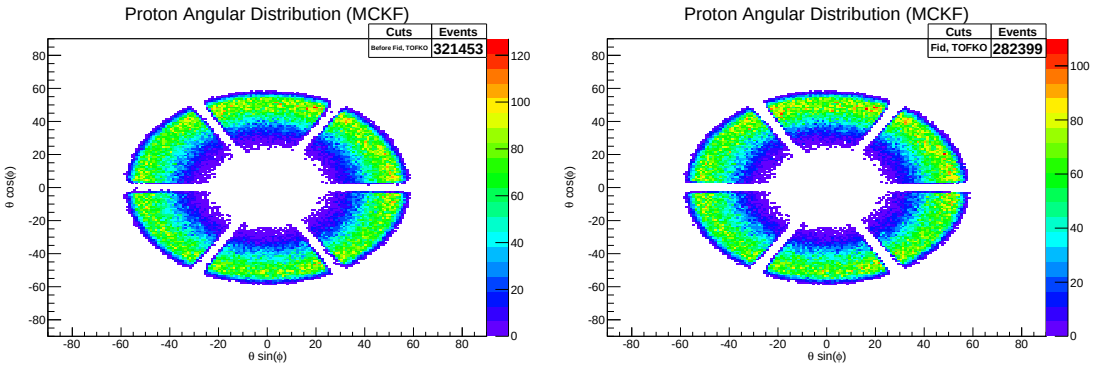

Figure 61: Angular distribution of the proton Monte Carlo simulation, on the left after the cuts previously described, and on the right the fiducial and TOF knockout cuts are added to them.

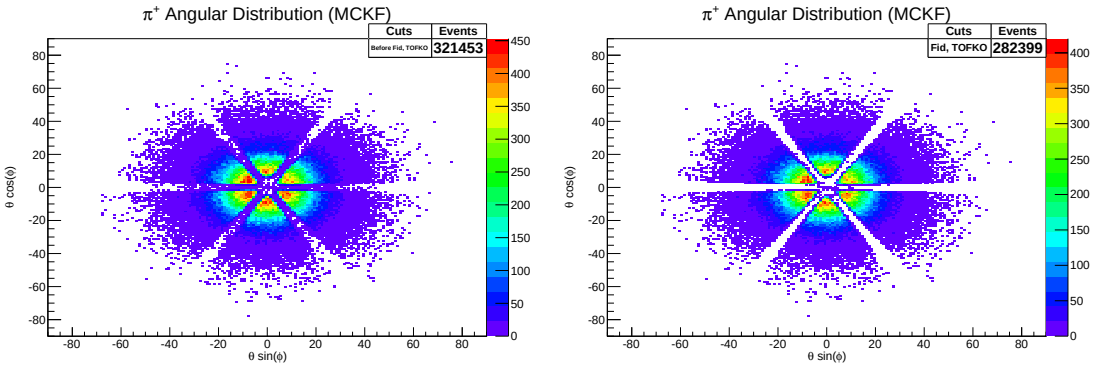

Figure 62: Angular distribution of the π^+ Monte Carlo simulation, on the left after the cuts previously described, and on the right the fiducial and TOF knockout cuts are added to them.

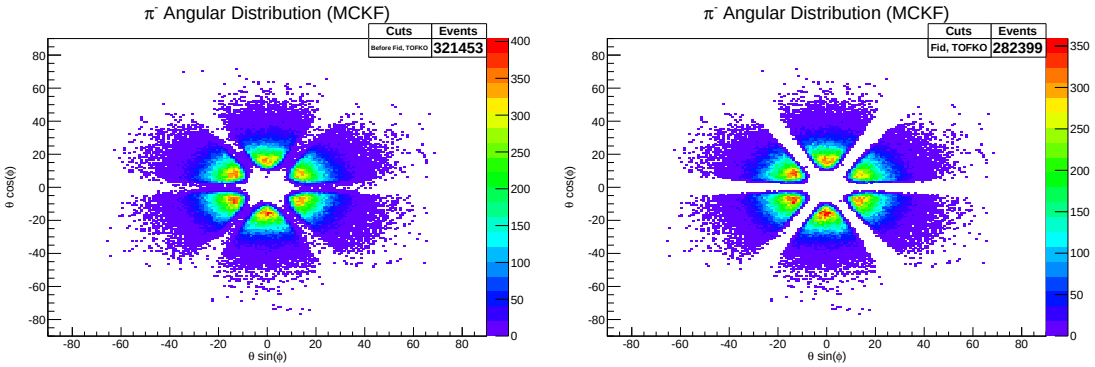

Figure 63: Angular distribution of the π^- Monte Carlo simulation, on the left after the cuts previously described, and on the right the fiducial and TOF knockout cuts are added to them.

We can see that the results are very similar to the data concerning each particle angular distribution and clearance of low acceptance detectors.

4.2.6 Acceptance Correction

As we mentioned at the beginning of this chapter, the Monte Carlo was done with the intention of correcting our data by the acceptance of the detector. As an example, we plot in figure 64 the simulated proton missing mass, which gives us information about how well the apparatus is detecting that signal.

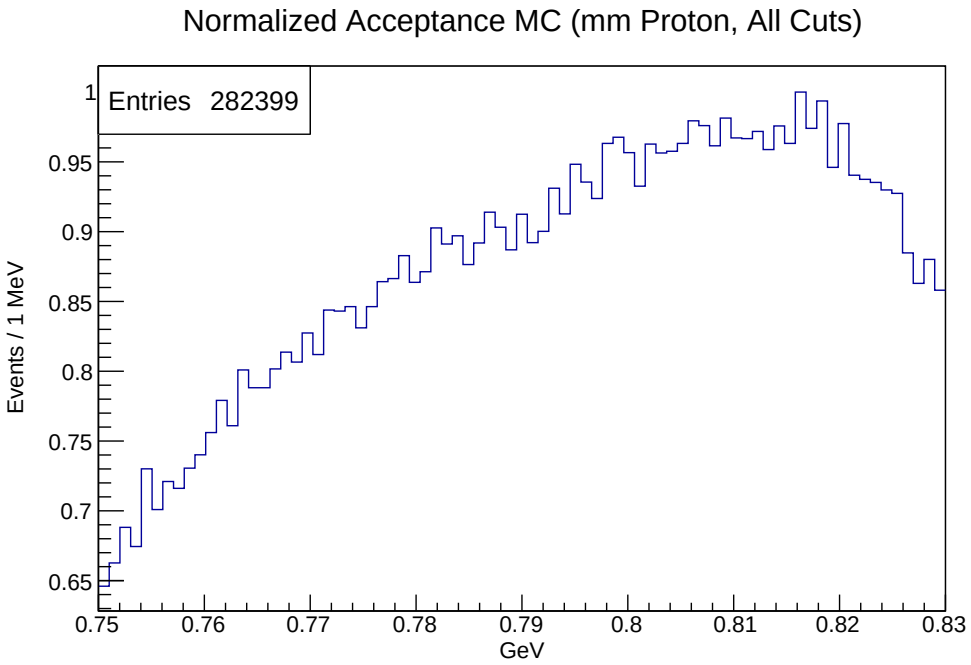

Figure 64: Normalized acceptance.

This distribution will be used to correct by acceptance the proton missing mass (which after all the cuts would be the ω mass) signal by dividing the last by the former, although it can be done to any variable.

5 Model Fitting

To fit our data to the JPAC Decay Model we need to take into account also the photoproduction reaction, which is present in the experiment but not in the decay model. We will use the photoproduction cross section derived in [38]

$$W = \frac{3}{4\pi}\left[\frac{1-A_2}{2} + \frac{3A_2-1}{2}\cos^2\theta - \sqrt{2}A_3\sin(2\theta)cos\phi - A_4\sin^2\theta\cos(2\phi)\right] \tag{5.1}$$

and then we can write the total intensity as

$$I(s,t,u,\theta,\phi,A_1,A_2,A_3,A_4,A_5) = A_1 W(\theta,\phi,A_2,A_3,A_4)P(s,t,u)|F(s,t,u,A_5)|^2 \tag{5.2}$$

where s, t and u are the Mandelstam variables of the decay, θ and ϕ are Adair's angles (see Appendix B) and the A_i's are the parameters to fit. A_5 is the a_0 of the JPAC Decay Model, and it is expected to be positive and independent from the photon energy and from our t' (which is defined from the photoproduction Mandelstam variables), while the parameters A_2, A_3 and A_4, which also must be fitted, are not known at these energies but a lower ones.

Now we can fit our data to the desired model. This could be done by fitting equation 5.2 to the Dalitz plot we can obtain from the data. First we plot the Dalitz from the data, shown in figure 65, which has the shape that corresponds to a P-wave dominated Dalitz, as expected.

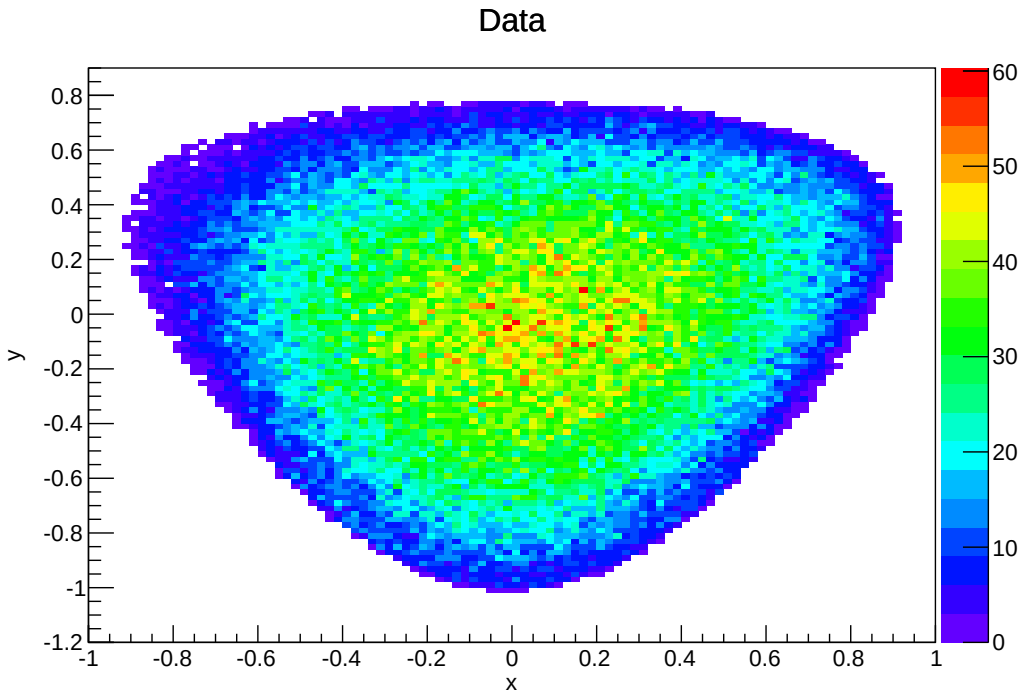

Figure 65: Dalitz for the data.

We also notice that the left superior corner is somewhat depleted. We verify that this is because the acceptance of the detector, shown in figure 66, the main cause behind this being the forward hole it presents.

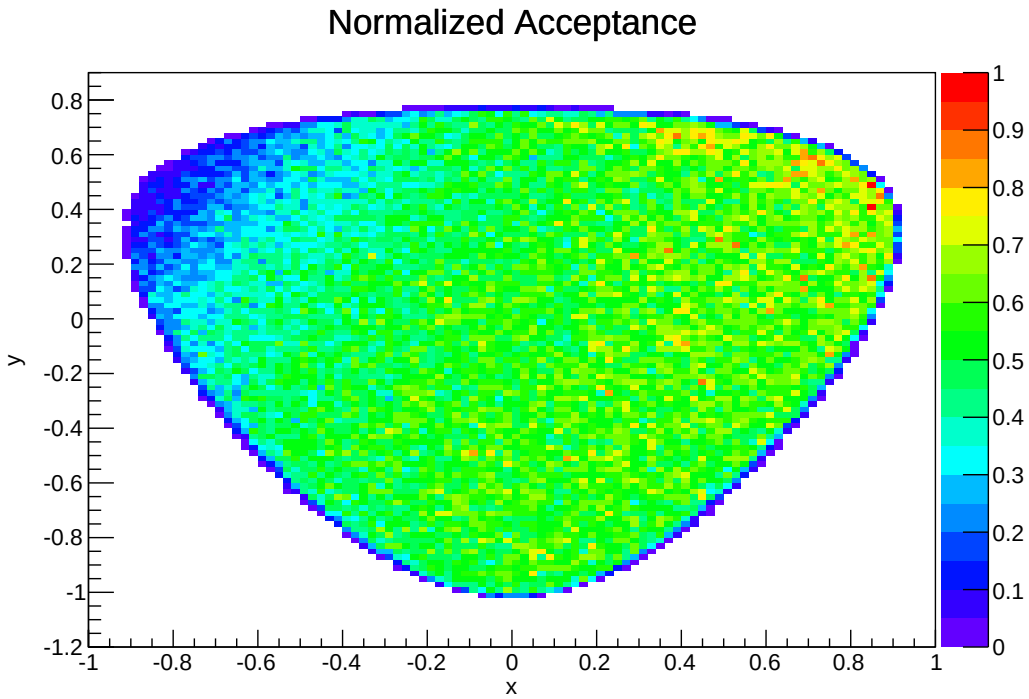

Figure 66: Dalitz for the (normalized) acceptance.

Figure 67 shows the Dalitz plot of the data after the acceptance correction (performed by dividing by it), where the depletion feature does not seem to be present anymore.

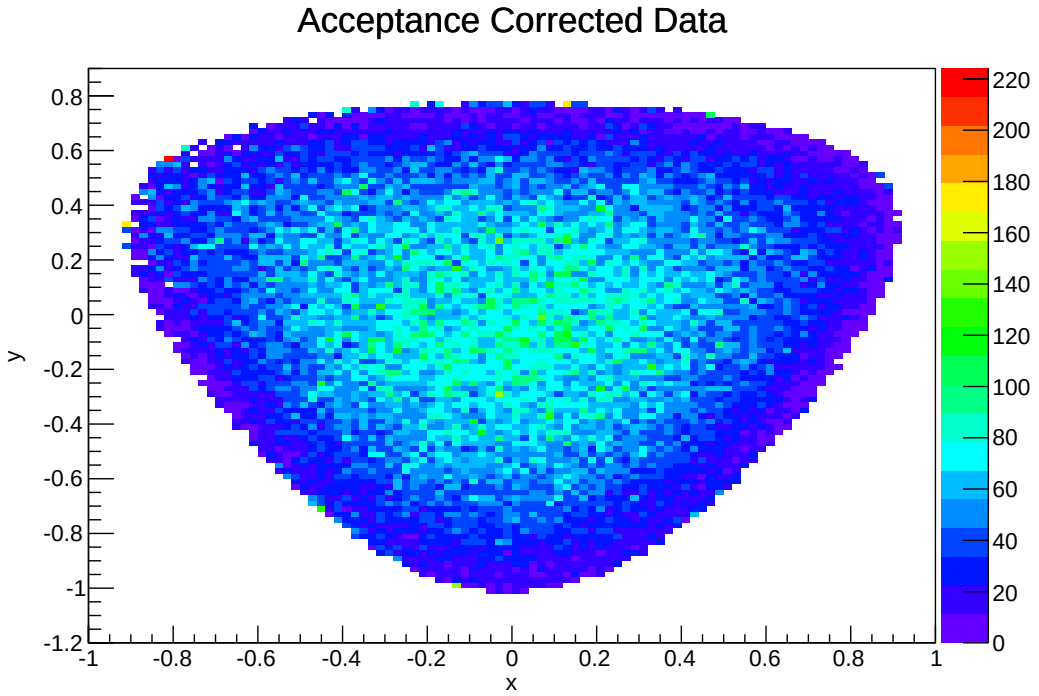

Figure 67: Dalitz for acceptance corrected data.

Finally we will divide the previous plot by P, the result of this is shown in figure 68. Now we have performed over our Dalitz the same operations that were performed over figure 5 (except we will not normalize to 1 at $x = y = 0$). There is a fundamental difference between the numerical result and the one we have obtained from our experimental data, that is that the numerical result was generated considering only the decay at a fixed energy, while in our case we also have a photoproduction at a range of energies.

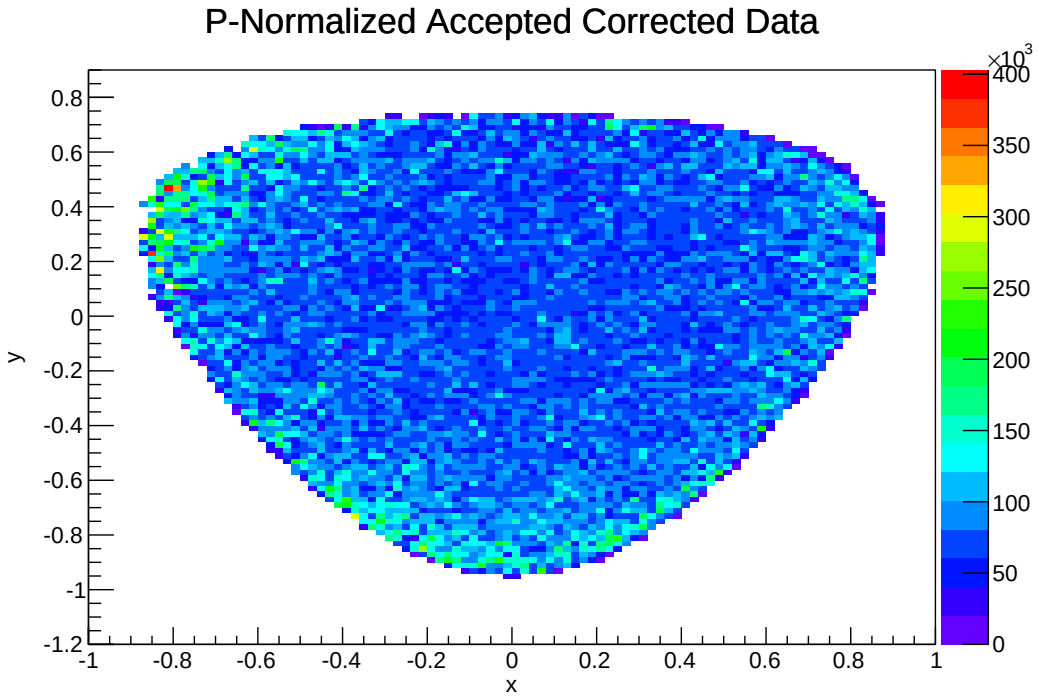

Figure 68: Dalitz for accepted data, normalized by P.

Although there are differences between the numerical result and our own, as we explained, we can see the similitude between both Dalitz plots by noticing that their corners are the populated zones.

Instead of fitting the equation we mentioned to the Dalitz, we will use a better method that performs the fit event by event, so we do not have to bin the data in order to fit it directly to the Dalitz plot. This was done using the PyPWA package, which performs an unbinned extended likelihood fit by minimizing the quantity [39]

$$-\ln \mathscr{L} = -\sum_{i=1}^{N} Q_i \ln\left[I(\vec{x}_i, \vec{a})\right] + \frac{1}{N_g}\sum_{i=1}^{N_a} I(\vec{x}_i, \vec{a}) \tag{5.3}$$

where N is the number of data events, Q_i their Q-factor, I the function described in equation 5.2, $\vec{x}_i$ the set of measurements for each one, $\vec{a}$ the set of parameters we want to fit and N_g and N_g the number of generated and accepted Monte Carlo events, respectively.

6 Results

For our analysis we will restrict to photon beam energies below 5.3 GeV, cut that was implemented at this stage.

6.1 ω Signal

We proceed then to correct by acceptance (already plotted in figure 64) the ω signal we got from our data after all the cuts and the weighting by the Q-factor.

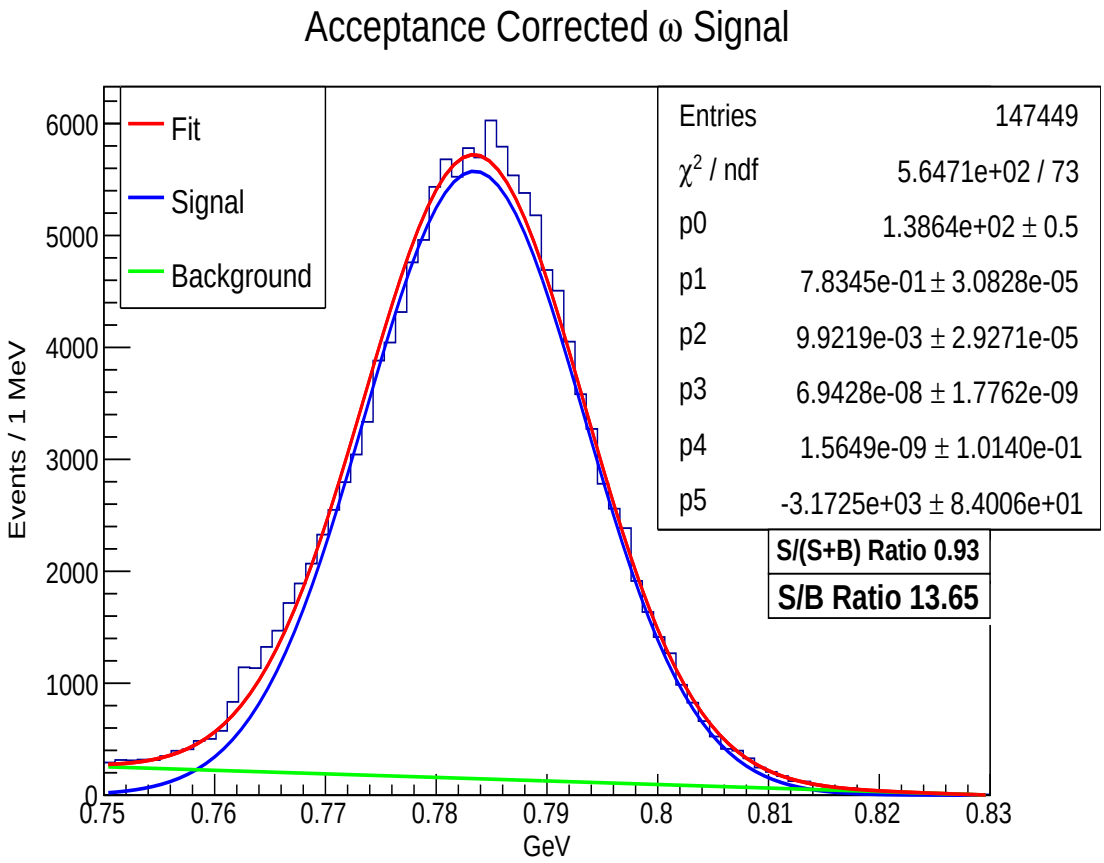

Figure 69: Acceptance corrected omega signal. The data fit is the red line, which is the sum of the blue line (a Voigtian corresponding to the signal) and the green line (a first order polynomial representing the background)

Figure 69 shows the acceptance corrected data fitted by a Voigtian with $\mu = p1$, $\sigma = p2$ and $\Gamma = p3$ multiplied by a factor $p0$ plus a polynomial of the form $y = p4 + p5(x - 0.75)$, as we have done before for each event in the Q-factor calculation, which will give us the signal and the remnants of the background.

The mass of the ω meson would be then the mean μ of the resulting Voigtian, and its widht will be given by σ. In this case we calculated the signal and background relations considering the areas under each curve between 0.75 and 0.83 GeV, which means that $\frac{S}{S+B}$ would correspond to the probability that any given event belongs to the signal, while in the calculation of the Q-factor, $Q_i = \frac{S_i}{S_i+B_i}$ was the probability that the particular event i belonged to the signal.

6.2 A_5 Parameter

Finally we plot the A_5 parameter that we obtained from fitting the JPAC Decay Model to our data in bins of energy, t' and P to show its dependence with those variables.

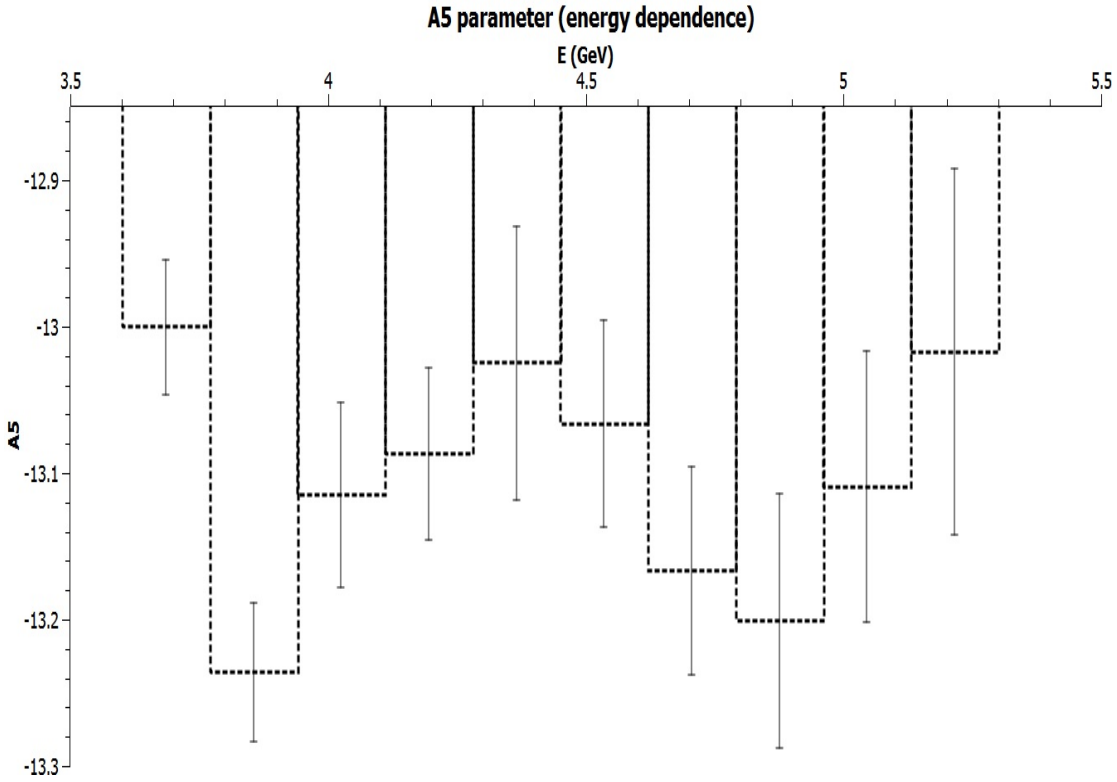

Figure 70: A_5 parameter dependence with energy.

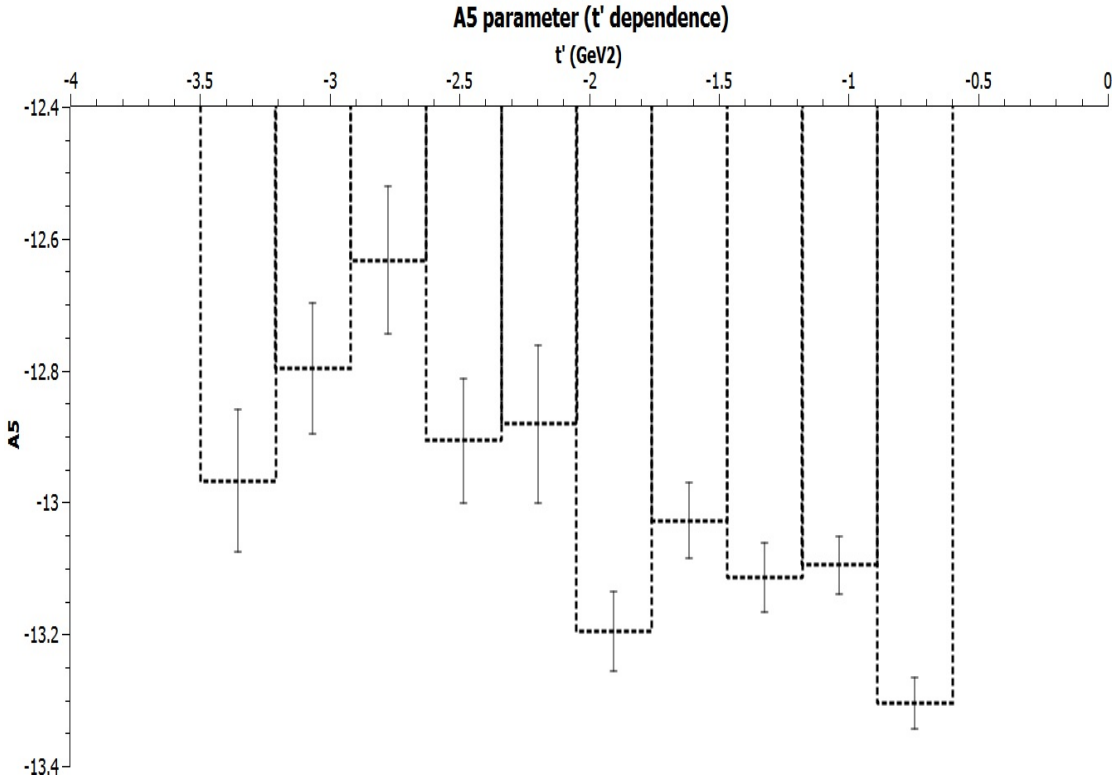

Figure 71: A_5 parameter dependence with t'.

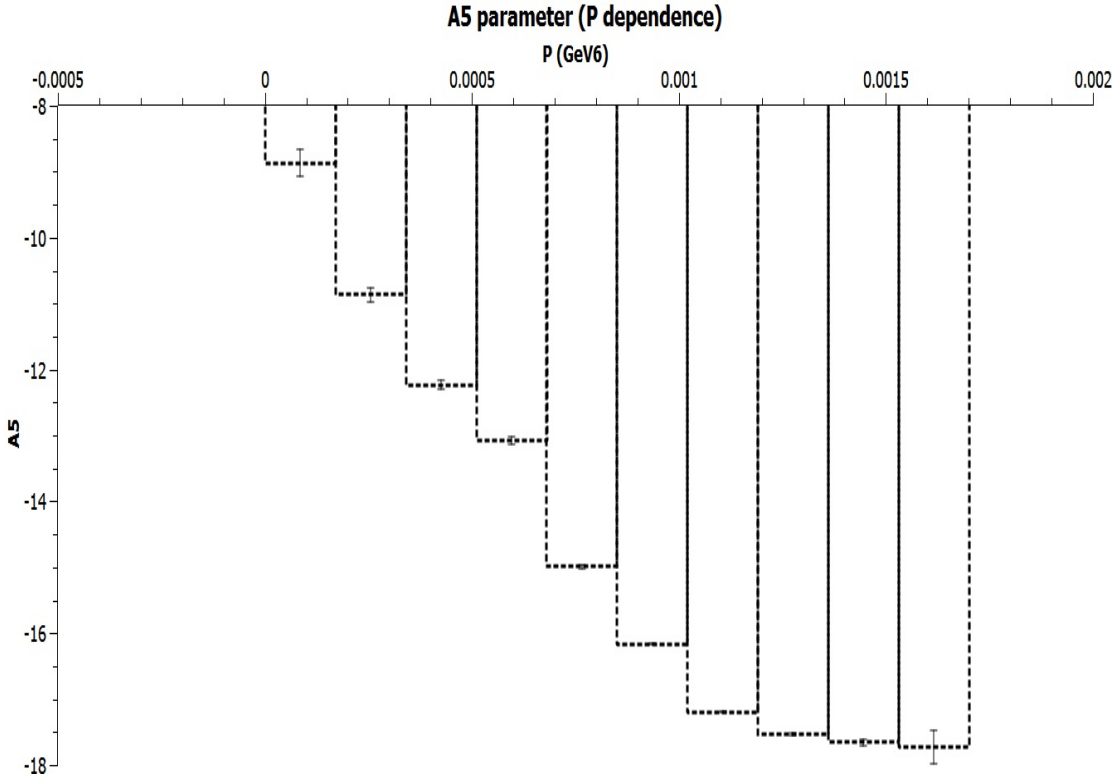

Figure 72: A_5 parameter dependence with P.

We can see that A_5 have little dependence with the photon energy and t' since its relative variation around certain value is small, as we expected, but this value is negative, when we were expecting a positive one. We also plotted the A_5 dependence with P, which seems to be monotonous and decreasing with it but stabilizing around $P = 0.0015\, GeV^6$.

We also verify that the parameters A_2, A_3 and A_4 obtained from the fit, which we are not showing here, are in good concordance with the ones from previous analysis at lower energies.

7 Conclusions And Discussion

We analyzed the $\gamma p \to p\omega$ reaction by means of its $p\omega \to p3\pi$ decay at a range of energies where the ω photoproduction has not been studied before, but only at energies below 3.6 GeV. A series of cuts on the data were performed, the probability for each event to belong to the signal of interest was calculated and weighted in, and the data was corrected by acceptance, which was obtained from a Monte Carlo simulation and various programs that simulate the detector. We then obtained a clear ω signal with 147449 events from where the mass and width of the ω were inferred, and finally a fit to the JPAC Decay Model was performed.

From figure 69 we can conclude that most of the background noise has been removed, and that the Q-factor method was instrumental to this, as can be seen in figure 55. Before deciding to use this we were trying to remove the background by other means, like side-band subtraction, which is the method used on the presentations done before about this work, but this proved to be not as effective as the one used here. We ended obtaining a clean ω signal with a resulting mass of 783.45 MeV and a width of 9.92 MeV, which is in good concordance with the PDG values of 782.65 and 8.49 MeV.

The Dalitz plot we obtained from the data, shown in figure 68, has a strong resemblance with the one obtained numerically by the JPAC, which is shown in figure 5, even when the last one does not take into account the photoproduction at a range of energies but only the decay at a fixed energy. This would have a blurring effect over the Dalitz plot obtained from the experimental data when compared to the numerical one because the former would be the result of a superposition of many Dalitz plots, each one constructed at a different fixed energy.

The fitting of the JPAC Decay Model to the experimental data resulted in a negative A_5 parameter (also called a_0 when we were only considering the decay), as can be seen in figures 70, 71 and 72, which is not in concordance with what was expected from the model. This appears to be also the case on the work of Chris Zeoli [40], which is similar to this one but with a photon beam energy range below 3.6 GeV. The possible causes of these negative results are still being discussed by the JPAC.

The dependence of A_5 with energy and t' seems to be none as can be seen from figures 70 and 71, where the parameter show little relative variation around certain

value. This was expected from the model. The P case is shown in figure 72, where A_5 seems first to diminish and then becomes constant, although the significance of this is still being discussed.

The parameters A_2, A_3 and A_4, that come from the photoproduction and were never obtained at these energies before, seem to be in good concordance with the ones from previous analysis at lower energies.

The stability of the fit is being studied by the JPAC and work is in progress to identify the possible causes of the negative result concerning the A_5 parameter, since it would be useful to have a tested model for this and similar decays.

The t distribution imposed on the Monte Carlo was of the form e^{3t} as expected from previous works, but we could have obtained it from fitting it to our data. This could have caused the already mentioned differences of the energy and t' distributions between the accepted Monte Carlo and the selected data, which is another issue that should be considered on any subsequent analysis.

Appendices

A Photoproduction Mandelstam Variables

The Mandelstam variables are used for scattering processes of two particles to two particles. If we consider the diagram shown in figure 73 and the signature of the Minkowski metric is chosen as (1,-1,-1,-1), then we define them as

$$s = (P_1^\mu + P_2^\mu)^2 = (P_3^\mu + P_4^\mu)^2 \tag{A.1}$$

$$t = (P_1^\mu - P_3^\mu)^2 = (P_2^\mu - P_4^\mu)^2 \tag{A.2}$$

$$u = (P_1^\mu - P_4^\mu)^2 = (P_2^\mu - P_3^\mu)^2 \tag{A.3}$$

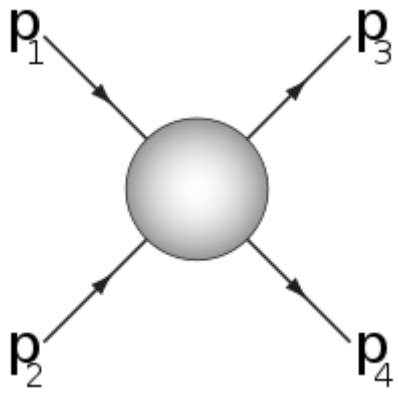

Figure 73: Particles 1 and 2 enter the diagram, they interact, and particles 3 and 4 exit it.

The different possible scattering processes are shown in figure 74, they are called s, t and u because these quantities would correspond to the four-momentum squared of the intermediate particle.

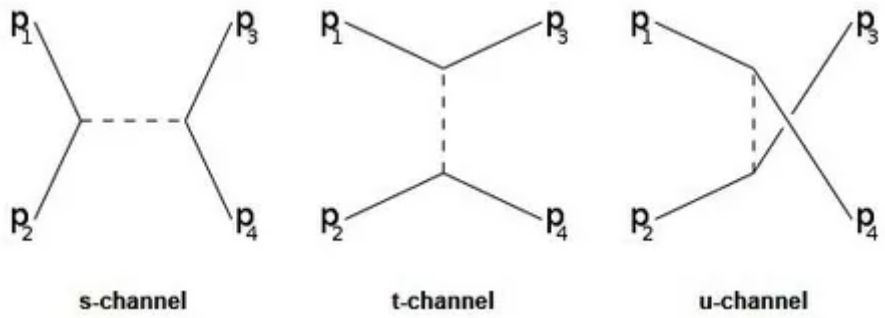

Figure 74: Possible scattering diagrams.

We are interested in the t-channel reaction $\gamma p \to p\omega$. From the reconstructed four-momentums of the photon, the target proton and the scattered proton, which we will call P_γ, P_{tp} and P_{sp} respectively, we know that

$$P_\omega = P_\gamma + P_{tp} - P_{sp}$$

Writing them in the Center of Mass frame (denoted by an asterisk) we have

$$P^*_\gamma = (E^*_\gamma = p^*_\gamma, \vec{p}^*_\gamma)$$

$$P^*_{tp} = (E^*_{tp} = \sqrt{p^{*2}_{tp} + m^2_p}, \vec{p^*_{tp}} = -\vec{p}^*_\gamma)$$

$$P^*_\omega = (E^*_\omega = \sqrt{p^{*2}_\omega + m^2_\omega}, \vec{p}^*_\omega)$$

$$P^*_{sp} = (E^*_{sp} = \sqrt{p^{*2}_{sp} + m^2_p}, \vec{p}^*_{sp} = -\vec{p}^*_\omega)$$

From the definition of the Mandelstam variable s we can write

$$s = (P_\gamma + P_{tp})^2 = (E^*_\gamma + E^*_{tp})^2 = (P_\omega + P_{sp})^2 = (E^*_\omega + E^*_{sp})^2$$

Before the interaction takes place we have

$$0 = p^{*2}_\gamma - p^{*2}_{tp} = E^{*2}_\gamma - E^{*2}_{tp} + m^2_p = (E^*_\gamma + E^*_{tp})^2 - 2E^*_{tp}(E^*_\gamma + E^*_{tp}) + m^2_p$$

which means that

$$E^*_{tp} = \frac{s + m^2_p}{2\sqrt{s}} \tag{A.4}$$

After the interaction takes place we have

$$0 = p^{*2}_\omega - p^{*2}_{sp} = E^{*2}_\omega - m^2_\omega - E^{*2}_{sp} + m^2_p = (E^*_\omega + E^*_{sp})^2 - 2E^*_{sp}(E^*_\omega + E^*_{sp}) + m^2_p - m^2_\omega$$

which means that

$$E^*_{sp} = \frac{s + m^2_p - m^2_\omega}{2\sqrt{s}} \tag{A.5}$$

From the definition of the Mandelstam variable t we can write

$$t = (P_{tp} - P_{sp})^2 = (E^*_{tp} - E^*_{sp})^2 - (\vec{p}^*_{tp} - \vec{p}^*_{sp})^2$$

We use the first equality to obtain t from the four-momentums reconstructed in the laboratory frame (we obtain s and u in the same manner with their respective

equalities). We will use the second equality to obtain t_{min}, therefore since the scattering angle would be null, the vectorial sum becomes an algebraic one. We need to work out the energies term, multiplying its root square by $2\sqrt{s}$ we have

$$2(E^*_{tp}-E^*_{sp})(E^*_{\gamma}+E^*_{tp}) = (E^*_{tp}+E^*_{\gamma}+E^*_{sp})^2 - E^{*2}_{\gamma} - E^{*2}_{sp} + E^{*2}_{tp} = E^{*2}_{\omega} - p^{*2}_{\gamma} - p^{*2}_{sp} + p^{*2}_{tp}$$

where two m_p^2 terms have canceled out. Since $p^{*2}_{\gamma} = p^{*2}_{tp}$ and $p^{*2}_{sp} = p^{*2}_{\omega}$ we have

$$t_{min} = \left(\frac{m^2_{\omega}}{2\sqrt{s}}\right)^2 - (p^*_{tp} - p^*_{sp})^2$$

where the momentums can be obtained from A.4 and A.5, which means that we can calculate $t' = t - t_{min}$ with the four-momentums reconstructed from the measured data, taking m_{ω} as the missing mass of the proton.

B ω Decay Frames

The Gottfried-Jackson frame [41] is a frame where the ω is at rest and, if p_{γ} and p_{ω} are the four-momentum of the incident photon and the ω meson, the coordinate system will then be defined as

$$\hat{z} = \vec{p_{\gamma}}$$
$$\hat{y} = \frac{\vec{p_{\gamma}} \times \vec{p_{\omega}}}{|\vec{p_{\gamma}} \times \vec{p_{\omega}}|}$$
$$\hat{x} = \hat{y} \times \hat{z}$$

In this way, $\hat{z}$ will be in the direction of the photon beam, $\hat{y}$ will be perpendicular to the production plane, and $\hat{x}$ is defined as to produce a right-handed system.

We will define also $\hat{\pi}$ as perpendicular to the decay plane in the Gottfried-Jackson frame

$$\hat{\pi} = \frac{\vec{p}_{\pi^+} \times \vec{p}_{\pi^-}}{|\vec{p}_{\pi^+} \times \vec{p}_{\pi^-}|}$$

Then we can define the decay angles as

$$\cos\theta = \hat{\pi} \cdot \hat{z} \tag{B.1}$$

$$\cos\phi = \frac{\hat{y}\cdot(\hat{z}\times\hat{\pi})}{|\hat{z}\times\hat{\pi})|} \tag{B.2}$$

$$\sin\phi = -\frac{\hat{x}\cdot(\hat{z}\times\hat{\pi})}{|\hat{z}\times\hat{\pi})|} \tag{B.3}$$

The Adair frame only differs form the Gottfried-Jackson frame in that the $\hat{z}$ is chosen to be the direction of the photon in the overall CM frame. The Adair angles are defined then by the set of equations already shown.

References

[1] ROOT website. *https://root.cern.ch/.*

[2] W. Cottingham and D. Greenwood. *An Introduction to the Standard Model.* Cambridge University Press, (1998).

[3] M. Gell-Mann. *Physics Letters 8(3), 214-215.* (1964).

[4] G. Zweig. *CERN Report 8182/TH.401.* (1964).

[5] W. Greiner, A. Schfer. *Quantum Chromodynamics.* Springer, (1994).

[6] CERN website. *http://aliceinfo.cern.ch/Public/en/Chapter1/results.html.*

[7] D.J. Gross and F. Wilczek. *Physical Review Letters, 30(26), 1343.* (1973).

[8] H.D. Politzer. *Physical Review Letters, 30(26), 1346.* (1973).

[9] W. Heisenberg. *ber den Bau der Atomkerne. Zeitschrift fr Physik, 77 1-11.* (1932).

[10] D. Griffiths. *Introduction to Elementary Particles, Second Revised Edition, 129-136.* WILEY-VCH, (2008).

[11] T.D. Lee and C.N. Yang. *Physical Review, 104(1), 254.* (1956).

[12] C.S. Wu et al. *Physical review, 105(4), 1413.* (1957).

[13] S. Gasiorowicz. *Quantum Physics, Third Edition, 243.* John Wiley & Sons, Inc., (2003).

[14] A.J. Barr. *Nuclear and Particle Physics, 20-21.* CreateSpace Independent Publishing Platform, (2014).

[15] A. Astbury et al. *Proceedings of the 29th International Conference on High Energy Physics, 1226-1228.* (1998).

[16] I.V. Danilkin et al. (Joint Physics Analysis Center). *Physical Review D, 91(9), 094029.* (2015).

[17] S. Chung. *BNL-QGS-02-0900. Brookhaven Nat. Lab, 14.* (2014).

[18] M. Jacob and G.C. Wick. *Annals of Physics, 7(4), 404-428.* (1959).

[19] D. Herndon, P. Soding and R. J. Cashmore. *Physical Review D, 11(11), 3165.* (1975).

[20] N. N. Khuri and S. B. Treiman. *Physical Review, 119(3), 1115.* (1960).

[21] Center for Theoretical I.V. Danilkin and Thomas Jefferson National Accelerator Facility Computational Physics. *Private Communication.* (2016).

[22] J. Beringer et al. *Physical Review D, 86(1), 010001.* (2012).

[23] F. Niecknig, B. Kubis and S.P. Schneider. *The European Physical Journal C, 72(5), 1-24.* (2012).

[24] Florida International University D. Schott. *A Search For An Exotic Meson In The* $\gamma + P \rightarrow \Delta^{++} + \pi^- + \eta$ *Reaction. Florida International University. PhD thesis.* (2012).

[25] CERN website. *http://home.cern/about/engineering/radiofrequency-cavities.*

[26] J. Li. Rensselaer Polytechnic Institute. *Search For Exotic Mesons In* $\pi^+\pi^-\pi^0$ *Decay. PhD thesis.* (2003).

[27] Y. Patois. *Slow Controls for Beam-Line Devices in Hall B at CEBAF.* (1997).

[28] D.I. Sober et al. *Nuclear Instruments and Methods in Physics Research Section A 440(2), 263-284.* (2000).

[29] B.A. Mecking et al. *Nuclear Instruments and Methods in Physics Research Section A 503(3), 513-553.* (2003).

[30] K.A. Olive et al (Particle Data Group). *Chin. Phys. C, 38 (9): 090001.* IOP Publishing, (2014).

[31] D. Keller. *CLAS-NOTE, Jefferson Lab, 2010-015.* (2010).

[32] P.D.B. Collins and A.D. Martin. *Hadron Interactions, 67-69.* (1984).

[33] g12 Collaboration. *g12 Analysis Procedures, Statistics and Systematics.* (2015).

[34] Minuit Home Page. *www.cern.ch/minuit.*

[35] M. Williams. Carnegie Mellon University. *Measurement of Differential Cross Sections and Spin Density Matrix Elements alog with a Partial Wave Analysis for $\gamma p \to p\omega$ using CLAS at Jefferson Lab. PhD thesis.* (2007).

[36] M. Williams et al. Carnegie Mellon University. *Journal of Instrumentation, 4(10), P10003.* (2009).

[37] D.I. Sober et al. *Nuclear Instruments and Methods in Physics Research Section A 440(2), 263-284.* (1970).

[38] K. Schilling et al. *Nuclear Physics B, 15(2), 397-412.* (1970).

[39] S. Bramlett et al. *The PyPWA Project, https://pypwa.jlab.org/.* (2015).

[40] Florida State University C. Zeoli. *Private Communication.* (2015).

[41] C.W. Salgado and D.P. Weygand. *Physics Reports, 537(1), 1-58.* (2014).